

國立臺灣大學工學院材料科學與工程學研究所



碩士論文

Department of Materials Science and Engineering

College of Engineering

National Taiwan University

Master Thesis

銅基材料在固態燃料電池陽極端導電性、

溫度感測及催化性質之研究

Study of Electric Conductivity, Temperature Sensing,

and Catalytic Effect of Cu-Based Materials

for Anode of Solid Oxide Fuel Cells

林雨芊

Yu-Chien Lin

指導教授：韋文誠 博士

Advisor: Wen-Cheng J. Wei, Ph.D.

中華民國 107 年 7 月


July 2018

國立臺灣大學碩士學位論文  
口試委員會審定書


論文中文題目：銅基材料在固態燃料電池陽極端導電性、溫度感測及催化性質之研究

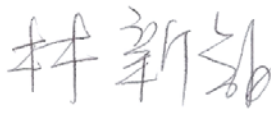
論文英文題目：Study of Electric Conductivity,  
Temperature Sensing, and Catalytic  
Effect of Cu-Based Materials for Anode  
of Solid Oxide Fuel Cell

本論文係林雨芊(R05527053)在國立臺灣大學材料科學  
與工程學系、所完成之碩士學位論文，於民國 107 年 7 月 20  
日承下列考試委員審查通過及口試及格，特此證明

口試委員： 韋文誠   
(指導教授)

吳玉娟 

郭俞麟 

系主任、所長 林新智  (簽名)

## 誌謝



時光飛逝，轉眼間碩士生涯即將結束，回想起剛加入 Wei-group 的時候還對燃料電池這個領域並不了解，經過兩年的學習，如今也順利完成了這本碩士論文。首先，我最要感謝的是我的指導教授韋文誠老師。老師在課業上非常有耐心的教導我們，也對我們寄予很高的期望。**主動、溝通和執行力**是老師一開始給予學生的三個目標，做到這三點讓我提高很多工作效率。老師也常常告訴我要建立自信心，並了解自己的優點和缺點，這樣才能不斷的進步。除此之外，老師在生活上對我們學生也非常關心，過年過節會舉辦一些跟畢業學長姊的聚會，讓我感受到 Wei-group 這個大家庭溫馨的氣氛。

另外，實驗室的同伴們也提供我很多幫助。謝謝彥友學長告訴我們很多實驗上要注意的細節，關心我們的實驗進度。在我遇到困難時，也提供我很多想法，每次跟學長討論完，都覺得受益良多。感謝冠宇學長、邱傑學姊和怡婷學姊教導我各種實驗器材的使用，畢業後對於我的問題也都不厭其煩的解答。我也特別要感謝逸紋和聿紘這兩位好夥伴。感謝逸紋常常陪我在閒暇之餘聊天散心，不斷的給予我鼓勵。聿紘的研究主題與我比較相近，對於實驗規劃也很有方法。謝謝他常常陪我討論到很晚，最後在電池的測試與設計上也提供我很多想法。這兩年有他們的陪伴與激勵，能讓我不斷地向前邁進。感謝庭懿、廷恩和坤祥三個學弟常常先將儀器讓給我使用，讓我順利完成實驗。也感謝台大環工所張慶源老師實驗室、台大地質科學系鄧茂華老師實驗室和台科大機械系郭俞麟老師實驗室的同學及學長在實驗上幫助我。最後，我要感謝我的家人以及朋友，在這段期間給予我的支持與鼓勵，讓我能順利完成碩士學位，謝謝大家。

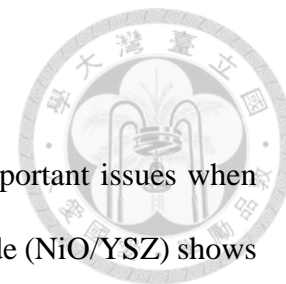
## 摘要



燃料電池在使用碳氫燃料時，陽極的碳沉積和催化能力是兩個非常重要的研究項目。在最近的研究報告指出，鎳基陽極(NiO/YSZ)會與碳氫燃料反應，產生嚴重的碳沉積。故在本實驗中使用氧化銅來取代氧化鎳，以改善此現象。以固相法合成三種含銅、鎳及氧化鋅之陽極粉末。實驗中測試陽極催化前後滲透率，以證明樣品的積碳程度。半銅半鎳鋅(C<sub>50</sub>N<sub>50</sub>Z)陽極片在甲烷中具有良好的催化性質，且積碳速率較慢。在650 °C中溫燃料電池操作溫度下，C<sub>50</sub>N<sub>50</sub>Z的導電性為1503 Scm<sup>-1</sup>，可以將銅的高導電及溫度感測與催化功能結合，進行下面四種銅、銅鎳、銅基合金及鎳線(Cu, Cu11Ni, Cu-38Zn, Cu9Ni6Sn, Ni)之室溫及高溫導電性測試。銅在650 °C下的導電性最優，足以作為電流收集的材料。由上述線材製作的五種熱電偶在 200 °C~650 °C進行長時間 (>100小時) 測試，檢視熱電位的靈敏度及飄移量的要求，Cu-Cu11Ni, Cu-Cu9Ni6Sn和Cu-Ni三種熱電偶可在中溫型固態燃料電池中做為溫度感測器。因此，在燃料電池陽極端，銅基材料可以同時具有催化、溫度感測以及當作電流收集層等三種功能。

關鍵字：銅基、陽極、催化、滲透率、碳沉積、熱電偶、固態燃料電池。

## ABSTRACT



Carbon deposition and catalytic ability of anodes are two important issues when using hydro-carbon fuels for solid oxide fuel cells. Nickel based anode (NiO/YSZ) shows a serious carbon deposition reported in recent research. Therefore, CuO is added to replace the NiO. In this study, three anode powders (100%Ni with 8YSZ, 50%Cu-50%Ni with 8YSZ and 100%Cu with 8YSZ) are prepared by powder mixing in well-dispersed slurry. A new approach to verify the effects of carbon deposition by measuring the permeability of the anodes are used in this study. C<sub>50</sub>N<sub>50</sub>Z shows a good catalytic ability and low coking rate for CH<sub>4</sub>. The conductivity of C<sub>50</sub>N<sub>50</sub>Z is 1503 Scm<sup>-1</sup> at 650 °C. Another two functions of copper can be combined with this anode. Four copper-based metal and nickel wires (Cu, Cu11Ni, Cu-38Zn, Cu9Ni6Sn, Ni) are tested for their electric conductivity at room to high temperature. Due to a high electric conductivity, Cu is good enough to apply as a material for current collector. Five different thermocouples made from above wires are also aging in air for more than 100 h at 200 °C~650 °C. Because of sensibility and less drift (<5%) of thermopotential at 200 °C to 650 °C, three thermocouples Cu-Cu11Ni, Cu-Cu9Ni6Sn and Cu-Ni are suitable for intermediate-temperature SOFC as temperature sensors. Thus, triple function of Cu-based materials can be applied on anode side of SOFCs.

**Keywords:** Cu-based; anode; catalytic; permeability; carbon deposition; thermocouple; SOFCs.

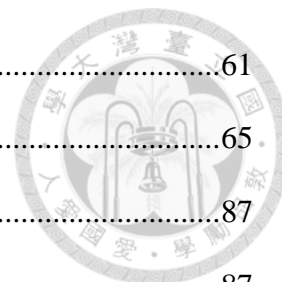
# CONTENTS



口試委員會審定書 .....	I
誌謝 .....	II
摘要 .....	III
ABSTRACT .....	IV
CONTENTS .....	V
LIST OF FIGURES .....	VIII
LIST OF TABLES .....	XIII
<b>Chapter 1 Introduction.....</b>	<b>1</b>
Research Objectives .....	3
<b>Chapter 2 Literature Review .....</b>	<b>4</b>
2.1 SOFCs .....	4
2.1.1 Carbon Deposition at Anode .....	5
2.1.2 Sulfur Corrosion .....	6
2.1.3 Thermal Expansion Coefficient (CTE) of Copper .....	6
2.1.4 Fabrication Method of Copper-Based Anode.....	7
2.2 Permeability of Porous Ceramics .....	13
2.2.1 Darcy Flow and Non-Darcy Flow .....	13
2.2.2 Non-Darcy Flow in Porous Media .....	14
2.3 Thermocouple .....	17
2.3.1 Principal of Thermoelectric Thermometry[41] .....	17
2.3.2 Common Thermocouple Types .....	18
2.3.3 Fabrication and Sealing Method of Thermocouple.....	20

<b>Chapter 3</b>	<b>Experimental Procedure.....</b>	<b>23</b>
3.1	Materials .....	23
3.2	Anode Preparation and Cell Assembly .....	23
3.3	Preparation of Thermocouple .....	25
3.4	Property Characterization .....	25
3.4.1	Sedimentation Test .....	25
3.4.2	XRD Analysis.....	26
3.4.3	SEM Analysis.....	26
3.4.4	Density Measurement.....	27
3.4.5	Thermogravimetric Analysis (TGA) .....	27
3.4.6	Permeability Test.....	28
3.4.7	Gas Chromatography .....	29
3.4.8	Conductivity Measurement .....	29
3.4.9	Thermopotential measurement.....	30
3.4.10	Thermal Expansion Analysis (Dilatometer, DIL) .....	31
<b>Chapter 4</b>	<b>Results and Discussions .....</b>	<b>37</b>
4.1	Electric Properties of Cu-based Alloy .....	37
4.1.1	Conductivity of Cu-based Alloy.....	37
4.1.2	Seebeck coefficient of Thermocouples .....	39
4.1.3	Short-term Thermopotential of Thermocouples.....	41
4.1.4	Long-term Thermopotential of Thermocouples .....	42
4.2	Properties of Anode .....	58
4.2.1	Dispersion Properties .....	58
4.2.2	Porosity of Anode.....	59
4.2.3	TGA Analysis of Anode Materials .....	60

4.2.4	Catalytic Effects of Methane.....	61
4.2.5	Electrical Conductivity of Anode.....	65
4.3	Fabrication and Characterization of Half-Cell .....	87
4.3.1	N <sub>100</sub> Z Anode Supported Cells .....	87
4.3.2	C <sub>50</sub> N <sub>50</sub> Z Anode Supported Cell.....	95
4.3.3	Improvement of C <sub>50</sub> N <sub>50</sub> Z Anode Supported Cell .....	102
Chapter 5 Conclusions.....		106
Appendix .....		108
REFERENCE .....		118





# LIST OF FIGURES



Fig. 2.1 Schematic diagram of an anode-supported SOFC .....	12
Fig. 2.2 Schematic diagram of (a) Darcy's Law and (b), (c) the relationship between Reynolds number and fluid flow velocity [40].....	16
Fig. 2.3 Schematic diagrams illustrating (a) Seebeck effect, (b) Peltier effect, and (c) Thomson effect. ....	22
Fig. 3.1 Flowchart of single cell preparation.....	34
Fig. 3.2 Schematic diagram of GC and permeability test.....	35
Fig. 3.3 Schematic diagram of four probe conductivity test. ....	36
Fig. 4.1 Electrical conductivities of C, C11N, CZ and N wire samples tested from room temperature to 700 °C in air. ....	45
Fig. 4.2 Arrhenius plots of $\sigma T$ versus $1/T$ of four wires.....	46
Fig. 4.3 Electrical conductivities of C, C11N and CZ wire samples in different curvatures tested at room temperature. ....	47
Fig. 4.4 (a) TGA and (b) DSC analysis result of five wires (C, C11N, C9N6S, CZ, and N) in air. ....	48
Fig. 4.5 Thermopotential plotted against temperature of five thermocouples.....	49
Fig. 4.6 Seebeck coefficient versus temperature of three thermocouples. ....	50
Fig. 4.7 (a) Thermopotentials of five types of thermocouples tested at 200 °C in first 5 min.(b) There are big variations on C11N-CZ when test three times. ....	51
Fig. 4.8 Thermopotentials of five types of thermocouples tested at 400 °C in first 5 min. ....	52
Fig. 4.9 Thermopotentials of five types of thermocouples tested at 600 °C in first 5	

min. ....	53
Fig. 4.10 Time dependence test of thermo-potential of C-C11N and C11N-CZ thermocouples at 200 °C in air.....	54
Fig. 4.11 Time dependence test of thermo-potential of C-C11N, C -C9N6S, C-N and C11N-CZ thermocouples at 400 °C in air.....	55
Fig. 4.12 Time dependence test of thermo-potential of C-C11N,C-C9N6S and C-N thermocouples at 650 °C in air.....	56
Fig. 4.13 Microstructure of four wires (a) and (b) C, (c) and (d) C11N, (e) and (f) C9N6S, (g) and (h) N before and after heat-treated at 650 °C for 100 h in air. ....	57
Fig. 4.14 Sedimentation height ratio ( $H_t/H_0$ ) of 8YSZ, NiO and MCMB slurries using 95% ethanol plotted against sedimentation time. ....	69
Fig. 4.15 Sedimentation height ratio ( $H_t/H_0$ ) of CuO slurries in four solvents plotted against sedimentation time.. ....	70
Fig. 4.16 Porosities of N <sub>100</sub> Z, C <sub>50</sub> N <sub>50</sub> Z and C <sub>100</sub> Z samples with 20 wt% pore former (MCMB) sintered at different temperatures. ....	71
Fig. 4.17 Porosities of C <sub>50</sub> N <sub>50</sub> Z samples sintered at selected temperature versus different amounts of pore former in anode formulation.....	72
Fig. 4.18 TGA test results of CuO or NiO powder in specified reducing atmosphere, either N <sub>2</sub> -20% H <sub>2</sub> or N <sub>2</sub> -20% CH <sub>4</sub> . ....	73
Fig. 4.19 TGA test of C <sub>100</sub> Z, C <sub>50</sub> N <sub>50</sub> Z and N <sub>100</sub> Z disks reduced in N <sub>2</sub> -20% H <sub>2</sub> . ....	74
Fig. 4.20 TGA test of C <sub>100</sub> Z, C <sub>50</sub> N <sub>50</sub> Z and N <sub>100</sub> Z disks reduced in N <sub>2</sub> -20% CH <sub>4</sub> . ....	75
Fig. 4.21 Crystal phase identification of C <sub>100</sub> Z anode before and after reduction. ....	76
Fig. 4.22 SEM micrographs of top view of anode disks, (a) C <sub>100</sub> Z sintered at 1000 °C, (b) after reduced at 700 °C for 10 h.....	77
Fig. 4.23 Crystal phase identification of C <sub>50</sub> N <sub>50</sub> Z anode before and after the	

reduction. ....	78
Fig. 4.24 Crystal phase identification of N <sub>100</sub> Z anode before and after the reduction. ...	79
Fig. 4.25 SEM micrographs of top view of C <sub>50</sub> N <sub>50</sub> Z anode disks, (a) sintered at 1200 °C,	
(b) after reduced at 700 °C for 10 h. ....	80
Fig. 4.26 SEM micrographs of top view of N <sub>100</sub> Z anode disks, (a) sintered at 1400 °C, (b)	
after reduced at 700 °C for 10 h. ....	81
Fig. 4.27 Content of H <sub>2</sub> in reacting gas (CH <sub>4</sub> ) through three anodes C <sub>100</sub> Z, C <sub>50</sub> N <sub>50</sub> Z and	
N <sub>100</sub> Z at 650 °C in 2 h. ....	82
Fig. 4.28 Pressure drop across N <sub>100</sub> Z and C <sub>50</sub> N <sub>50</sub> Z sample plot against velocity of N <sub>2</sub>	
before and after reacting with CH <sub>4</sub> at 650 °C in 2 h. ....	83
Fig. 4.29 Pressure head of the reactor plotted against deposition time showing the kinetics	
of coking reaction of C <sub>50</sub> N <sub>50</sub> Z and N <sub>100</sub> Z in CH <sub>4</sub> at 650 °C. ....	85
Fig. 4.30 Arrhenius plot of electric conductivity of N <sub>100</sub> Z sintered at 1500 °C with 20 wt%	
MCMB and C <sub>50</sub> N <sub>50</sub> Z sintered at 1300 °C without MCMB. ....	86
Fig. 4.31 SEM micrographs of surface morphology of N <sub>100</sub> Z anode pre-sintered at 1000	
°C (a) 200×, (b) 2500×. ....	90
Fig. 4.32 SEM micrographs of the top view of N <sub>100</sub> Z anode with one layer of 8YSZ-N	
sintered at 1000 °C for 1 h, (a) 200×, (b) 2500×, and sintered at 1400 °C for	
1 h (c) 200×, (d) 2500×, and (e) cross-section. ....	91
Fig. 4.33 Shrinkage behavior (a) shrinkage and (b) shrinkage rate of 8YSZ-D, 8YSZ-T	
and N <sub>100</sub> Z presintered at 1000 °C with a heating rate of 5 °C min <sup>-1</sup> in air. ...	92
Fig. 4.34 SEM micrographs of top view of N <sub>100</sub> Z anode (a) with one layer of 8YSZ-N	
and two-layer 8YSZ-D sintered at 1400 °C, (b) with one layer of 8YSZ-N and	
two-layer of 8YSZ-T sintered at 1400 °C. ....	93
Fig. 4.35 SEM micrograph of top view of N <sub>100</sub> Z anode with one layer of 8YSZ-N and	

two-layer 8YSZ-T sintered at (a) 1400 °C, (b) 1450 °C, (c) 1500 °C for 1 h and (d) cross-section sintered at 1500 °C. ....	94
Fig. 4.36 The Shrinkage behavior of 8YSZ-T and C <sub>50</sub> N <sub>50</sub> Z presintered at 1000 °C or at 1100 °C at a heating rate of 5 °Cmin <sup>-1</sup> in air. ....	98
Fig. 4.37 SEM micrograph of top view of C <sub>50</sub> N <sub>50</sub> Z anode (a) pre-sintered at 1000 °C, (b) with one layer of 8YSZ-N and two layers 8YSZ-T sintered at 1000 °C. ....	99
Fig. 4.38 SEM micrographs of top view and cross-section of C <sub>50</sub> N <sub>50</sub> Z anode (with 20 wt% .....	100
Fig. 4.39 SEM micrographs of the top view and cross-section of C <sub>50</sub> N <sub>50</sub> Z anode spin- coated one layer of 8YSZ-N and two layers of 8YSZ-T. (a) and (b) sintered at 1200 °C (without MCMB), (c) and (d) sintered at 1200 °C (with 5 wt% MCMB), (e) and (f) sintered at 1400 °C (with 5 wt% MCMB). ....	101
Fig. 4.40 SEM micrographs of C <sub>50</sub> N <sub>50</sub> Z anode without MCMB. The anode (a) sintered at 1200 °C, and then (b) reduced at 600 °C for 1 h by H <sub>2</sub> . ....	104
Fig.4.41 SEM micrographs of (a) cross-section and (b) top view of anode and anode function layer (AFL), which was made by using spin-coating, (c) cross- section of single cell showing the thickness of individual layer, (d) top view of spin-coated two-layer of 8YSZ. ....	105
Fig. A-1 GC results of the reforming of LPG gas at a flow rate of 10 mlmin <sup>-1</sup> at different temperatures.....	110
Fig. A-2 Content of H <sub>2</sub> in the reforming gas (LPG) through three anodes C <sub>100</sub> Z, C <sub>50</sub> N <sub>50</sub> Z and N <sub>100</sub> Z at 650 °C in 2 h.....	111
Fig. A-3 Content of CH <sub>4</sub> in reforming gas (LPG) through three anodes C <sub>100</sub> Z, C <sub>50</sub> N <sub>50</sub> Z and N <sub>100</sub> Z at 650 °C in 2 h.....	112
Fig. A-4 (a) N <sub>100</sub> Z anode sintered at 1400 °C before tested with LPG, (b) carbon	

deposition on the N <sub>100</sub> Z anode after reacting with LPG for 2 h at 650 °C.....	113
Fig. A-5 (a) cross- section of cell 1 (b) I-V curve and power density of cell 1 using H <sub>2</sub> as a fuel.....	116
Fig. A-6 (a), (b) cross- section of cell 2 (c) I-V curve and power density of cell 2 using H <sub>2</sub> as a fuel.....	117

# LIST OF TABLES

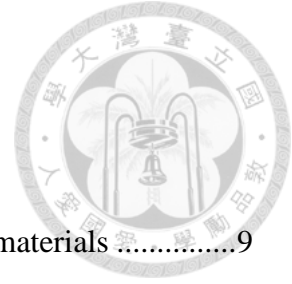
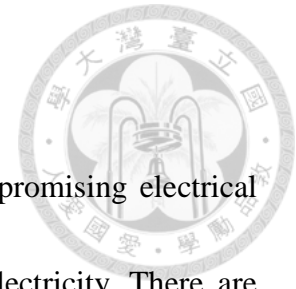


Table 2.1 Coefficient of thermal expansion of anode and electrolyte materials .....	9
Table 2.2 Summary of SOFC literature with Cu-based anode .....	10
Table 2.3 Types of Commercial Thermocouple.....	21
Table 3.1 Abbreviation name of anode materials .....	32
Table 3.2 Diameter and length of four Cu-based alloy and Ni wires .....	33
Table 4.1 Young's modulus and hardness of Cu-based alloys [courtesy by Yi-Ting, [48]] .....	44
Table 4.2 Properties of raw powders for anode .....	67
Table 4.3 Dispersion results ( $H_f/H_0$ ) of NiO, 8YSZ and MCMB [courtesy by Mu-Min, [43]] .....	68
Table 4.4 Permeability of two anodes before and after carbon deposition.....	84
Table A-1 Content of $H_2$ and $CH_4$ in LPG after reacting with sample at 650 °C.....	109

# Chapter 1 Introduction



Solid oxide fuel cells (SOFCs) had been known as one of promising electrical power generators, which convert chemical energy directly into electricity. There are several advantages of SOFCs, including high efficiency, well fuel flexibility and low pollution. The cell consists of anode, electrolyte and cathode. The anode is an important component for fuel oxidation and electron release [1].

Hydrogen is utilized in most SOFC study because of its high inherent energy, clean and eco-friendly properties. The cost of producing hydrogen by thermal decomposition of water is as low as NT\$18/kg, while refined high purity hydrogen costs US\$5.0/kg [2]. Since hydrogen is flammable, a low density and easy leakage problems, the storage and transportation of hydrogen show technology difficulty and cost a lot. Instead, gaseous hydrocarbon fuel may be an alternative choice to apply on SOFC.

Nickel and yttria-stabilized zirconia (YSZ) cermet is a common anode material in SOFC, when it uses  $H_2$  as a fuel. However, good catalytic properties of a Ni-YSZ anode using hydrocarbon fuels will induce hydrocarbon cracking reaction, and result in carbon deposition and cell deterioration. Low activity of Cu for C-C formation [2] was reported and capable of preventing coking. Nickel therefore is replaced by copper in this work.

Cu shows a lower catalytic activity of the C-H bond [3] of the fuels. A better oxidation of a catalyst at anode is also needed. Therefore, optimal composition and new

design Cu-Ni anode are needed to figure out in this study.



When carbon deposit on anode, the active area of anode will reduce and the open channel (i.e. permeability) of the anode will also be decreased. So, the permeability is evolving, and needed to determine the degree of carbon deposition in the anode. Most studies on permeability are based on Darcy's law, of which a linear relationship between the pressure gradient and the fluid velocity are proposed [4]. However, Darcy's law is only valid for the flows of slow and high viscosity.

For non-Darcy flow, Forchheimer number is used as a criterion ( $>0.005$ ) to determine the validity of the relationship [5]. Because nitrogen and  $\text{CH}_4$  are used as a testing gas in this study and both meet the criteria of non-Darcy flow. Therefore, Forchheimer equation, which is formulated as a second-order of velocity, is applied in this study.

Cu and Cu-Ni Alloys have been widely used due to the cost and performance of electric conductivity. In addition, Cu-based thermal couples have been studied in several temperature sensor applications. They also have the potential being used as a current collector and thermal couple of SOFCs for their similar CTE and less interface reaction with Cu-Ni based anode. Thus, Cu-Ni-YSZ anode using different functions of Cu-Cu alloys are practiced in this research.



## Research Objectives

In this study, properties of Cu-based materials are investigated for establishment of the fundamentals of electric conductivity, thermal potential and catalytic capability of hydrocarbon fuels. Thus, the materials in appropriate combination are applying on the anode side of SOFC.

There are three main functions are designed tended to apply to improve the function of SOFC.

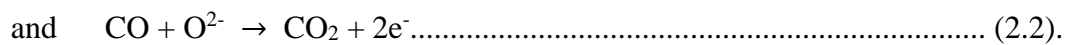
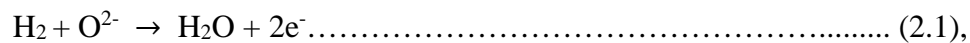
1. Find optimal Cu-Ni-YSZ anode to decrease carbon deposition and maintain the catalytic effect of hydrocarbon fuel;
2. Compare electrical conductivity of several Cu and Cu-alloy wires for using as current collector at an operating temperature (650 °C) of IT-SOFC;
3. Use Cu-based wires to make thermal couple for temperature sensing in a long-term test.

## Chapter 2 Literature Review

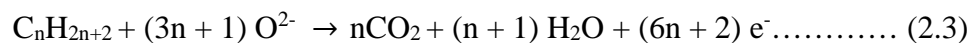


### 2.1 SOFCs

A solid oxide fuel cell (SOFC) is typically a sandwich structure, which consists of an anode, a cathode and an electrolyte in between, as shown in Fig. 2.1. On the cathode side, oxygen is reduced into oxygen ions by electron, and diffuses through the electrolyte layer to the anode. On the anode side, the arriving oxygen ions react with hydrogen or carbon mono-oxide (the fuels) and release two electrons, as the following equations [1].



However, the reactions can be more complex for hydro-carbon fuel,



If no enough oxygen is supplied, tar or fixed carbon will be made and retard the performance of SOFC.

There are several requirements for the anode of SOFC in order to have a high performance and long-term stability at operating temperatures [1, 6],

- (1) high porosity, at least 25% porosity;
- (2) High electrical conductivity;



- (3) Chemical compatibility with electrolyte;
- (4) Thermal expansion coefficient matching with electrolyte;
- (5) Capacity to prevent carbon deposit at reaction site;
- (6) High oxidation catalysis for various fuels.

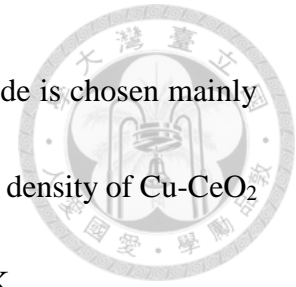
### 2.1.1 Carbon Deposition at Anode

In recent years, yttria-stabilized zirconia (YSZ) and Ni are the most employed anode material in SOFC due to its high activity for oxidation of H<sub>2</sub>. However, the catalytic effect of Ni-YSZ anode is decreased as carbon deposition, which is induced by incomplete oxidation from the hydrocarbon fuels.

Fixed carbon is produced by either a reverse water gas reaction, the disproportionation of CO, or the decomposition of CH<sub>4</sub>, as shown below.



Owing to a low activity for C-C formation by Cu [2], Cu-based anode is chosen mainly due to avoid coking. In Costa-Nunes' study [7], the maximum power density of Cu-CeO<sub>2</sub> cell was five times larger than that of Ni-YSZ cell in CO gas at 973K.




### 2.1.2 Sulfur Corrosion

Toxic sulfur is another problem for SOFC. Most of hydrocarbon fuels from fossil fuel or biomass contain sulfide impurities, which may corrode the ceramic parts and finally increase the polarization resistance, lowering the performance of the cells. Nickel-based anodes showed sulfur tolerance at levels of 0.05 ppm at 1023 K, improving only slightly with increasing temperature [8]. In order to prevent poisoning from hydrosulfide, some metals mixed with ceria materials are made as sulfur tolerant shift reaction catalysts [9]. One example Cu-CeO<sub>2</sub> anode can tolerant the sulfur in fuel gas up to 450 ppm at 1073K [10].

### 2.1.3 Thermal Expansion Coefficient (CTE) of Copper

This work tends to replace nickel by copper, taking this as a potential solution for SOFCs using hydrocarbon gases as fuel. During the cell-manufacturing and operating



process, thermal expansion coefficient matching with electrolyte is important. Table 2.1 shows the CTE of copper, nickel and some electrolyte materials. GDC [11], SDC [12], ScSZ [13] and YSZ are several common electrolytes of SOFCs. Thermal expansion coefficient of copper is higher than Nickel, and less matching with those electrolytes. Several dis-advantages are pre-visional. The Cu cannot be co-sintered with GDC, SDC, ScSZ and YSZ, due to the sintering capability, and needed sintering atmosphere of Cu is much different from those oxides. Thus, the fabrication of co-sintering is more difficult to the Cu-cermet as the anode.

#### **2.1.4 Fabrication Method of Copper-Based Anode**

There are three possible methods for solving the problems. First method is co-sintering electrode and electrolyte in one step, which can decrease the sintering temperature of the cells [11, 12, 14]. Sometimes, active metals, such as Li, was added as a sintering aid for the oxide electrolytes [15]. Second method is impregnation of Cu into porous YSZ preform. Graphite, polystyrene [16, 17], PMMA [18] and ammonium oxalate [13] have been used as pore formers and pre-mixed with YSZ powders. After calcining the mixture, pore formers were burnt out and left a porous skeleton. Then, the porous skeleton was impregnated with a Cu nitrate solution. After sintered in reducing

atmosphere, Cu-oxide anode can be made. Besides the methods, screen printing [19], electro-less plating [17] of Cu, or plasma spray [20] of mixed Cu-CeO<sub>2</sub> was also used for manufacturing of Cu-based anode of SOFC. The third is using Cu, Cu-Zn, or Cu-Ni alloy or oxide powder precursors.

Literature on Cu-based anode reports a variety of the approaches, as shown Table 2.2. Different alloy elements such as Li [11], Fe [16, 21], Co [22], Ni [18, 23] and Pd [24] were reported to add in Cu anode. The Cu-based alloys show a lower electric conductivity, but better CTE and co-sintering properties.

These SOFCs can be divided in to either electrolyte-support or anode-support. The performance of the anode-supported cells are superior to electrolyte-supported [25]. Some of excellent results, the highest power density is 1238 mW cm<sup>-2</sup> using H<sub>2</sub> at 850 °C with an anode-supported geometry. On the other hand, electrolyte-supported cell has a higher stability after reduction-oxidation cycles in anode because of its dense structure. But the electric resistance of the thick electrolyte layer is the major source of polarization during polarization. Few cases [19, 26, 27] reported outstanding power output.

Table 2.1 Coefficient of thermal expansion of anode and electrolyte materials

Component	Material	CTE(1/K×10 <sup>6</sup> )	Reference
Anode	Cu	16.5	[1]
	Ni	13.4	
Electrolyte	GDC	11.59-12.3	[28]
	SDC	11.9-12.0	
	ZrO <sub>2</sub> -8mol% Sz <sub>2</sub> O <sub>3</sub>	10.7	[1]
	ZrO <sub>2</sub> -11mol% Sz <sub>2</sub> O <sub>3</sub>	10.0	
	ZrO <sub>2</sub> -3mol% Y <sub>2</sub> O <sub>3</sub>	10.8	
	ZrO <sub>2</sub> -8mol% Y <sub>2</sub> O <sub>3</sub>	10.5	

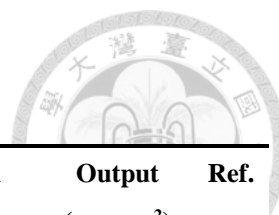


Table 2.2 Summary of SOFC literature with Cu-based anode

Anode	Electrolyte	Supported layer	Assembled method	Test Temp. (°C)	Fuel	Output (mWcm <sup>-2</sup> )	Ref.
Cu-CeO <sub>2</sub>	ScSZ	Porous ScSZ anode	Impregnation	800	H <sub>2</sub>	372	[13]
					C <sub>2</sub> H <sub>5</sub> OH + H <sub>2</sub> O	222	
Cu-Fe-Ce-YSZ	YSZ	Porous YSZ anode	Impregnation	800	H <sub>2</sub>	195	[16]
					CH <sub>4</sub>	90	
Cu-Ce-YSZ	YSZ	Porous YSZ anode	Impregnation	800	H <sub>2</sub>	140	[16]
					CH <sub>4</sub>	70	
Cu/YSZ + Ni/YSZ (Bilayer)	YSZ	Bilayer anode	Impregnation	750	96% H <sub>2</sub> + 4% H <sub>2</sub> O	228	[18]
					CH <sub>4</sub>	145	
NiFe-ZrO <sub>2</sub> /Cu	YSZ	anode	Impregnation	850	H <sub>2</sub>	1238	[21]
Cu+Co/CeO <sub>2</sub> +YSZ	YSZ	375 μm anode	Impregnation	800	H <sub>2</sub>	400	[22]
					n-C <sub>4</sub> H <sub>10</sub>	275	
					80% CH <sub>4</sub> + 20% O <sub>2</sub>	1165	
Cu+Ni+SDC	SDC	anode	Impregnation	600	CH <sub>4</sub>	317	[23]
Cu-Fe/CeO <sub>2</sub> -YSZ	YSZ	Porous YSZ anode	Impregnation	800	n-C <sub>4</sub> H <sub>10</sub>	240	[29]
					H <sub>2</sub>	260	
Cu-Co(Ru)/Zr <sub>0.35</sub> Ce <sub>0.65</sub> O <sub>2</sub>	YSZ	anode	Impregnation	800	H <sub>2</sub>	465	[30]
					CH <sub>3</sub> OH	444	



<b>Cu+Co+Ce O<sub>2</sub></b>	YSZ	Porous YSZ anode	Impregnation	800	H <sub>2</sub>	700	<a href="#">[31]</a>
					CH <sub>4</sub>	250	
<b>Cu–CeO<sub>2</sub>– YSZ/Ni– ScSZ</b>	ScSZ	anode	Impregnation	800	H <sub>2</sub>	604	<a href="#">[32]</a>
					C <sub>2</sub> H <sub>5</sub> OH	408	
<b>Li+Cu+GD C</b>	GDC	100 $\mu$ m anode	Hot-pressing	700	H <sub>2</sub>	200	<a href="#">[11]</a>
<b>Cu carbonate</b>	SDC+ Na <sub>2</sub> CO <sub>3</sub>	0.3-0.5mm of anode, electrolyte and cathode	Hot-pressing	500	H <sub>2</sub>	1150	<a href="#">[12]</a>
<b>Cu-YSZ</b>	YSZ	anode	Hot-pressing	800	H <sub>2</sub>	275	<a href="#">[14]</a>
<b>Cu+SDC</b>	SDC	electrolyte	Screen- printing	700	H <sub>2</sub>	92	<a href="#">[19]</a>
<b>Cu+Pd+ LaSrCrMn O (LSCM)</b>	LaSrGaMg O (LSGM)	300 $\mu$ m LSGM electrolyte	Screen- printing	850	H <sub>2</sub>	860	<a href="#">[24]</a>
					CH <sub>4</sub>	480	
<b>CuO+SDC</b>	SDC	electrolyte	Screen- printing	650	H <sub>2</sub>	122	<a href="#">[26]</a>
<b>CuCo–CeO<sub>2</sub></b>	YSZ	100 $\mu$ m anode	Screen- printing	750	H <sub>2</sub>	103	<a href="#">[33]</a>
					80% CH <sub>4</sub>	67	
					+20% O <sub>2</sub>		
<b>Mo<sub>y</sub>–M<sub>x</sub>Ce<sub>1-x</sub> O<sub>2-<math>\delta</math></sub>(M: Co, Ni, Cu</b>	GDC	electrolyte	Screen- printing	700	H <sub>2</sub>	350	<a href="#">[27]</a>
<b>Cu–Ni-YSZ</b>	YSZ	640 $\mu$ m anode	Electroless plating	750	H <sub>2</sub>	161	<a href="#">[17]</a>
					CH <sub>4</sub>	57	
<b>Cu, Co, Ni, +SDC</b>	YSZ	anode	Plasma spray	800	H <sub>2</sub>	475	<a href="#">[20]</a>

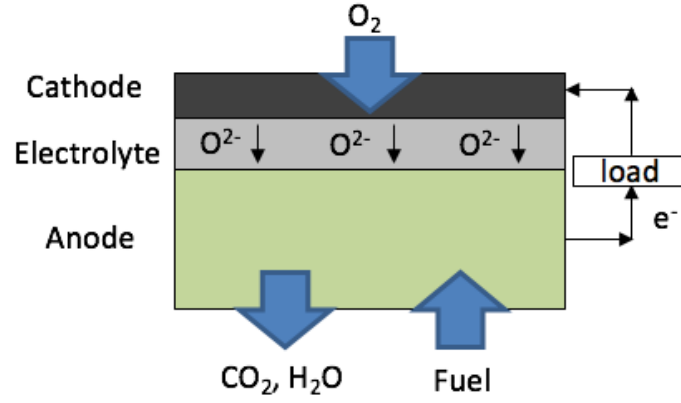


Fig. 2.1 Schematic diagram of an anode-supported SOFC



## 2.2 Permeability of Porous Ceramics

Most studies on permeability are based on Darcy' law, which is formulated on the experiments of a flow of water through beds of sand by Henry Darcy in 1856 [4]. The schematic diagram of the fundamental of the test is shown in Fig. 2.2 (a). Darcy got a linear relationship between the pressure gradient and the fluid velocity of measured at the end of tube. The Darcy equation can be written as

$$u = \frac{Q}{A} = -\frac{k \Delta P}{\mu \Delta L} \dots \dots \dots (2.7),$$

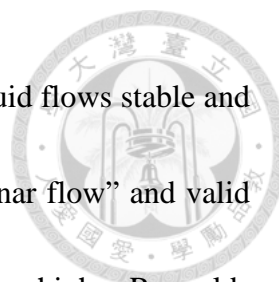
where  $u$  is velocity of water (m/s),  $Q$  is flow rate ( $\text{m}^3/\text{s}$ ),  $A$  is cross-sectional area of the flow ( $\text{m}^2$ ),  $k$  is permeability,  $\Delta P$  is a pressure drop between downstream pressure and upstream pressure (with a unit of Pa),  $\mu$  is viscosity ( $\text{Pa} \cdot \text{s}$ ), and  $\Delta L$  is length of flow (m). However, Darcy's law is only valid for slow, viscous flow, e.g. water or viscous liquid.

### 2.2.1 Darcy Flow and Non-Darcy Flow

Reynolds number (Re) is a dimensionless parameter to investigate the ratio of fluid inertia and viscous force [34]. It can be divided into laminar, transition and turbulent flows, which is shown in Fig. 2.2 (b). For a flow in a cylindrical pipe, Re is defined as below

$$\text{Re} = \frac{\rho u D}{\mu} \dots \dots \dots (2.8),$$

where  $\rho$  is a density of the flow ( $\text{kg}/\text{m}^3$ ) and  $D$  is the diameter of the pipe (m). When the



influence of the viscous force is greater than the inertial force, the fluid flows stable and has a Reynolds number smaller than one. This case is called “Laminar flow” and valid for Darcy’s law. On the contrary, transition and turbulent flows with a higher Reynolds number are non-Darcy flows, of which the flow patterns become disordered and irregular, as shown in Fig. 2.2 (c). As the velocity of flow increasing, non-linear deviation is observed.

In order to correct the Darcy equation for non-Darcy flow, a second order fitting of the velocity was proposed by Forchheimer in 1901[35] :

$$\frac{\Delta P}{\Delta L} = -\frac{\mu u}{k} + \beta \rho u^2 \dots \dots \dots (2.9),$$

where  $\beta$  is Forchheimer coefficient, or called non-Darcy coefficient.

**2.2.2 Non-Darcy Flow in Porous Media**

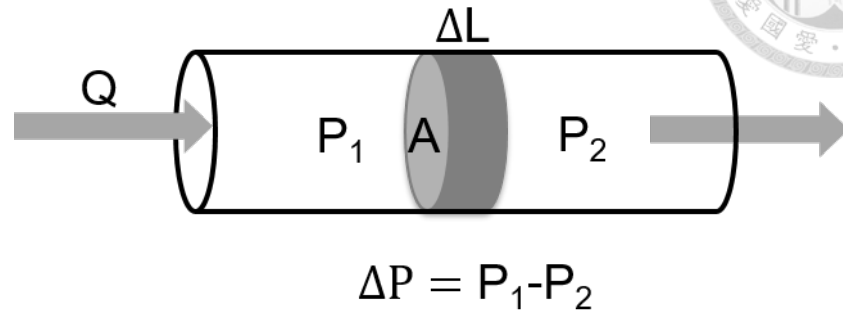
Unlike a pipe flow, the size of capillary and curved flow path may have influence on viscous force and inertial force. There is a way for determining either Darcy flow or non-Darcy flow in porous media is described as below. Reynold number which is defined as

$$Re = \frac{\rho du}{\mu} \dots \dots \dots (2.10),$$

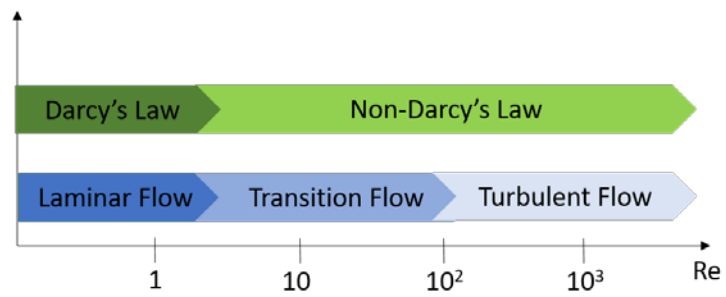
where  $d$  is diameter of the pore. The deviation from Darcy's linearity might occur from lower values of  $Re$ . In Fancher's report [35], non-Darcy flow started at  $Re = 0.4$ . Since the pore diameter is difficult to decide in some complex structure of porous media, the critical values of the  $Re$  for non-Darcy flow vary from 0.1 to 1000 in several researches [36-39]. So, Reynold number is not suitable as a criterion due to the varies geometries and states of porous media

According to Zheng's study, a new criterion, Forchheimer number ( $F_0 = \frac{k\beta\rho u}{\mu}$ ), is clearly defined and can applied to all kinds of porous media [5]. The critical values of Forchheimer number is from 0.005 to 0.2. Therefore, our test follows the Forchheimer number given by Zheng.

(a)



(b)



(c)

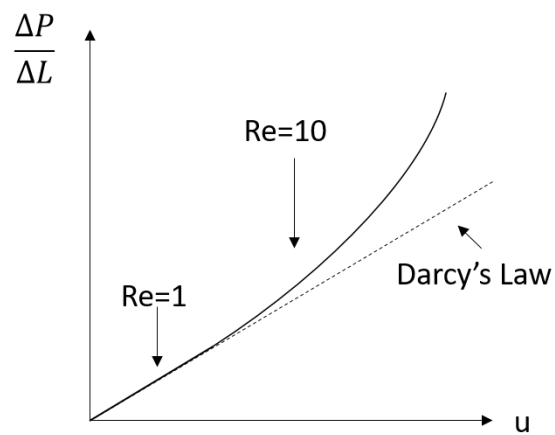


Fig. 2.2 Schematic diagram of (a) Darcy's Law and (b), (c) the relationship between Reynolds number and fluid flow velocity [40].



## 2.3 Thermocouple

Solid oxide fuel cell is a multilayer structure with different materials. Different coefficients of thermal expansion and interface reactions may cause deterioration of the cell during long-term test. Thus, an accurate control of the temperature of SOFC is needed. Therefore, a copper-based thermocouple is designed to operate in the temperature range of room temperature to 650 °C.

### 2.3.1 Principal of Thermoelectric Thermometry[41]

Electrical and thermal conductivity are a result of the migration of electrons. Electrons are non-mobile on ground state at 0 K as the description of Pauli exclusion principle and Fermi-Dirac distribution. When temperature increases, electrons absorb heat and transit to excited state. According to the principles, three thermoelectric effects would happen when two different metal materials are welded together.

(1) Seebeck effect: Two dissimilar metals are joined together and put the joint at hot environment ( $T_1$ ), the other end in room temperature ( $T_0$ ) as shown in Fig. 2.3. A voltage difference (Thermopotential) occurs because electron energy levels of each metal wire shift differently and had different electron concentration to cause the diffusion. So, the thermopotential resulted by a temperature difference ( $\Delta T$ ) can be written as below.



$$\Delta V = S_{AB} \Delta T \dots\dots\dots (2.11),$$

where  $S_{AB}$  is Seebeck coefficient.

(2) Peltier effect: When current flow through a junction between two dissimilar metals, the junction may absorb or release heat from surrounding. The direction of electrical current leads the sense of the heat exchange, which is written as:

$$\dot{Q} = (\pi_A - \pi_B) I \dots\dots\dots (2.12),$$

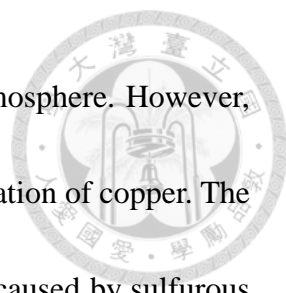
where  $\dot{Q}$  is absorption or release of heat energy,  $\pi_A$  and  $\pi_B$  are the Peltier coefficients of metals A and B, and I is the electric current.

(3) Thomson effect: If electrical current traverses a temperature gradient of a single metal wire, the heat exchange occurs. When the direction of electrons from cold to hot, the heat will be absorbed slightly. While the direction of electrons from hot to cold, the heat will release to reduce electron energy.

### 2.3.2 Common Thermocouple Types

Table 2.3 shows eight common types of the thermocouples, which are used in different temperature range and atmosphere. They can be divided into three types by their operating temperature. J and T types are mainly used at low to intermediate temperature. The material of negative electrode is coronel (Ni-45% Cu) and the material of positive is





iron and copper, respectively. The both can be used in reducing atmosphere. However, the upper temperature limit (350 °C) of T type is due to an easy oxidation of copper. The other concern, rusting and embrittlement of iron for J-type, may be caused by sulfurous atmospheres or subzero temperature.

K type is widely chosen for the use at high temperature ( $\leq 1260$  °C) in oxidation atmosphere. Because oxidation resistance of K type is better than E-, J- and T- type thermocouple. Owing to intergranular corrosion of alumel (Ni-5%Al) with sulfur and preferential vaporization of chromium, K type is not suitable in reducing, vacuum and sulfurous atmospheres.

R, S and B types are made by platinum and platinum-rhodium alloy wires. Compare to other types, thermopotential difference of these three types are not obvious at low temperatures. Thus, R, S and B types are mainly used in ultra-high temperature range ( $800$  °C $\ll$  $1700$  °C). They also should not be used in reducing atmosphere. Excessive grain growth of Pt and diffusion of Rh may affect stability of the temperature sensing capability under prolonged use.


This study wants to study copper alloy materials assembling for thermocouple using on Cu-based anode of SOFC. Thus, a thermocouple is desirable as it can be used in reducing atmosphere and is stable at SOFC operating temperature (650 °C).

### 2.3.3 Fabrication and Sealing Method of Thermocouple

In this study, a twisting and welding method are used to form the measuring junction of thermocouple. When temperature increases, different thermal expansion coefficient of two metals may cause separation of two wires. The twisting and welding method can provide additional strength to prevent this poor situation.

In order to isolate thermocouple from contamination of measuring sample, there are many different insulation materials are used to seal the thermocouple. In Wang's [42] report, he used a sealing glass ( $\text{TiO}_2\text{-Na}_2\text{O-SiO}_2\text{-B}_2\text{O}_3$ ) for Cu based thermocouple. He reported that the oxidation and grain growth may influence the stability of the thermocouple. Alumina tube is a common insulator commercially used. Therefore, this study uses alumina tube, instead of glass, to seal different thermocouples and observe their oxidation behavior and electrical properties.

Table 2.3 Types of Commercial Thermocouple



Type	Materials	Temperature (°C)	Properties
<b>T</b>	Copper (+) Nickel-45% Copper (-)	-200-370	1. Stable in Moist or reduction atmosphere; 2. Oxidation upon 300 °C.
<b>J</b>	Iron (+) Nickel-45% Copper (-)	0-760	1. Cannot used in sulfurous atmosphere above 540 °C; 2. Oxidation of iron is rapid above 540 °C.
<b>E</b>	Nickel-10% Chromium (+) Nickel-45% Copper (-)	-200-900	1. Unstable in reduction atmosphere; 2. Highest Seebeck coefficient.
<b>K</b>	Nickel-10% Chromium (+) Nickel-5% Aluminum and Silicon (-)	-200-1260	Unstable in reduction, vacuum sulfurous atmosphere.
<b>N</b>	Nickel-14% Chromium-1.5% Silicon (+) Nickel-4.5% Silicon-0.1% Magnesium (-)	0-1260	N/A
<b>R</b>	Platinum-13% Rhodium (+) Platinum (-)	0-1480	Cannot used in reducing atmosphere, nor containing metallic or nonmetallic vapor.
<b>S</b>	Platinum-10% Rhodium (+) Platinum (-)	0-1480	
<b>B</b>	Platinum-30% Rhodium (+) Platinum-6% Rhodium (-)	870-1700	

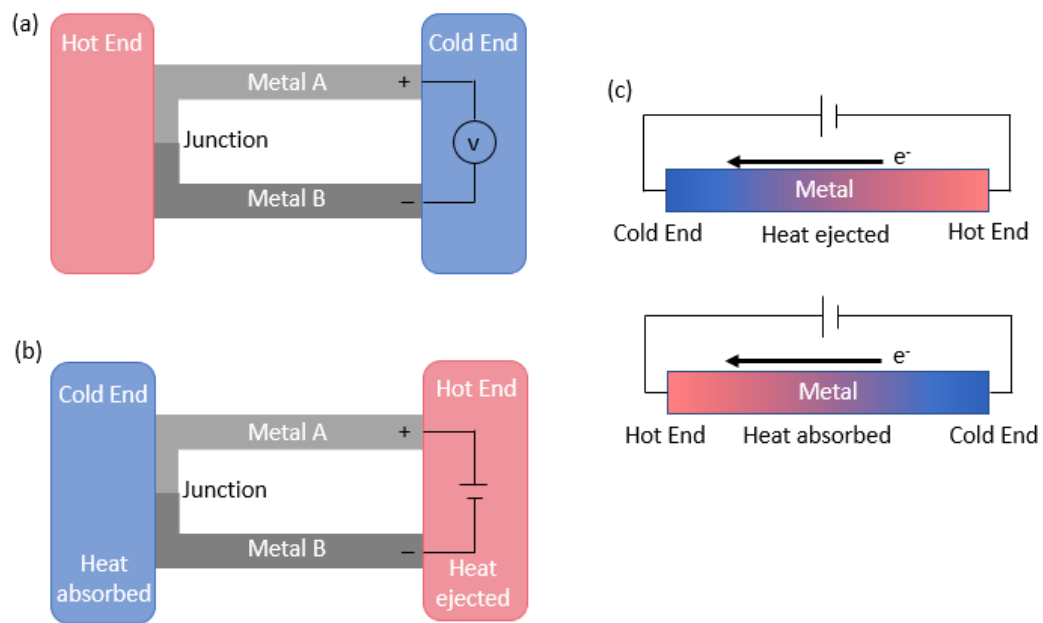


Fig. 2.3 Schematic diagrams illustrating (a) Seebeck effect, (b) Peltier effect, and (c) Thomson effect.

## Chapter 3 Experimental Procedure




### 3.1 Materials

Nickel oxide powder (NiO, NICO LTD, F grade, Japan), copper oxide powder (CuO, First Chemical Works (第一化工), Taiwan), 8 mol% yttria-doped zirconia powder (8YSZ, Dai-ichi, Japan) and meso-carbon micro-black (MCMB, National Chung-Shan Institute of Science and Technology (中山科學院), Taiwan) are used as anode materials. Ethanol (95% purity, Taiwan Tobacco and Liquor Corporation, Taiwan) and DI water are two solvents for the preparation of slurry. D-134 (ammonium salt homopolymer with 2-propenoic acid group, Dai-Ichi Kogyo Seiyaku Co. Ltd., Japan) and Darvan C (ammonium salt of polymethyl acrylate anionic, Venderbilt, USA) are used as dispersant in aqueous anode slurry.

Five metal wires: pure Copper (C11000, as abbreviated as "C"), Copper-11wt% Nickel alloy (C70600, KANTHAL, Sweden, "C11N"), Copper-38wt% Zinc alloy (C26000, "CZ"), Copper- 9wt% Nickel- 6% Tin (C72700, MIRDC, Taiwan, "C9N6S") and pure Nickel (Nilaco, Japan, "N") are tested and made into thermocouples.

### 3.2 Anode Preparation and Cell Assembly

NiO, CuO and 8YSZ powders were mixed in three mass ratios, named  $N_{100}Z$ ,  $C_{50}N_{50}Z$  and  $C_{100}Z$ , which are given in Table 3.1. NiO and 8YSZ powders were dispersed



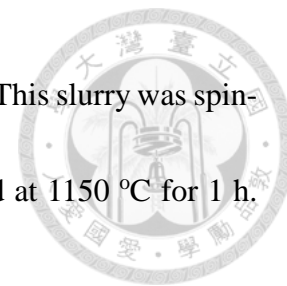
in ethanol. While CuO was dispersed in H<sub>2</sub>O with 1 wt% D-134. Based on Chen's process [43], the mixture of NiO, CuO and 8YSZ was then ball-milled for 24 h, followed MCMB been added into the slurry and ball-milled for additional 1 h. The mixture was rotary-drying and the dried anode powder was sieved through a screen of 100 mesh. The anode disks were made by die-pressing at 70.0 MPa in a diameter of 30 mm, followed pre-sintering the disks at 1000 °C for 1 h.

A nano-sized 8 mol% yttrium stabilized zirconia powder (8YSZ-N, Tsinghua University, China) was dispersed into DI water with D-134 as a dispersant. To be used as a flat layer [44], 8YSZ-N slurry was diluted to 1.0 wt% and spin-coated on an pre-sintered anode substrate by the spinning conditions of 3000 rpm, 60 s and 1 cycle.

The other slurry, 5 wt% 8YSZ-T slurry as electrolyte material starting from the 8YSZ (TOSOH, Japan) powders, were prepared with ethanol and ball-milled for 24 h. Then spin-coated on the flat layer was conducted by the conditions of 3000 rpm, 60 s and 2 cycles.

Then the spin-coating of NiO/YSZ slurry for anode function layer was prepared by mixing NiO, 8YSZ with ethyl cellulose (E0266, TCI, Tokyo, Japan) and terpineol (95%, Showa Chemical Industry Co. Ltd., Japan) in mass ratio of 15:15:2:68. The mixture was ball-milled for 24 h and spin-coated in the conditions of 5000 rpm, 60s and 2 cycles.

Finally, a LSCF with PEG slurry was used as cathode source. This slurry was spin-coated on electrolyte in the condition of 1000 rpm, 20s and sintered at 1150 °C for 1 h. The flowchart of the single cell preparation was shown in Fig. 3.1.



### **3.3 Preparation of Thermocouple**

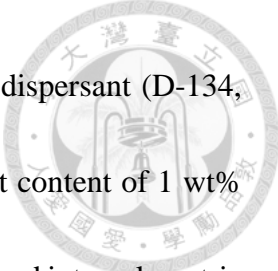
C, C11N, CZ, C9N6S and N wires are cleaned by putting into ethanol and then 2 vol % diluted hydrochloric (HCl) acid for removing oxide layer on the wire surface. Then dry the samples in vacuum chamber for preventing from oxidation.

Five types of thermocouple were prepared Twisting and welding methods [45] was used in this study in order to increase the strength of coupling point and to prevent separation of two metal wires. Two wires were twisted in one end and welded by a fine-wire welder (MINI-2K5A-2, Thermoway Ind. Co, Ltd. (崧啟), Taiwan). After that, the thermocouple was put into a alumina tube (inside diameter: 6.50 mm) as an electric insulation layer.

### **3.4 Property Characterization**

#### **3.4.1 Sedimentation Test**

NiO, CuO, 8YSZ and MCMB powders are the anode materials used in this study. In order to disperse powders and mix homogeneously, the slurries of sedimentation test



were using water or alcohol based solutions. Slurries with different dispersant (D-134, Darvan C) were prepared in a solid loading of 5 vol% and dispersant content of 1 wt% based on the mass of powder. After ball-milled 24 h, the slurry was poured into volumetric glass cylinder to be measured the origin height ( $H_o$ ) of the slurry and the final height ( $H_f$ ) of the suspension. A plot of  $H_f/H_o$  versus sedimentation time ( $t$ ) was plotted to determine which solvent was better for dispersing powder.

### 3.4.2 XRD Analysis

Crystallographic properties were examined by X-ray diffractometry (TTRAX 3, Rigaku, Japan) using Cu  $K\alpha$  radiation. Diffraction patterns were collected from  $2\theta$  ranging between  $10^\circ$  and  $90^\circ$  at a scan rate of  $4^\circ \text{ min}^{-1}$  in a step of  $0.02^\circ$ .

### 3.4.3 SEM Analysis

Scanning electron microscope (JSM 6510, JEOL, Japan) was used to analyze the surface morphology by secondary electron image (SEI) mode. Qualitative and quantitative analyses of sample composition were conducted by energy-dispersive X-ray spectroscopy (EDS, Oxford Instruments, UK).





### 3.4.4 Density Measurement

The density of bulky sample could be determined by Archimedes' method. The bulky density  $D_b$  was calculated as below.

$$D_b = \frac{W_1 \times \rho_w}{W_2 - W_3} \dots\dots\dots(3.1),$$

where  $W_1$  = the mass of dried sample in air,  $W_2$  = the mass of the sample including the water filled in open pores,

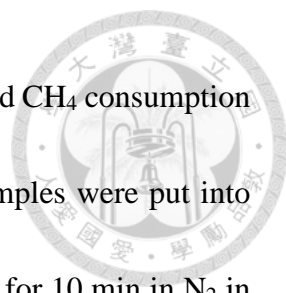
$W_3$  = the mass of the sample immersed in the water,

$\rho_w$  = density of water ( $\text{g/cm}^3$ ).

First, ultrasonicing the sample surface in water bath; Then putting the sample on the sieve all immersed under the water surface to measure  $W_3$ ; Afterward, taking out the sample and putting on an electronic balance to get  $W_2$ ; Finally, drying the sample in oven and weighing it again to get  $W_1$ . As a result,  $D_b$  can be calculated by Eq. (3.1). The relative density and porosity could be measured from  $D_b/D_{th}$  and  $1 - D_b/D_{th}$  ( $D_{th}$  is the theoretical density).

### 3.4.5 Thermogravimetric Analysis (TGA)

Reducibility of anode materials and thermally reactions can be quantified by a TGA



test (STA 449 F3 Jupiter, Netzsch). It was conducted to identify H<sub>2</sub> and CH<sub>4</sub> consumption of a fuel flowing through Ni-Cu based anode materials. 200 mg samples were put into Al<sub>2</sub>O<sub>3</sub> crucible preheated from room temperature to 120 °C and hold for 10 min in N<sub>2</sub> in order to eliminate the water on the powder surface. Without taking out from instrument, the sample was heated to 700 °C at 10 °Cmin<sup>-1</sup> in a fixed ratio of 20% H<sub>2</sub> or 20% CH<sub>4</sub>. The mass loss of sample was recorded during the heating process as well as consumption of H<sub>2</sub> and CH<sub>4</sub>. Oxidation of five metal wires were analyzed by Differential Scanning Calorimetry (DSC, TA Q600, TA, US). The heating process is from room temperature to 800 °C in air and heating rate is 10 °Cmin<sup>-1</sup>.

### 3.4.6 Permeability Test

Gas permeability of anodes was measured by previous mentioned Forchheimer equation and tested in the equipment shown in Fig. 3.2. The disk of sample was put on a zirconia tube and sealed by ceramic paste at 700 °C in hydrogen atmosphere. Then a gas flow of methane was reformed at 650 °C for 2 h. In order to observed the difference of permeability before and after reacting with the methane. The flow rate and pressure drop was recorded by a flowmeter and pressure gauge. Furthermore, a gas product was collected at either 300 °C, 600 °C or 650 °C in every 30 min to test catalytic properties of anode.



### 3.4.7 Gas Chromatography

The gaseous products of CH<sub>4</sub> and H<sub>2</sub> were analyzed by two chromatography/thermal conductivity detector analyzers (GC/TCD, 8900GC, China Chromatography Co., Taipei, Taiwan). The GCs are installed with the same packed columns (60/80 Carbonxen-1000, 15 ft × 1/8 in SS, Sigma-Aldrich, Saint Louis, MO, USA). Different carrier gases of helium (He) for the analyses of CH<sub>4</sub> and argon (Ar) for that of H<sub>2</sub> were used, respectively. The concentrations of every gaseous species were calculated by the obtained calibration curves.

### 3.4.8 Conductivity Measurement

A DC four-probe method was used to measure the current and voltage of wire and anode samples, which is shown in Fig. 3.3. The resistance is calculated by eqs. (3.2), (3.3) and (3.4).

$$\sigma = \frac{1}{\rho} \dots\dots\dots (3.2),$$

$$R = \rho \frac{l}{A} \dots\dots\dots (3.3),$$

$$R = \frac{V}{I} \dots\dots\dots (3.4),$$

where  $\sigma$  is the conductivity (Scm<sup>-1</sup>),  $\rho$  is the resistivity (Ωcm), R is the resistance (Ω), V is the voltage (Volt), I is the current (Amp), l is the length (cm) of the wire sample, and

A is the cross-section of the sample ( $\text{cm}^2$ ). Table 3.2 shows the diameter and length of the sample wires.



After four probes of testing electrodes connected to the wire surface, a current of 2.00 Amp, the voltage (V) shown on the four-probe machine was recorded. Then we heated the sample step-by-step to 700 °C in an interval of 50 °C, and recorded the conductivity at different temperatures.

### **3.4.9 Thermopotential measurement**

In this experiment, thermocouple was heated from room temperature to 700 °C to measure thermopotential and Seebeck coefficient for finding suitable thermocouple used in SOFC operating temperature. Then thermocouple was tested at 200 °C, 400 °C, 650 °C in a furnace and last for more than 100 h. The change of thermopotential was recorded so that we can observed the deterioration of thermocouple.

The measurement of thermocouple were also tested in two situations. One is put the thermocouple in a furnace at a constant temperature (200 °C, 400 °C, and 600 °C), the other one is put the thermocouple in a furnace and heating up from room temperature to a specified temperature (200 °C, 400 °C, and 600 °C). Then start to record the thermopotential when the furnace reached the temperature. From the potential change, we can know how long thermopotential takes to get stable.



### 3.4.10 Thermal Expansion Analysis (Dilatometer, DIL)

The volume changes of sample caused by expansion and shrink during heating/cooling process was measured by a dilatometer (LINSEIS, L75HS 1600C). The coefficient of Linear and volume thermal expansion (CTE) is calculated by Eqs. (3.5) and (3.6) as below.

$$\alpha = \frac{1}{L} \cdot \frac{\Delta L}{\Delta T} \dots \dots \dots (3.5)$$

$$\gamma = \frac{1}{V_0} \cdot \frac{\Delta V}{\Delta T} = \frac{3}{L} \cdot \frac{\Delta L}{\Delta T} \dots \dots \dots (3.6)$$



Table 3.1 Abbreviation name of anode materials

Sample	Composition (mass%)
<b>N<sub>100</sub>Z</b>	CuO:NiO:8YSZ:MCMB = 0 :40:40:20
<b>C<sub>50</sub>N<sub>50</sub>Z</b>	CuO:NiO:8YSZ:MCMB = 20:20:40:20
<b>C<sub>100</sub>Z</b>	CuO:NiO:8YSZ:MCMB = 40:0 :40:20



Table 3.2 Diameter and length of four Cu-based alloy and Ni wires

<b>Material</b>	<b>Diameter (cm)</b>	<b>Length (cm)</b>
<b>C (Cu)</b>	0.100	1.00
<b>CZ (Cu-38%Zn)</b>	0.102	1.00
<b>C11N (Cu-11% Ni)</b>	0.124	1.00
<b>C9N6S (Cu-9%Ni-6%Sn)</b>	0.175	1.00
<b>N (Ni)</b>	0.100	1.00

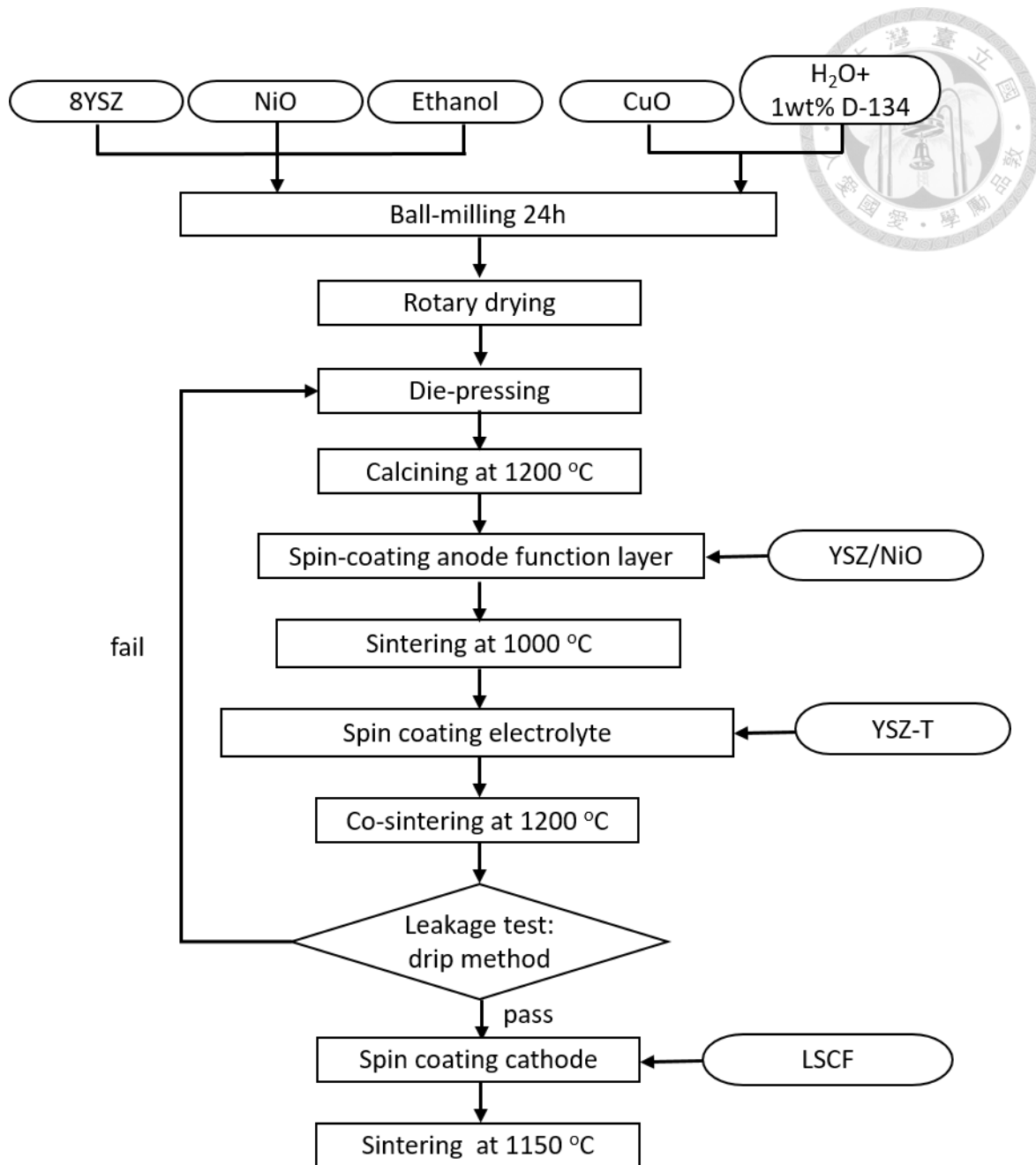


Fig. 3.1 Flowchart of single cell preparation.



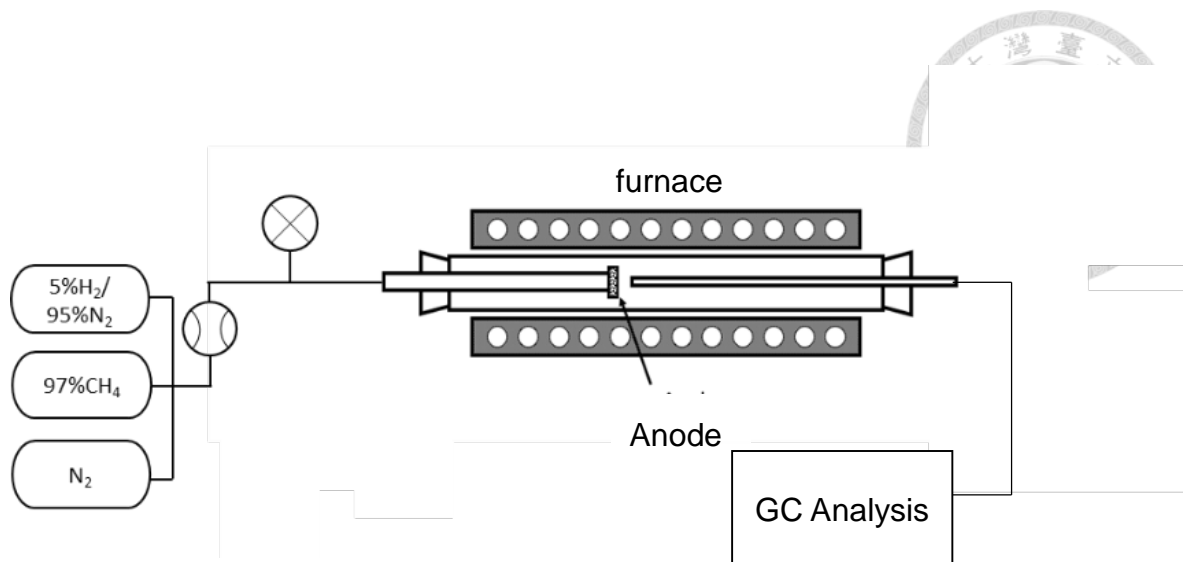


Fig. 3.2 Schematic diagram of GC and permeability test.

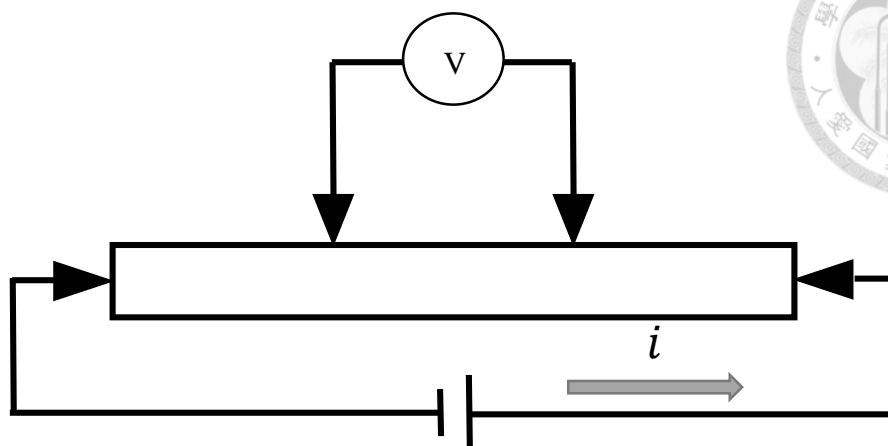


Fig. 3.3 Schematic diagram of four probe conductivity test.

## Chapter 4 Results and Discussions

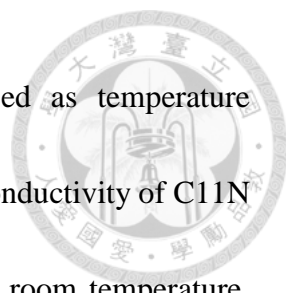
### 4.1 Electric Properties of Cu-based Alloy

#### 4.1.1 Conductivity of Cu-based Alloy

DC four-probe method are used to measure the conductivity of Cu alloy wires from room temperature to 700 °C in air. Fig. 4.1 shows the electrical conductivities of C, C11N, CZ, and N wire samples. As the temperature increases, the conductivities of these four wires decrease. The same phenomenon was found in Wolff's reports [46].

The bandgap of metals is generally small and thus the electrons can easily jump to conduction band. However, thermal motion caused by increasing temperature makes the electrons scatter and disturb their mean free path. As a result, drift velocity and mobility of the electrons decrease [47]. So that the conductivity of metal decreases when temperature rises. The theoretical conductivity of Cu and Ni metal are  $59.6 \times 10^6 \text{ S}\cdot\text{m}^{-1}$  and  $14 \times 10^6 \text{ S}\cdot\text{m}^{-1}$ , respectively [1]. While the conductivity of Cu and Ni wires of this measurement is  $59.2 \times 10^6 \text{ S}\cdot\text{m}^{-1}$  and  $13.5 \times 10^6 \text{ S}\cdot\text{m}^{-1}$  at room temperature. The measured values are 0.67% and 3.57% lower than the theoretical values. That may be possibly due to impurity (mainly oxygen content) in the wires. The conductivity of the Cu wire at 650 °C was  $16.9 \times 10^6 \text{ S}\cdot\text{m}^{-1}$  and decreased 71.5%. In contrast, the conductivity of the Ni wire at 650 °C was  $3.07 \times 10^6 \text{ S}\cdot\text{m}^{-1}$  and decreased 77.4%. Therefore, Cu wire is more suitable using as current collector than the Ni.



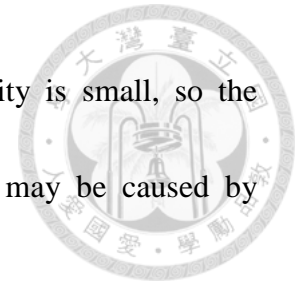


The conductivity of pure Cu wire is obviously decreased as temperature increasing, different from that of C11N and CZ wire samples. The conductivity of C11N and CZ samples are  $5.36 \times 10^6 \Omega^{-1} \cdot \text{m}^{-1}$  and  $10.57 \times 10^6 \Omega^{-1} \cdot \text{m}^{-1}$  at room temperature, respectively. The conductivity degradation of these two samples tested at 650 °C are 19.3% and 36.2%. The reason for the different electrical performance between pure Cu and Cu alloys may be due to grain growth of Cu-based materials and surface oxidation of the wires during testing.

In the Arrhenius form diagram, electrical conduction mechanism of C, C11N, CZ and N are showed in Fig. 4.2. Different activation energy ( $E_a$ ) indicates different electrical conduction mechanism. The curves of C and N are complicate. The reason may due to surface oxidation or changes in microstructure. However, both C11N and CZ data shows only one slope, implying activation energy level from low to high temperature. As a result, C11N and CZ are electronic conductive dominant. And the  $E_a$  of C11N and CZ are  $3422.99 \text{ Jmol}^{-1}$  and  $2512.20 \text{ Jmol}^{-1}$ , respectively.

Fig. 4.3 shows electrical conductivities of C, C11N and CZ wire samples tested at room temperature in different curvatures. In this test, 10 cm wires are bent into circle with three different curvatures: 2.5 mm, 3.35 mm and 5.5 mm. As the curvature decrease, the conductivity of pure Cu decreases. While the conductivities of C11N and CZ are slightly rising and then declined in considering the data variation. The reason of the conductivity

increase is not known yet. The deviation of Cu alloy conductivity is small, so the conductivity decrease at different curvatures is significant. This may be caused by different hardness or/and Young's modulus of C, C11N and CZ.



In Haung's report [48], the hardness of C, CZ, C11N and C9N6S are tested by Vickers test in air at room temperature. The data are shown in Table 4.1. The hardness of the as-received C, C11N, CZ and C9N6S are 1.86 GPa, 2.38 GPa, 2.98 GPa and 3.93 GPa, respectively. And their Young's modulus are 89.9 GPa, 126 GPa, 103 GPa and 112 GPa. Copper has lowest Young's modulus and hardness. When copper wire was bent, there might generate more dislocations and resulted in a lower conductivity. Thus, the conductivities of two copper alloys are more stable when curvature is changed.

Five wires are tested by TGA analysis in air from room temperature to 800 °C so as to observe the oxidation reaction. The weight increments from high to low are C, C11N, C9N6S, CZ and N, as shown in Fig. 4.4 (a). The DSC results are shown in Fig. 4.4 (b). After temperature was higher than 200 °C, all of the wires started to oxidize and had exothermic peak.

#### **4.1.2 Seebeck coefficient of Thermocouples**

In order to measure temperature in SOFC or metal mold, Cu-based wires were welded in couple (made into 5 thermocouples). To record thermopotential of the



thermocouples at different temperatures and calculate Seebeck coefficient for observing temperature sensitivity of thermocouple.

Fig. 4.5 shows the thermopotential of five thermocouples heating from room temperature to 700 °C. The thermopotential rose as temperature increased. The reason is that the amount of excited electrons are increasing in high temperature side. This caused different numbers of conducted electrons to be higher between cold side and hot side, then the thermopotential increased.

The relationship between thermocouple and temperature difference can be written as

$$E= A + B(\Delta T) + C(\Delta T)^2 \dots\dots\dots(4.1),$$

Where E is thermopotential in specific temperature (mV), A, B and C is experimental value,  $\Delta T$  is temperature difference between cold and hot sides. Then Seebeck coefficient is obtained by differentiating Eq. (3.1),

$$S= \frac{dE}{dT} \dots\dots\dots(4.2).$$

Fig. 4.6 shows the Seebeck coefficient of five thermocouples at different temperatures. The values also represent the temperature sensitivity of thermocouples. From high to low, the Seebeck coefficient of C-C11N, C11N-CZ, C-C9N6S, C-N and C-CZ at 650 °C is 0.0614 mV $k^{-1}$ , 0.0603 mV $k^{-1}$ , 0.0398 mV $k^{-1}$ , 0.0326 mV $k^{-1}$  and 0.0032 mV $k^{-1}$ . Thus, C-C11N has best temperature sensitivity in the range 450 °C to 700 °C.

Besides, C-CZ is not suitable as a thermocouple for its low Seebeck coefficient.



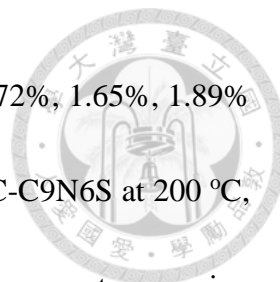
### 4.1.3 Short-term Thermopotential of Thermocouples

One of the purposes of the thermocouple development in this study is for in-situ measurement of temperature. Fig. 4.7, Fig. 4.8 and Fig. 4.9 show the thermopotentials of these three types of thermocouples tested at 200 °C, 400 °C and 600 °C in 5 min from test starts.

In Fig. 4.7(a), the thermopotentials of C-C11N, C-CZ , C-C9N6S, C-N and C11N-CZ thermocouples tested at 200 °C are 3.30 mV, 0.31 mV, 2.67 mV, 2.54 mV and 3.57 mV, respectively. They were all gradually increased to reach their steady state. Compared to Fig. 4.5, the variation of these four samples are 3.30%, 3.13%, 0.26%, 2.68% and 2.94%. However, the thermopotential of C11N-CZ has tested three times and has big error in Fig. 4.7(b) . This may be caused by needle crystal of ZnO, which has mentioned in Zhou's report [26].

Thermopotentials of C-C11N, C-CZ, C-C9N6S, C-N and C11N-CZ thermocouples tested at 400 °C are 9.58 mV, 0.87 mV, 7.42 mV, 7.73 mV and 10.59 mV as shown in Fig. 4.8. The variation of them are 1.7%, 3.85%, 1.55%, 1.53% and 6.29%. Meanwhile, the thermopotentials of C-C11N, C-CZ, C-C9N6S, C-N and C11N-CZ thermocouples tested at 600 °C are 20.20 mV, 1.422 mV, 13.96 mV, 12.98 mV and 20.13 mV respectively, as

shown in **Fig. 4.9**. The deviation of the thermocouples are 1.39%, 0.72%, 1.65%, 1.89% and 1.04%. In summary, the deviation of C-CZ, C-C11N, C-N and C-C9N6S at 200 °C, 400 °C and 600 °C are smaller than 5.00 %, which is capable of doing temperature sensing and has a short response time. In contrast, C11N-CZ showed huge error bar and deviation at low temperature.



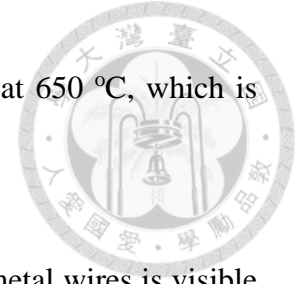
#### 4.1.4 Long-term Thermopotential of Thermocouples

In order to understand the time effect on the degradation of thermopotential. Three thermocouples including C-C11N, C-C9N6S, C-N and C11N-CZ were prepared and tested at 200 °C, 400 °C and 650 °C for more than 100 h. Fig. 4.10 shows the results of the time dependence test of thermo-potential of C-C11N and C11N-CZ thermocouples at 200 °C in air. The thermopotential of C-C11N and C11N-CZ are 3.57 mV and 3.30 mV after 16 days. The change of thermopotential in the two materials are, 1.97% and 3.80%, respectively.

In Fig. 4.11, the thermopotentials of C-C11N, C-C9N6S, C-N and C11N-CZ tested at 400 °C are 10.03 mV, 6.69 mV, 7.79 mV, 10.59 mV, respectively. The variation of these four samples are 5.68%, 4.48%, 1.14%, and 1.51%. Meanwhile, the thermopotentials of C-C11N, C-C9N6S and C-N thermocouples tested at 650 °C are 23.53 mV, 14.68 mV and 14.47 mV, as shown in **Fig. 4.12**. The variation of them are



1.48%, 1.23% and 1.24%. Both have less drift in thermopotential at 650 °C, which is feasible to apply as a temperature sensor on the anode of SOFC.



After long term test at 650 °C for 100 h, the oxide layer of metal wires is visible to the naked eye. So, we also observed microstructure of C, C11N, C-C9N6S and N before and after the test in Fig. 4.13. The surface of copper wire before heat treatment is much smoother than after heat treatment, which are shown in Fig. 4.13 (a) and (b). The oxide layer may be peeled off because of grinding. In Fig. 4.13 (d) and (f), the average thickness of C11N and C9N6S oxide layer are 4.72  $\mu\text{m}$  and 48.38  $\mu\text{m}$ . Tin is easier to oxide than copper and nickel. So, C9N6S has thicker oxide layer after long term test. And the oxidation of nickel wire is not obvious in Fig. 4.13 (h). However, all of these four wires have sufficient metal content to translate electron and maintain stable thermopotential.

To choose optimal thermocouple and conductivity of wires, there are four criteria:

(1) High Seebeck coefficient for temperature sensitivity, (2) less response time, (3) less drift of thermopotential in long-term test, and (4) less change of microstructure at 650 °C.

Therefore, C-C11N is the best thermocouple to match these requirements, C-C9N6S and C-N are the second and third choice.

Table 4.1 Young's modulus and hardness of Cu-based alloys [courtesy by Yi-Ting, [48]]

Sample	Young's modulus (GPa)	Std.	Hardness (GPa)	Std.
C	89.9	2.17	1.86	0.07
CZ	103	2.54	2.98	0.15
C11N	126	8.97	2.38	0.14
C9N6S	134	3.26	3.93	0.31

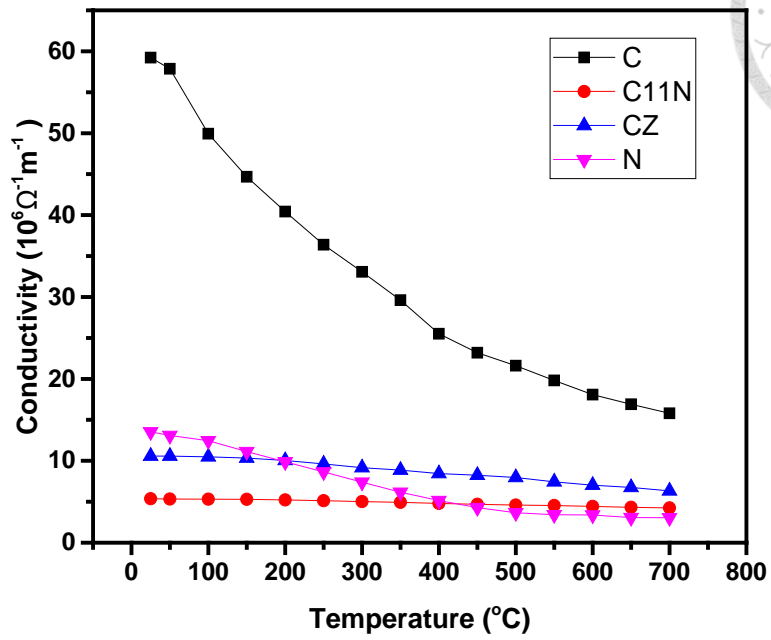


Fig. 4.1 Electrical conductivities of C, C11N, CZ and N wire samples tested from room temperature to 700  $^{\circ}\text{C}$  in air.

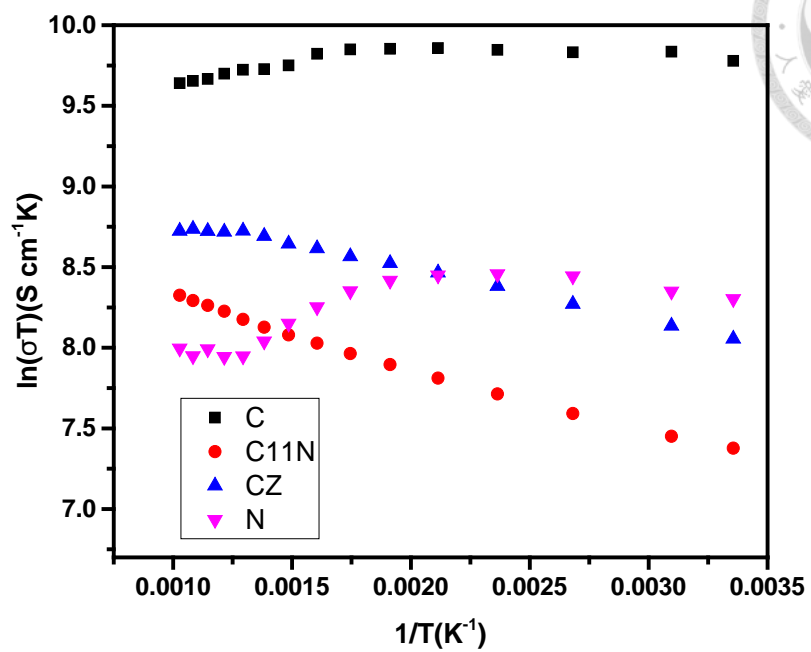


Fig. 4.2 Arrhenius plots of  $\sigma T$  versus  $1/T$  of four wires.

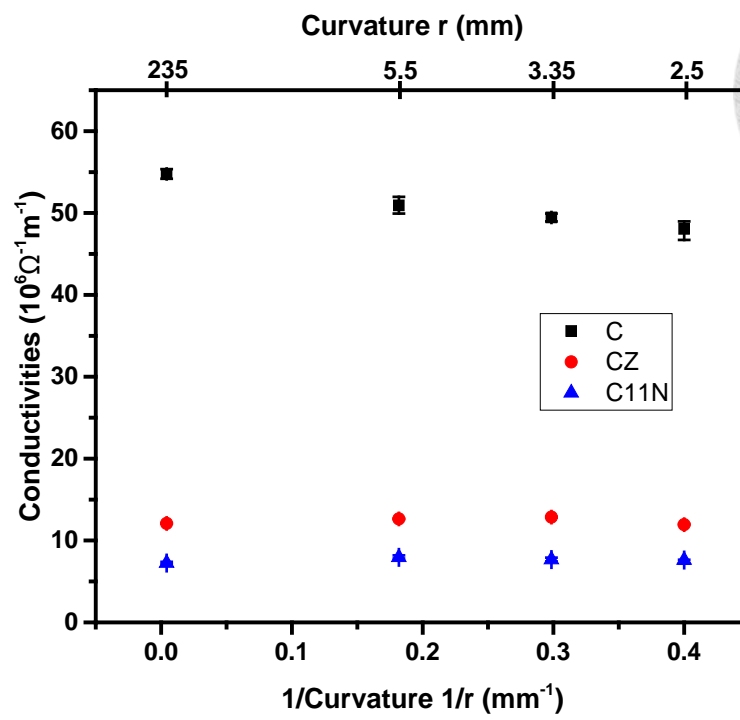


Fig. 4.3 Electrical conductivities of C, C11N and CZ wire samples in different curvatures tested at room temperature.

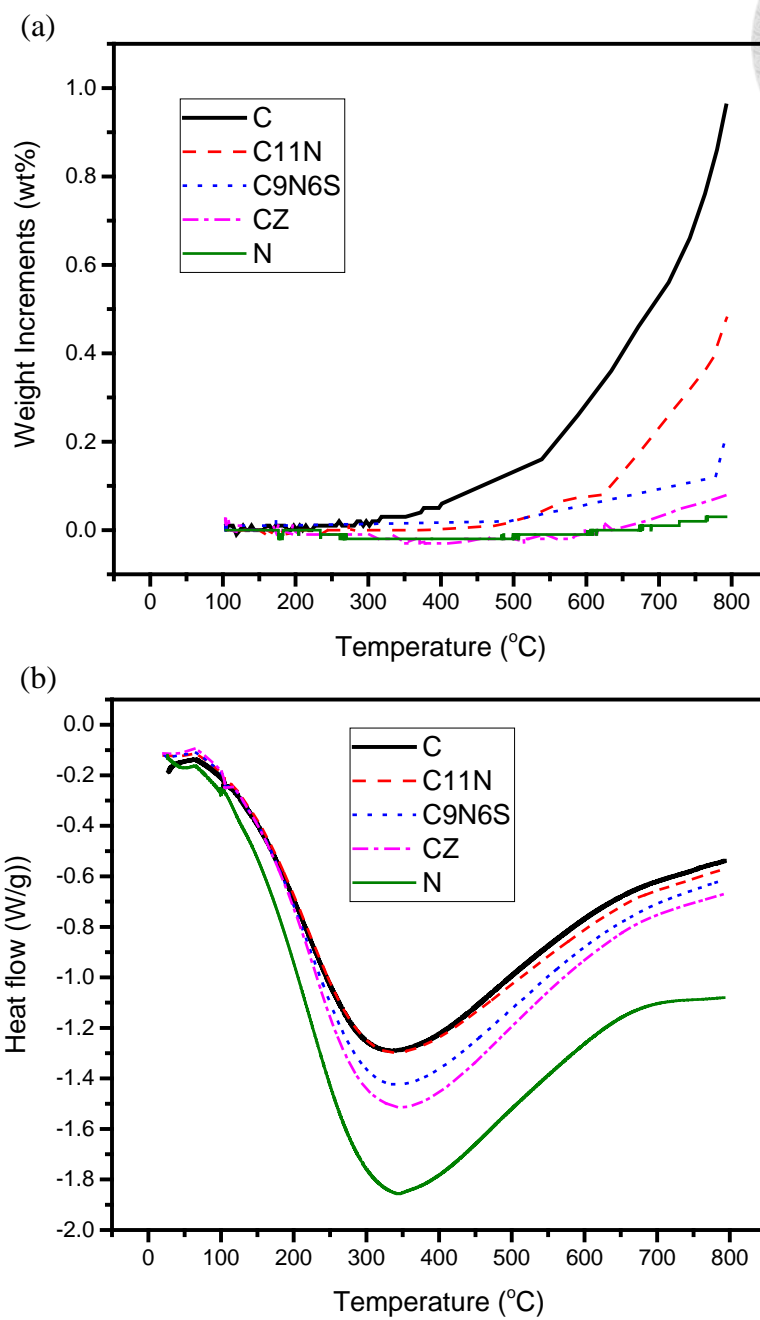


Fig. 4.4 (a) TGA and (b) DSC analysis result of five wires (C, C11N, C9N6S, CZ, and N) in air.

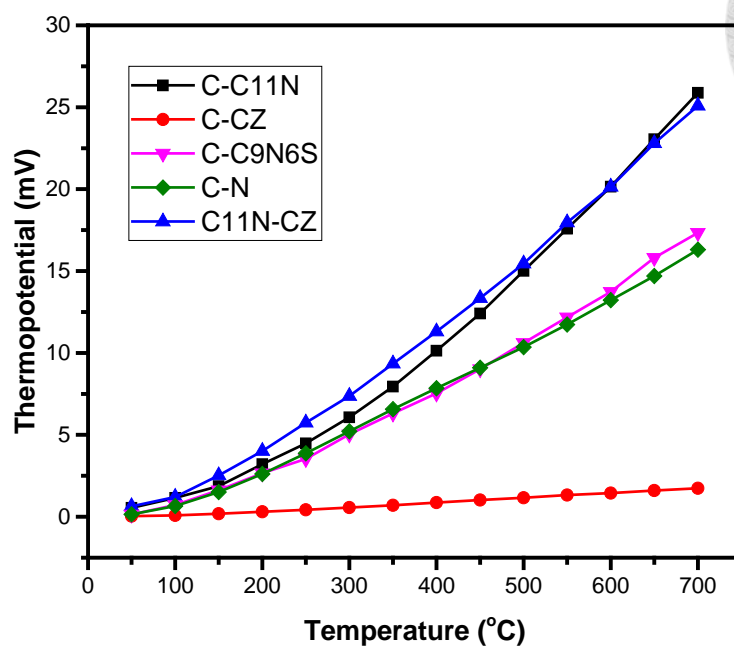


Fig. 4.5 Thermopotential plotted against temperature of five thermocouples.

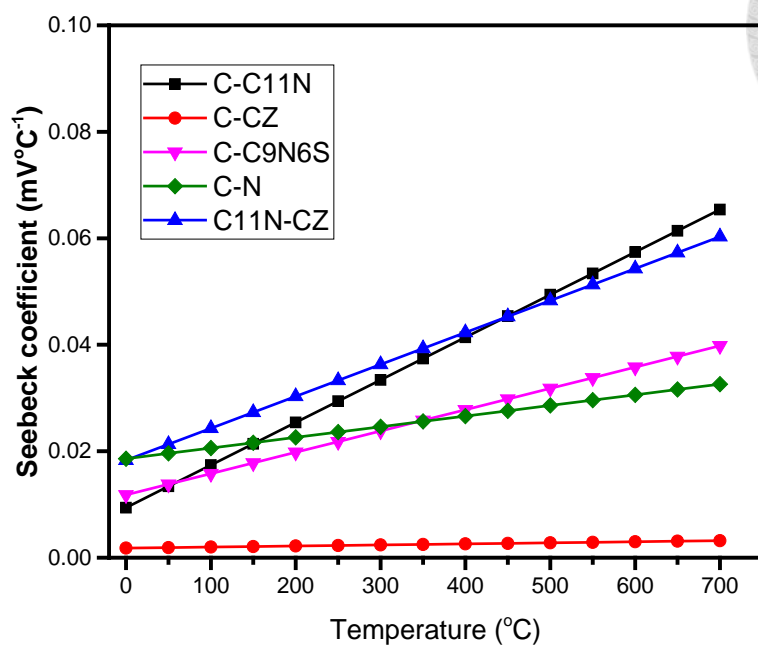


Fig. 4.6 Seebeck coefficient versus temperature of three thermocouples.



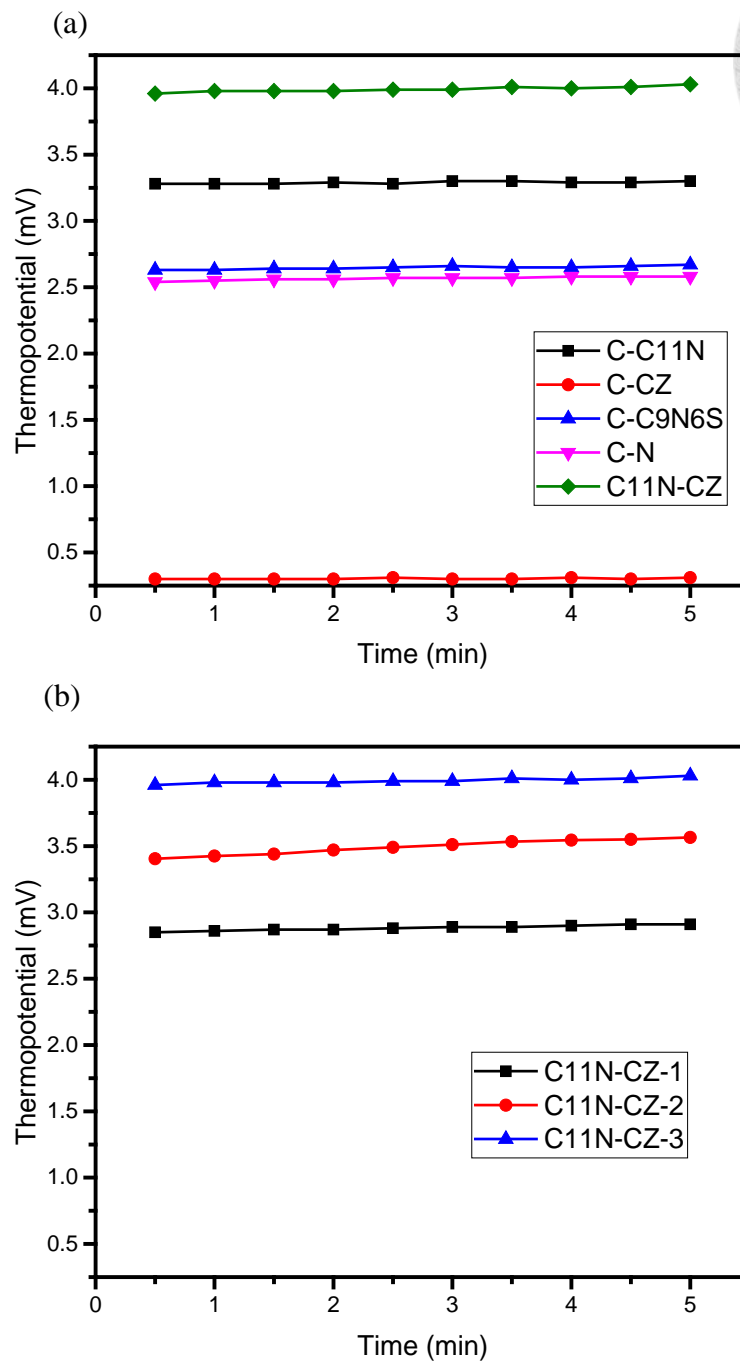


Fig. 4.7 (a) Thermopotentials of five types of thermocouples tested at 200 °C in first 5 min.(b) There are big variations on C11N-CZ when test three times.

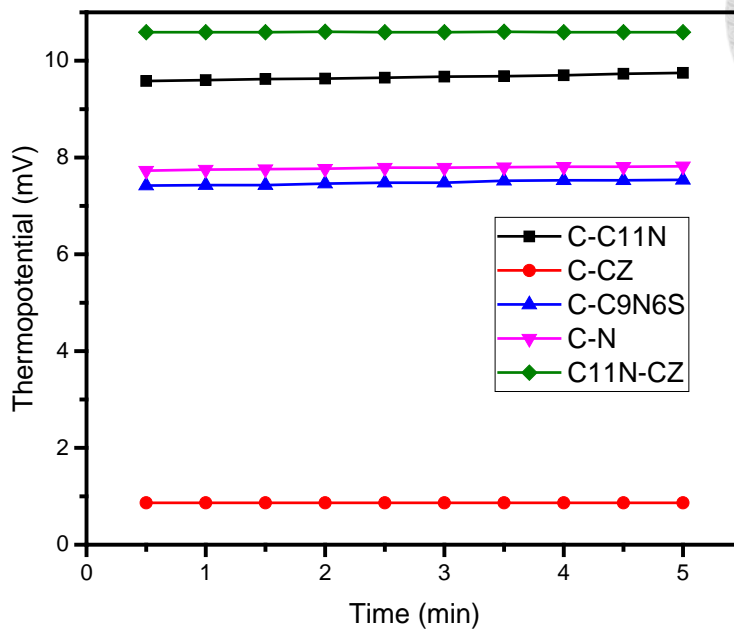


Fig. 4.8 Thermopotentials of five types of thermocouples tested at 400 °C in first 5 min.

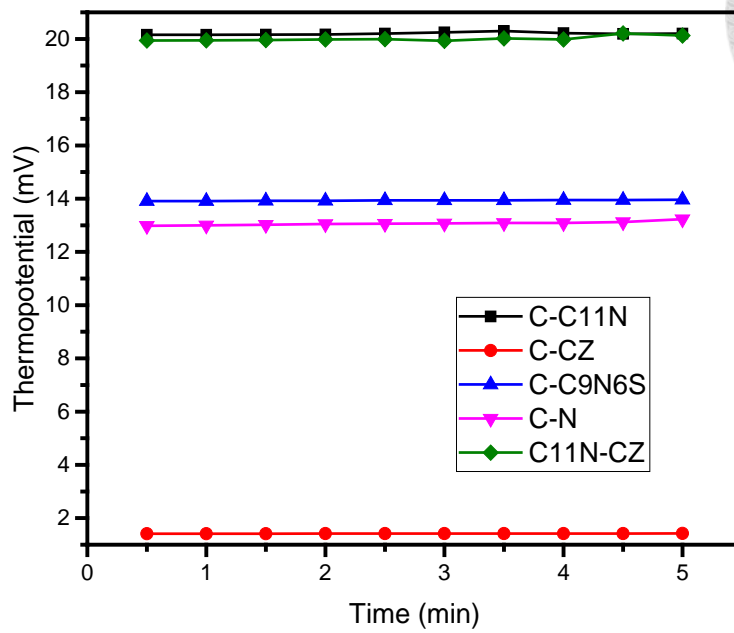


Fig. 4.9 Thermopotentials of five types of thermocouples tested at 600 °C in first 5 min.

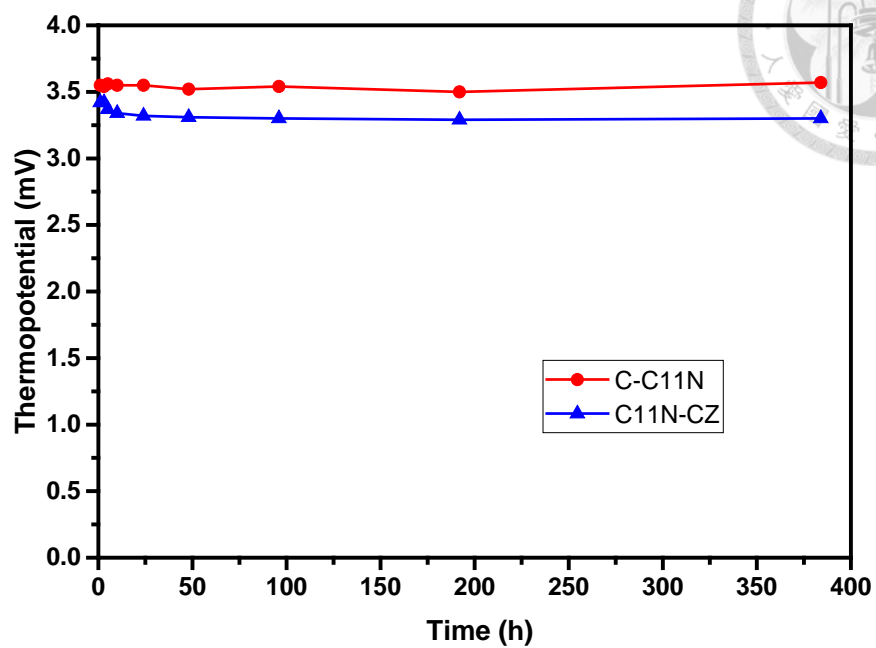


Fig. 4.10 Time dependence test of thermo-potential of C-C11N and C11N-CZ thermocouples at 200 °C in air.

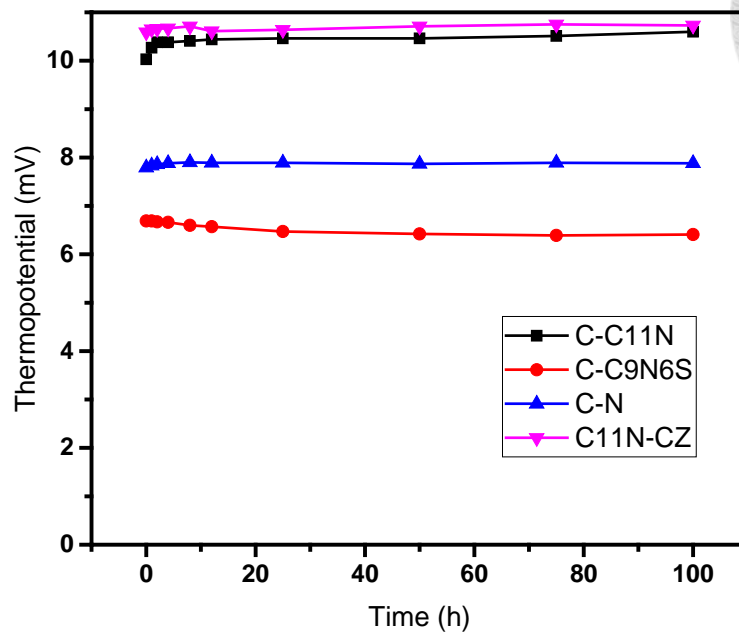


Fig. 4.11 Time dependence test of thermo-potential of C-C11N, C -C9N6S, C-N and C11N-CZ thermocouples at 400 °C in air.

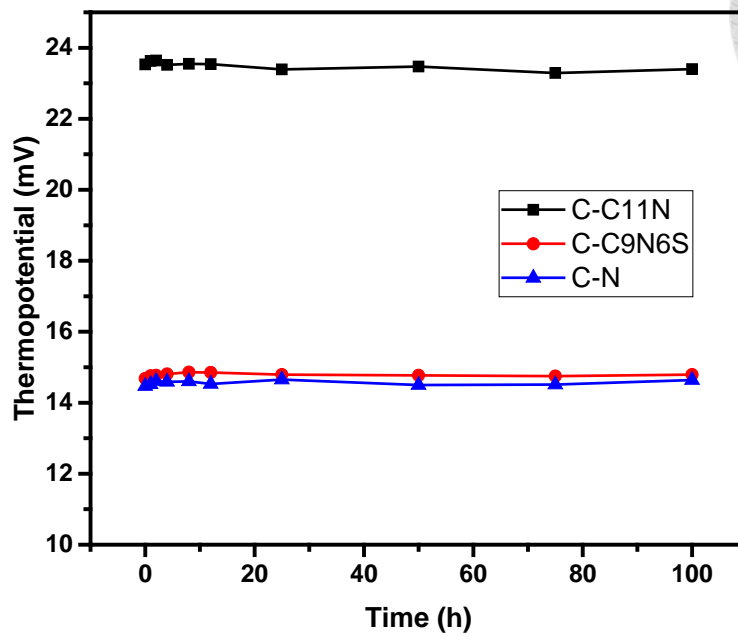


Fig. 4.12 Time dependence test of thermo-potential of C-C11N,C-C9N6S and C-N thermocouples at 650 °C in air.

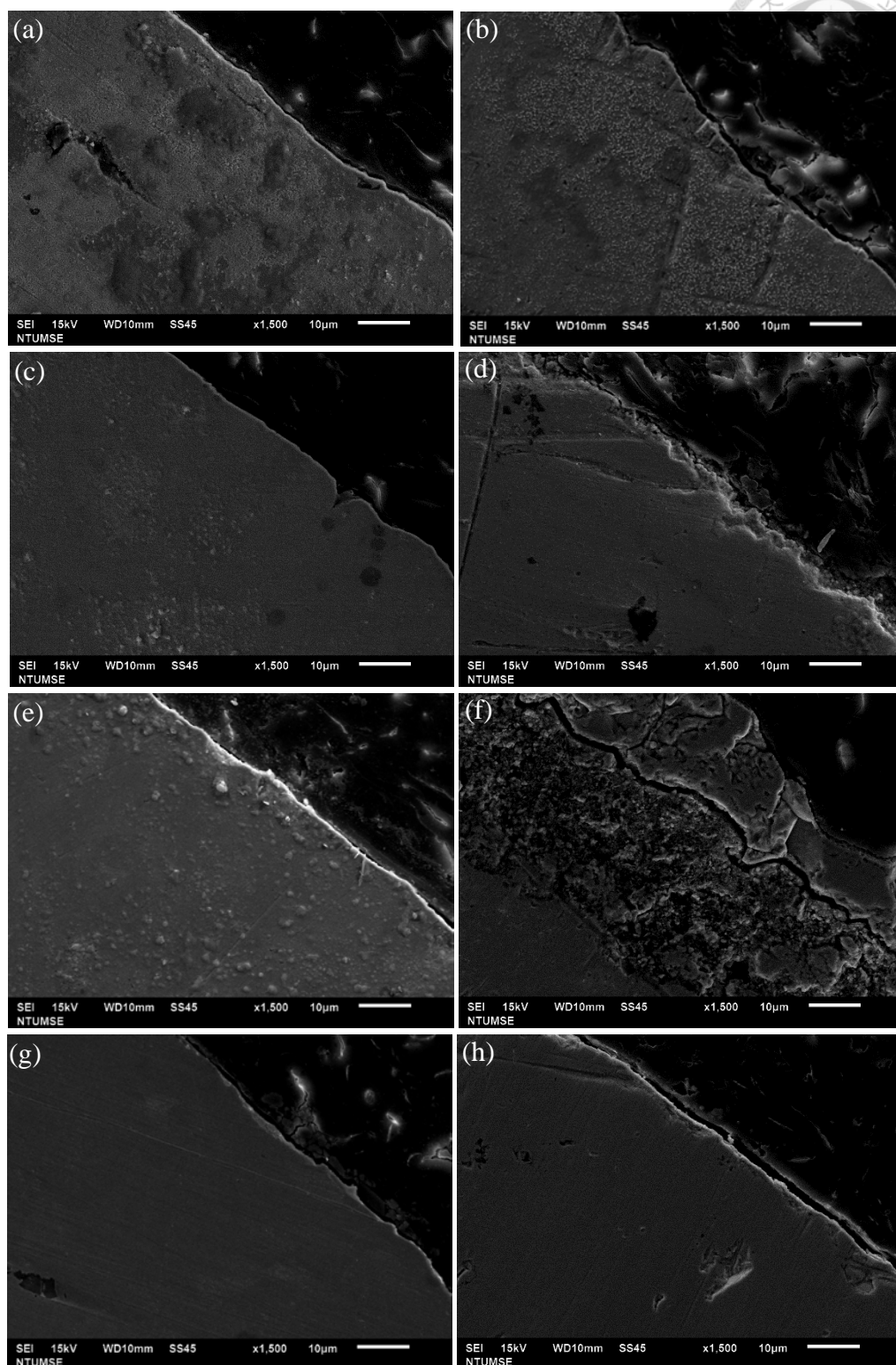


Fig. 4.13 Microstructure of four wires (a) and (b) C, (c) and (d) C11N, (e) and (f)

C9N6S, (g) and (h) N before and after heat-treated at 650 °C for 100 h in air.



## 4.2 Properties of Anode

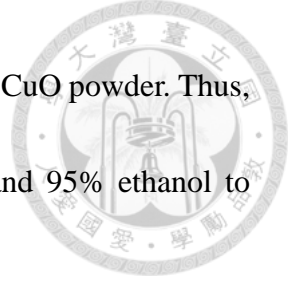
Five different powders, CuO, NiO, 8YSZ-D, 8YSZ-T and MCMB (used as pore-former) were mixed to make anode powders. Table 4.2 Properties of raw powders shows the basic properties of those five powders. In order to get optimal Cu-Ni based anode, dispersion, sintering, catalytic and conductivity properties are tested in this study.

### 4.2.1 Dispersion Properties

Powders should be well-dispersed to increase the triple phase boundary of anode. In Chen's [43] report, NiO, 8YSZ and MCMB had been tested in three solutions for 200 h. Three powders all performed good dispersive properties in 95% ethanol, which was shown in Fig. 4.14. However, in two water-based solutions,  $H_f/H_0$  of NiO and 8YSZ decreased about 20% and 5%, respectively. MCMB had worst dispersive property in water-based solution, floating on the top of solution (Table 4.3).

Then we measured the sedimentation properties of CuO powder in four different solutions and dispersants. The slurries were ball-milled for 24 h before poured into volumetric cylinder to have sedimentation test. Best dispersive condition was determined by a higher value of  $H_f/H_0$ . Fig. 4.15 shows that DI water with both 1 wt% D-134 and 1 wt% Darven C dispersant are good dispersing media for CuO powder. In contrast, ethanol





and ethanol with 1wt% PVB are not as good as the aqueous cases for CuO powder. Thus, we choose DI water with 1wt% D-134 to disperse CuO powder and 95% ethanol to disperse NiO, 8YSZ for homogeneous mixing.

#### 4.2.2 Porosity of Anode

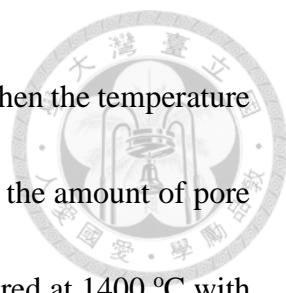
In previous reports [49, 50], the best porosity range of anode should be 30 vol% to 40 vol% so the gaseous molecules of fuel can diffuse to reaction interface. In order to obtain optimum anode formula, different weight percents of MCMB were added to increase open pores. The Archimedes' method was adopted to measure the density and porosity of the anode. The theoretical densities of N<sub>100</sub>Z, C<sub>50</sub>N<sub>50</sub>Z and C<sub>100</sub>Z can be calculated as following equations.

$$D_{N_{100}Z} = \frac{100 \text{ g}}{\frac{50 \text{ g}}{6.67 \text{ g/cm}^3} + \frac{50 \text{ g}}{5.9 \text{ g/cm}^3}} = 6.26 \text{ g/cm}^3 \dots\dots\dots(4.3),$$

$$D_{C_{50}N_{50}Z} = \frac{100 \text{ g}}{\frac{25 \text{ g}}{6.31 \text{ g/cm}^3} + \frac{25 \text{ g}}{6.67 \text{ g/cm}^3} + \frac{50 \text{ g}}{5.9 \text{ g/cm}^3}} = 6.18 \text{ g/cm}^3 \dots\dots\dots(4.4),$$

$$D_{C_{100}Z} = \frac{100 \text{ g}}{\frac{50 \text{ g}}{6.31 \text{ g/cm}^3} + \frac{50 \text{ g}}{5.9 \text{ g/cm}^3}} = 6.10 \text{ g/cm}^3 \dots\dots\dots(4.5).$$

The porosities of three anodes sintered at different temperatures with 20 wt% poreformers are shown in Fig. 4.16. The porosity of N<sub>100</sub>Z sintered at 1500 °C for 1 h is 31%, which meets the requirement. While the porosity of C<sub>50</sub>N<sub>50</sub>Z sintered at 1100 °C to 1400 °C is about 55%, due to a low melting point of CuO. In order to reduced the porosity of C<sub>50</sub>N<sub>50</sub>Z, various percentages of MCMB were added. Fig. 4.17 shows the porosity of C<sub>50</sub>N<sub>50</sub>Z with



different amount of MCMB sintered at 1300 °C or 1400 °C for 1 h. When the temperature is higher than 1300 °C, the porosity of C<sub>50</sub>N<sub>50</sub>Z is greatly affected by the amount of pore former, but not sintering temperature. The porosity of C<sub>50</sub>N<sub>50</sub>Z sintered at 1400 °C with 10 wt% MCMB is 38.7%, and without MCMB is 25.4%. In order to compare the samples in similar porosity, N<sub>100</sub>Z, C<sub>50</sub>N<sub>50</sub>Z and C<sub>100</sub>Z were sintered at 1400 °C, 1200 °C and 1000 °C for 1 h respectively, and observed in catalytic test.

#### 4.2.3 TGA Analysis of Anode Materials

First, two powders (NiO and CuO) and three different types of anode (C<sub>100</sub>Z, C<sub>50</sub>N<sub>50</sub>Z and N<sub>100</sub>Z) were analyzed by TGA in two reducing atmospheres (N<sub>2</sub>-20% H<sub>2</sub> and N<sub>2</sub> -20% CH<sub>4</sub>) which are common fuels used in SOFC. Fig. 4.18 shows that NiO begins to lose its mass from 300 °C to 385 °C. While the mass of CuO decreases from 200 °C to 275 °C. Mass loss of NiO and CuO are about 22.6% and 20.1%. The theoretical mass loss of NiO and CuO are 21.4% and 20.1%. The slight difference between theoretical and actual measured value may be due to water vapor evaporation.

When NiO was heated in CH<sub>4</sub>, it started to lose weight at 480 °C and slightly gain weight at 550 °C. The increasing weight may be caused by carbon deposition. There are two steps reduction reaction of CuO in CH<sub>4</sub>. First, 10% weight loss is from 350 °C to 465 °C and the other is 8% weight loss from 465 °C to 600 °C. This situation may result from

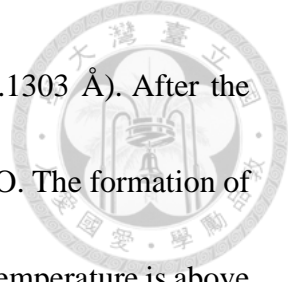
two kinds of reducing products:  $\text{Cu}_2\text{O}$  and  $\text{Cu}$ . In this Fig. 4.18, we could know that  $\text{CuO}$  showed a higher chemical reactivity in both hydrogen and methane.



Fig. 4.19 and Fig. 4.20 show TGA analysis of three types of anode, a mixture of  $\text{CuO}$  or  $\text{NiO}$  with 8YSZ, which have been calcined at  $1000\text{ }^{\circ}\text{C}$ .  $\text{C}_{100}\text{Z}$  and  $\text{C}_{50}\text{N}_{50}\text{Z}$  started to reduce at  $200\text{ }^{\circ}\text{C}$  and  $190\text{ }^{\circ}\text{C}$  in  $20\%\text{H}_2\text{-N}_2$ . Both of them complete the reduction at  $300\text{ }^{\circ}\text{C}$ . The range of reducing temperature is similar to that of  $\text{CuO}$  powder in  $\text{H}_2$ . While  $\text{N}_2$  reduced from  $350\text{ }^{\circ}\text{C}$  to  $700\text{ }^{\circ}\text{C}$  in  $\text{H}_2$ . Additive of 8YSZ may lower the speed of  $\text{NiO}$  reduction, but it didn't affect the reduction speed of  $\text{CuO}$ . In methane atmosphere (Fig. 4.20), all of three anodes begin to reducing their mass at  $480\text{ }^{\circ}\text{C}$ . However,  $\text{C}_{50}\text{N}_{50}\text{Z}$  and  $\text{N}_{100}\text{Z}$  reversely gain weight at  $545\text{ }^{\circ}\text{C}$  and  $590\text{ }^{\circ}\text{C}$ , implying carbon deposition being initiated. Owing to a low capability of C-C formation by  $\text{Cu}$ ,  $\text{C}_{100}\text{Z}$  doesn't have carbon deposition up to  $700\text{ }^{\circ}\text{C}$ .

#### 4.2.4 Catalytic Effects of Methane

Before reacting with methane,  $\text{NiO}$  on anode should be reduced into metallic phase. In order to assure full reduction of the anode samples, the crystal phases of sintering disks were analyzed by XRD method. Fig. 4.21 is the XRD patterns of  $\text{C}_{100}\text{Z}$  disk sintering at  $1000\text{ }^{\circ}\text{C}$  and after reduced at  $700\text{ }^{\circ}\text{C}$  for 10 h. Before the reduction, there are three phases in  $\text{C}_{100}\text{Z}$ , cubic-phase YSZ ( $a=5.139\text{ }\text{\AA}$ ), monoclinic  $\text{ZrO}_2$  ( $a=5.3129\text{ }\text{\AA}$ ,  $b=5.2125\text{ }\text{\AA}$ ,  $c=$



5.1471 Å), and monoclinic CuO (a= 4.6853 Å, b= 3.4257 Å, c= 5.1303 Å). After the reduction, the peak of cubic Cu (a= 3.6150 Å) is found instead of CuO. The formation of ZrO<sub>2</sub> monoclinic phase is resulted by the alloying of CuO. When the temperature is above 900 °C, oxygen ions transfer from CuO lattice to oxygen vacancies of YSZ at the interface [51]. Then Y<sup>3+</sup> ions move away from the YSZ lattice for the electrical neutrality. As a result, a non-conducting monoclinic-phase ZrO<sub>2</sub> forms in C<sub>100</sub>Z.

The porosity of C<sub>100</sub>Z and C<sub>100</sub>Z-R which sintered at 1000 °C is around 55% to 65%, as shown in Fig. 4.22 (a) and (b). In Fig. 4.22 (a), the small sphere particles are 8YSZ and the bigger particles are CuO. After reduction, the reduced Cu becomes smaller in size. The reason of increasing porosity after reduction can be explained by the change of their density. The volume shrinkage of CuO and NiO is shown as below.

$$V_{\text{CuO}} = \frac{4.6853 \text{ Å} \times 3.4257 \text{ Å} \times 5.1303 \text{ Å} \times \sin(\pi - 99.549^\circ) - 3.6150 \text{ Å}^3}{4.6853 \text{ Å} \times 3.4257 \text{ Å} \times 5.1303 \text{ Å} \times \sin(\pi - 99.549^\circ)} = 0.418 \dots \dots \dots (4.6),$$

$$V_{\text{NiO}} = \frac{4.1771 \text{ Å}^3 - 3.5238 \text{ Å}^3}{4.1771 \text{ Å}^3} = 0.400 \dots \dots \dots (4.7),$$

where 99.549° is the β angle of monoclinic CuO.

Fig. 4.23 and Fig. 4.24 show the XRD curves of C<sub>50</sub>N<sub>50</sub>Z and N<sub>100</sub>Z samples which have been sintered at 1200 °C and 1400 °C for 1 h, respectively. In addition to peaks of CuO, YSZ and m-ZrO<sub>2</sub>, C<sub>50</sub>N<sub>50</sub>Z has additional phase, a cubic structure of NiO (a=4.1771 Å). After the reduction at 700 °C for 10 h, the peaks of ZrO<sub>2</sub>, NiO and CuO were disappeared. This implies that the Cu and Ni in C<sub>50</sub>N<sub>50</sub>Z-R is reduced to metallic phase.

C<sub>50</sub>N<sub>50</sub>Z-R also shows the solid solution of the Cu and Ni metals, matching to Cu-Ni phase diagram [47].



The macrostructure of C<sub>50</sub>N<sub>50</sub>Z sintered at 1200 °C is shown in Fig. 4.25 (a). The grain size of C<sub>50</sub>N<sub>50</sub>Z is about 3 μm and the porosity is 51.9%. After reduced at 700 °C for 10 h, the porosity obviously increases to 58.1% by reduction of NiO and CuO. Some of small particles precipitate on the big grains, as shown in Fig. 4.25 (b). The small particles are Cu grains approved by EDS analysis.

Fig. 4.24 is the XRD patterns of N<sub>100</sub>Z disk sintering at 1400 °C. In the same reducing condition, the XRD pattern of C<sub>100</sub>Z-R shows a fully reduction of NiO into cubic Ni ( $a=3.5238 \text{ \AA}$ ). The porosity of N<sub>100</sub>Z is 45.3 % and 52.6% before and after reducing. The surface of N<sub>100</sub>Z sintered at 1400 °C is in Fig. 4.26 (a) and (b). The grain size is smaller than that of C<sub>50</sub>N<sub>50</sub>Z sintered at 1200 °C. Thus, by adding CuO into Ni-based anode may improve the sintering behavior and increase the grain growth.

Following, three anode samples using methane were tested to observe the conversion behavior of methane through the anode and permeability change at 650 °C. Methane decomposition is following a main reforming reaction ( $\text{CH}_4 \rightarrow \text{C} + 2\text{H}_2$ ) which starts nearly at 700 °C without catalyst [52].

A flow rate of 10 ml·min<sup>-1</sup> methane flows through the anode samples was conducted during the heating process from room temperatures to 650 °C and lasting for 2 h. Then

reformed gas was collected at 300 °C and 650 °C in every 30 min. Fig. 4.27 shows the content of H<sub>2</sub> appearing in the gas product. The conversion temperature of CH<sub>4</sub> by Ni metal can be improved to 650 °C, which is the operating temperature of IT- SOFC. The degree of the conversion of CH<sub>4</sub> from high to low is N<sub>100</sub>Z, C<sub>50</sub>N<sub>50</sub>Z and C<sub>100</sub>Z. There is almost none of H<sub>2</sub> conversion when the methane flows through the C<sub>100</sub>Z.

The content of H<sub>2</sub> produced in reforming of CH<sub>4</sub> through N<sub>100</sub>Z is up to 35.1% when temperature reach 650 °C, and H<sub>2</sub> reduces as the time went by. It might be caused by coke formation on the anode. While the initial H<sub>2</sub> content of C<sub>50</sub>N<sub>50</sub>Z is 11.3% at the beginning, but it increases to 33.06% after 90 min and slight decreases to 30.16% as the time increases to 120 min. As a result, N<sub>100</sub>Z has a highest ability to converse methane into H<sub>2</sub>. However, the conversion rate cannot last for long in N<sub>100</sub>Z due to coking. In contrast, C<sub>50</sub>N<sub>50</sub>Z has a stable conversion rate in this 2 h thermal process. Therefore, we may be selected C<sub>50</sub>N<sub>50</sub>Z mixture as our anode material.

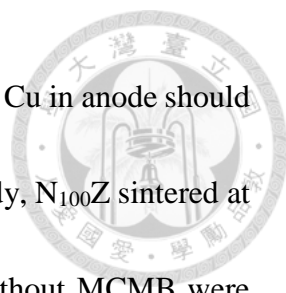
In order to know the degree of carbon deposition, permeability of the anode was tested using nitrogen as a medium. The viscosity of nitrogen is 17.643 μPa·s and the density is 1.251 kg/m<sup>3</sup> [52]. In this study, Forchheimer number  $F_0$  is in the criterion for non-Darcy flow. Thus, we use Forchheimer equation, Eq. (2.9) to fit the data shown in Fig. 4.28 (a) and (b). The figure shows the pressure drop across N<sub>100</sub>Z sample plotted against the velocity of nitrogen. The value is higher as velocity increased and shows

parabolic relationship. We can get the permeability of N<sub>100</sub>Z before and after reacting with CH<sub>4</sub> are  $11.95 \times 10^{-13}$  and  $2.08 \times 10^{-13}$ , which are shown in Table 4.4. It is 5.75 times less after reacting with methane for 2 h.

Compare to N<sub>100</sub>Z, the permeability of C<sub>50</sub>N<sub>50</sub>Z before and after reacting with CH<sub>4</sub> are  $155.93 \times 10^{-13}$  and  $7.37 \times 10^{-13}$ . It is 21.16 times less after reacting with methane for 2 h. This result implies that two samples have carbon deposition in this study. However, the permeability of C<sub>50</sub>N<sub>50</sub>Z after reforming CH<sub>4</sub> is much higher than that of N<sub>100</sub>Z. This may be the reason why the H<sub>2</sub> content passing C<sub>50</sub>N<sub>50</sub>Z is stable for 2 h in the GC analysis. Apart from this, we also investigate the carbon deposition from a kinetic point of view. Fig. 4.29 shows the pressure front of the sample plotted against the reaction time during the 2 h thermal process. The speed of increasing pressure can imply the rate of carbon deposition. The pressure (P) of C<sub>50</sub>N<sub>50</sub>Z gradually increases in 2 h. In contrast, the pressure of N<sub>100</sub>Z increases faster than that of previous C<sub>50</sub>N<sub>50</sub>Z in the first h and reaches a balance in 1.5 h. There may be no contact area between anode and CH<sub>4</sub> after 1.5 h. The carbon deposition rate of N<sub>100</sub>Z is much faster than that of C<sub>50</sub>N<sub>50</sub>Z. Thus, the C<sub>50</sub>N<sub>50</sub>Z is a candidate anode material to use in hydrocarbon fuels.

#### 4.2.5 Electrical Conductivity of Anode

Conductivity is an important criterion for an anode of SOFC. In order to have good



conductivity at operating temperature of SOFC, the content of Ni and Cu in anode should be more than 40 vol% and 20 vol%, respectively [53, 54]. In this study, N<sub>100</sub>Z sintered at 1500 °C with 20 wt% MCMB and C<sub>50</sub>N<sub>50</sub>Z sintered at 1300 °C without MCMB were tested by a four-probe method. Fig. 4.30 shows the electrical conductivity of N<sub>100</sub>Z (31% porosity) is 482.75 Scm<sup>-1</sup> at 650 °C and 363.52 Scm<sup>-1</sup> at 800 °C. The activation energy of N<sub>100</sub>Z is -2.06 kJmol<sup>-1</sup>. While C<sub>50</sub>N<sub>50</sub>Z has a higher electrical conductivity because of its lower porosity. The electrical conductivity is 1503.37 Scm<sup>-1</sup> at 650 °C and 959.60 Scm<sup>-1</sup> at 800 °C. However, the activation energy of C<sub>50</sub>N<sub>50</sub>Z is -6.46 kJmol<sup>-1</sup>, higher than N<sub>100</sub>Z. They are both valid to use as anode materials. Therefore, we tried to use C<sub>50</sub>N<sub>50</sub>Z and N<sub>100</sub>Z for making single cell in the following section.





Table 4.2 Properties of raw powders for anode

	CuO	NiO	8YSZ-T	8YSZ-D	MCMB
Density (g/cm <sup>3</sup> )	6.31	6.67	5.9	5.9	2.18
Atomic weight	79.55	74.69	131.42	131.42	12
D <sub>50</sub> (μm)	3.037	1.0 ±0.5	230 nm	0.279	21±3
BET (m <sup>2</sup> /g)	13.2	77.6	7±2	7-10	<1.2



Table 4.3 Dispersion results ( $H_f/H_0$ ) of NiO, 8YSZ and MCMB [courtesy by Mu-Min,

[43]]

<b>Powders</b>	<b>H<sub>2</sub>O + Darven C</b>	<b>H<sub>2</sub>O + D-134</b>	<b>95% Ethanol</b>	<b>50% Ethanol</b>
<b>NiO</b>	78%	80%	100%	100%
<b>8YSZ</b>	95%	96%	100%	100%
<b>MCMB</b>	Floating	Floating	100%	99%

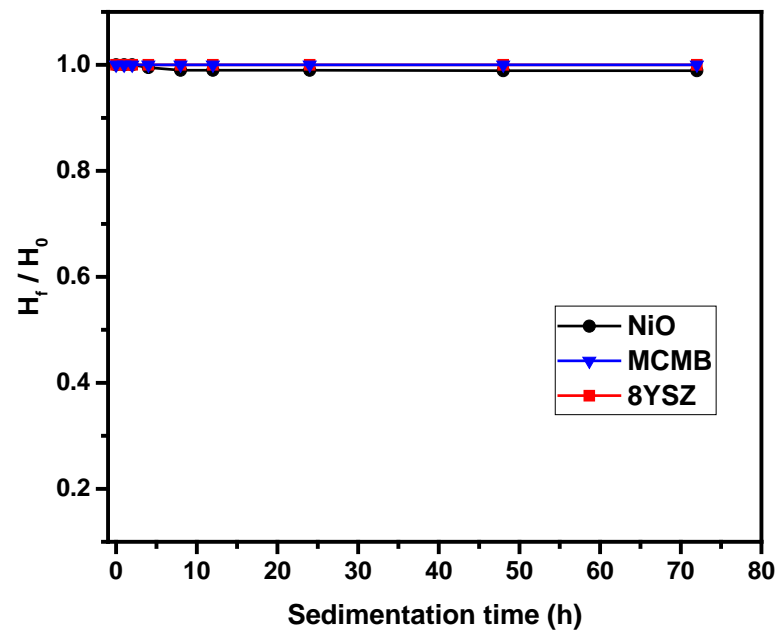


Fig. 4.14 Sedimentation height ratio ( $H_f/H_0$ ) of 8YSZ, NiO and MCMB slurries using 95% ethanol plotted against sedimentation time.

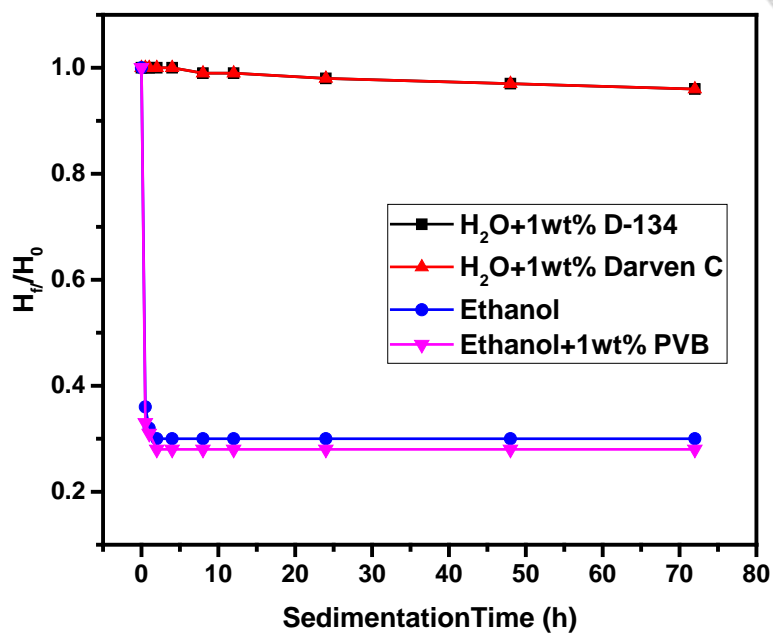


Fig. 4.15 Sedimentation height ratio ( $H_f/H_0$ ) of CuO slurries in four solvents plotted against sedimentation time..

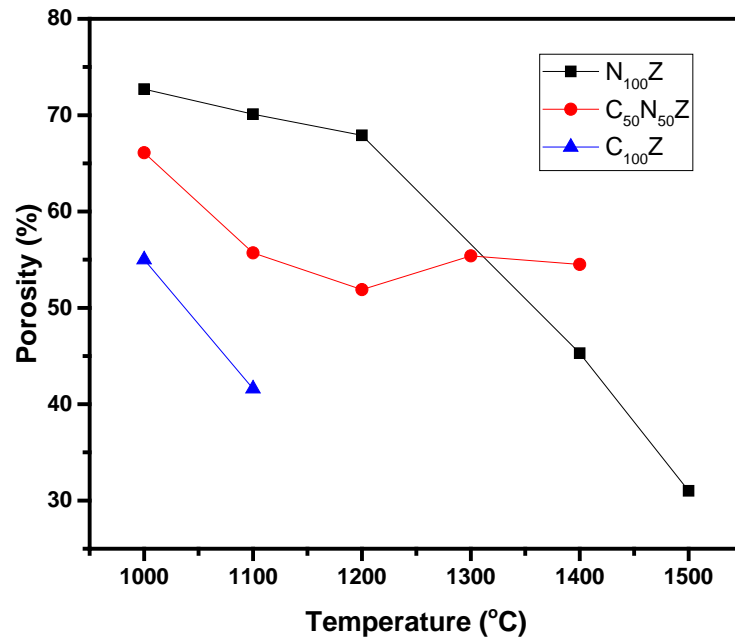


Fig. 4.16 Porosities of N<sub>100</sub>Z, C<sub>50</sub>N<sub>50</sub>Z and C<sub>100</sub>Z samples with 20 wt% pore former (MCMB) sintered at different temperatures.

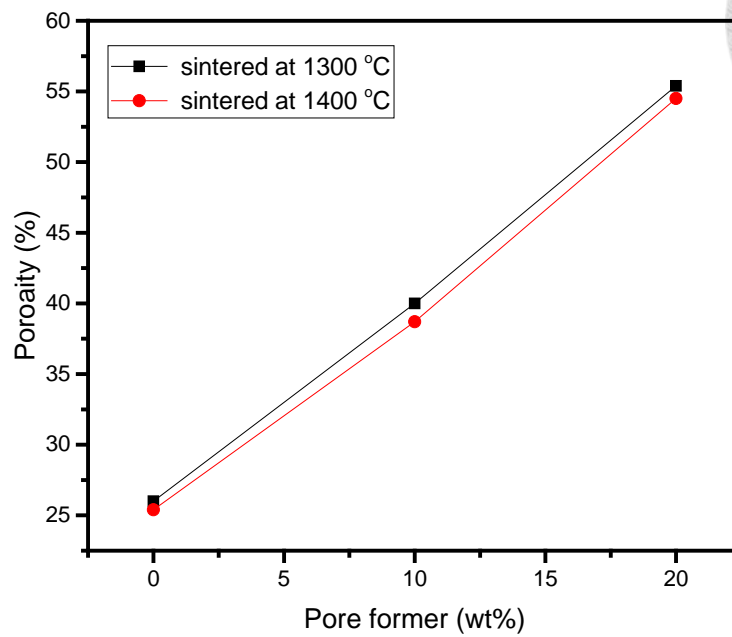


Fig. 4.17 Porosities of  $C_{50}N_{50}Z$  samples sintered at selected temperature versus different amounts of pore former in anode formulation.

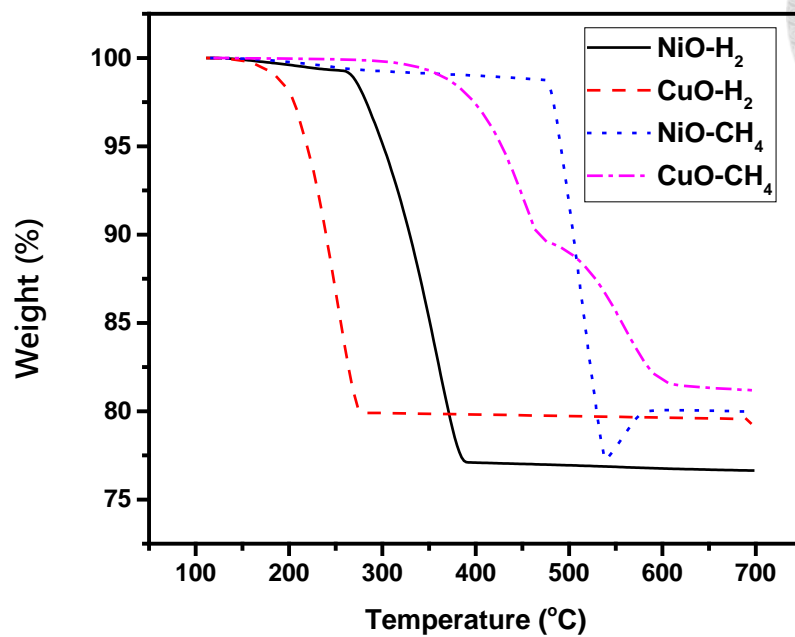


Fig. 4.18 TGA test results of CuO or NiO powder in specified reducing atmosphere, either N<sub>2</sub>-20% H<sub>2</sub> or N<sub>2</sub>-20% CH<sub>4</sub>.

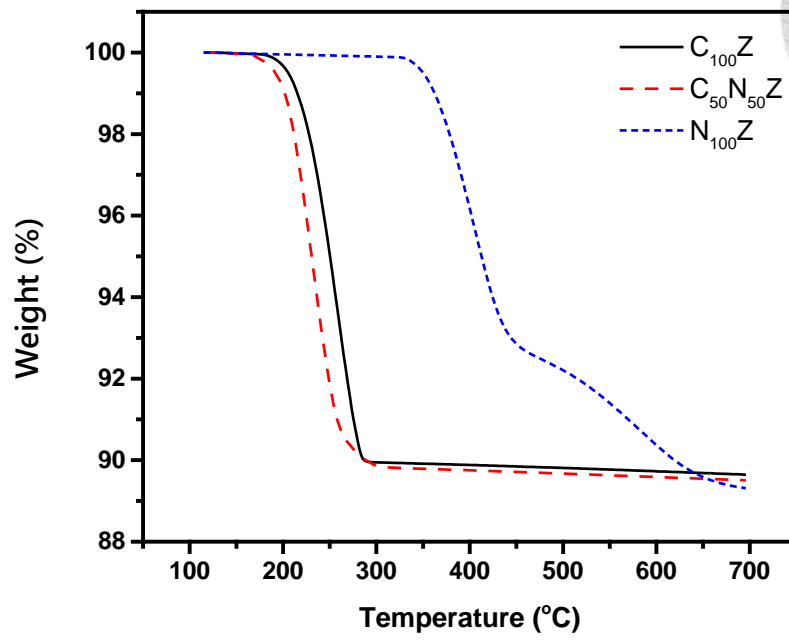


Fig. 4.19 TGA test of C<sub>100</sub>Z, C<sub>50</sub>N<sub>50</sub>Z and N<sub>100</sub>Z disks reduced in N<sub>2</sub>-20% H<sub>2</sub>.



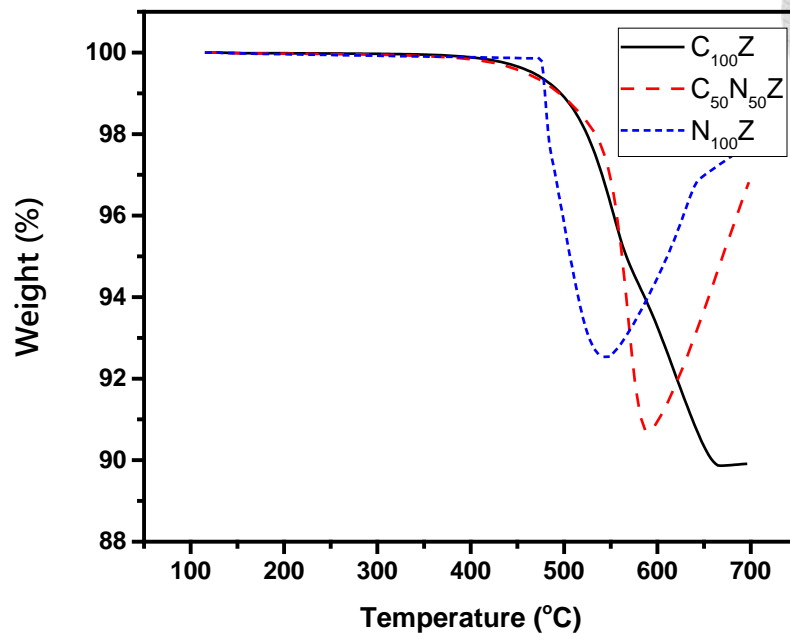


Fig. 4.20 TGA test of C<sub>100</sub>Z, C<sub>50</sub>N<sub>50</sub>Z and N<sub>100</sub>Z disks reduced in N<sub>2</sub>-20% CH<sub>4</sub>.

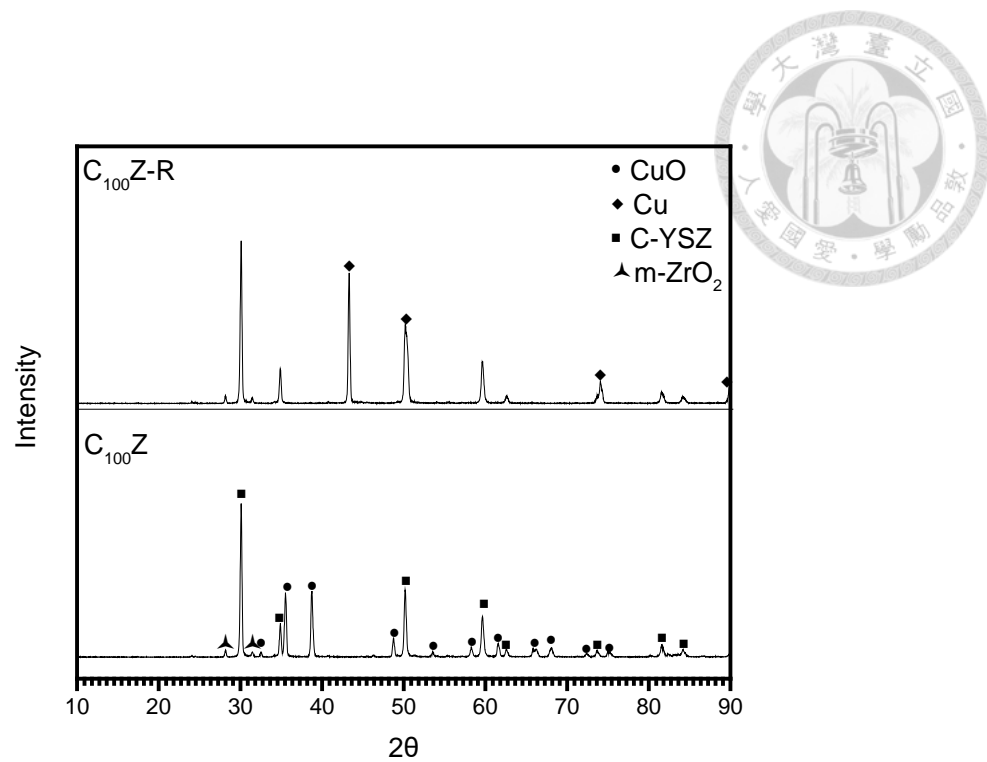


Fig. 4.21 Crystal phase identification of  $C_{100}Z$  anode before and after reduction.

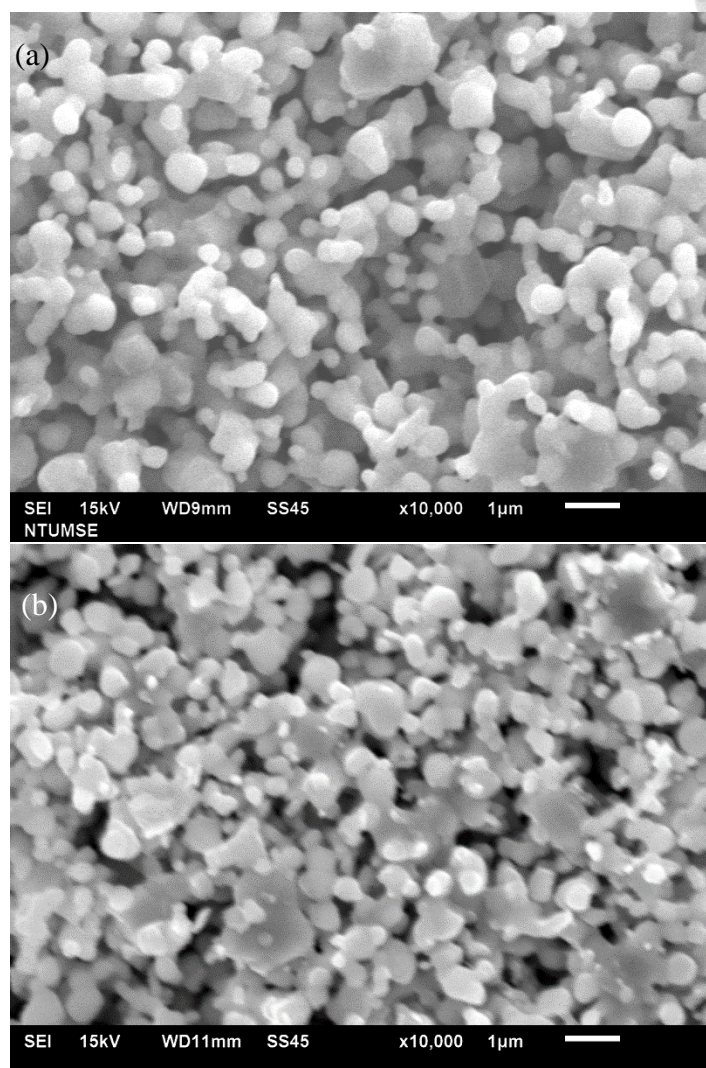


Fig. 4.22 SEM micrographs of top view of anode disks, (a)  $C_{100}Z$  sintered at 1000 °C, (b) after reduced at 700 °C for 10 h.

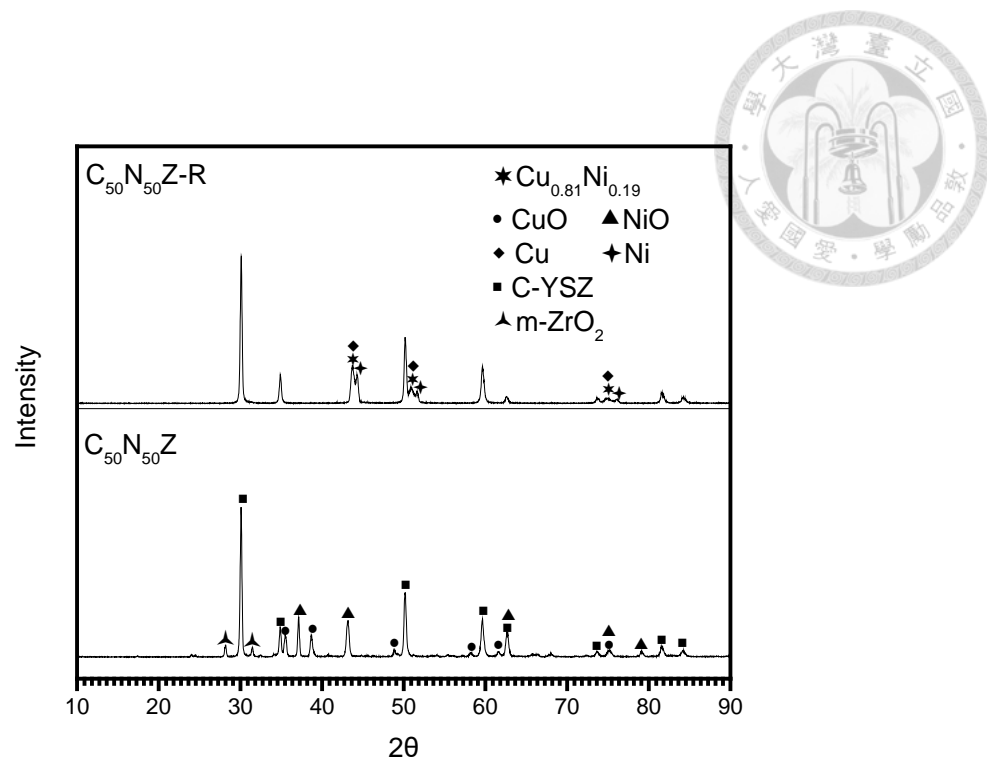


Fig. 4.23 Crystal phase identification of  $C_{50}N_{50}Z$  anode before and after the reduction.

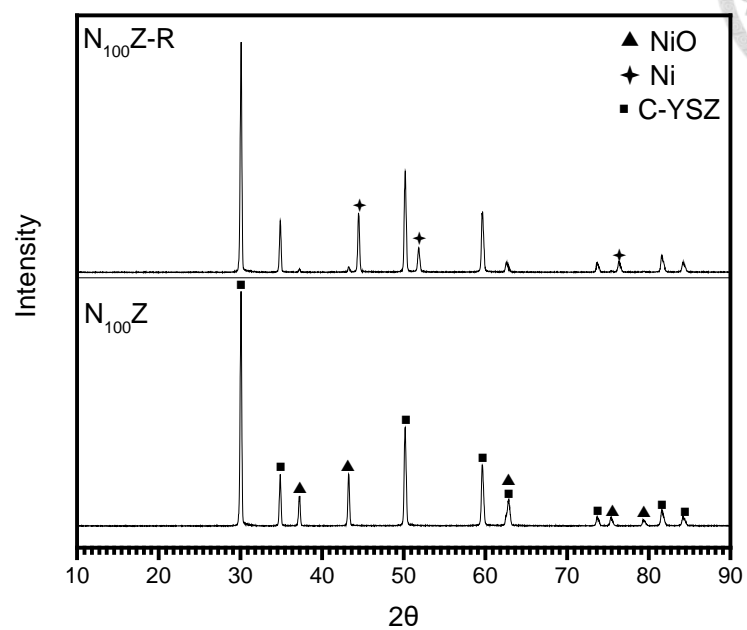


Fig. 4.24 Crystal phase identification of  $N_{100}Z$  anode before and after the reduction.

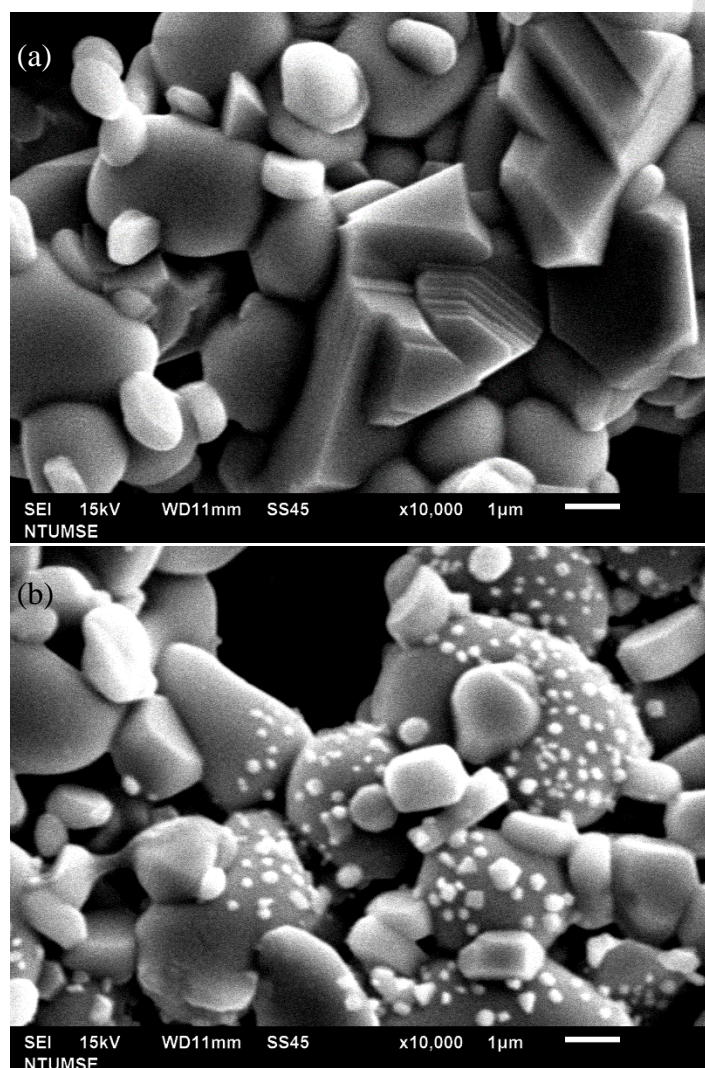


Fig. 4.25 SEM micrographs of top view of C<sub>50</sub>N<sub>50</sub>Z anode disks, (a) sintered at 1200 °C, (b) after reduced at 700 °C for 10 h.



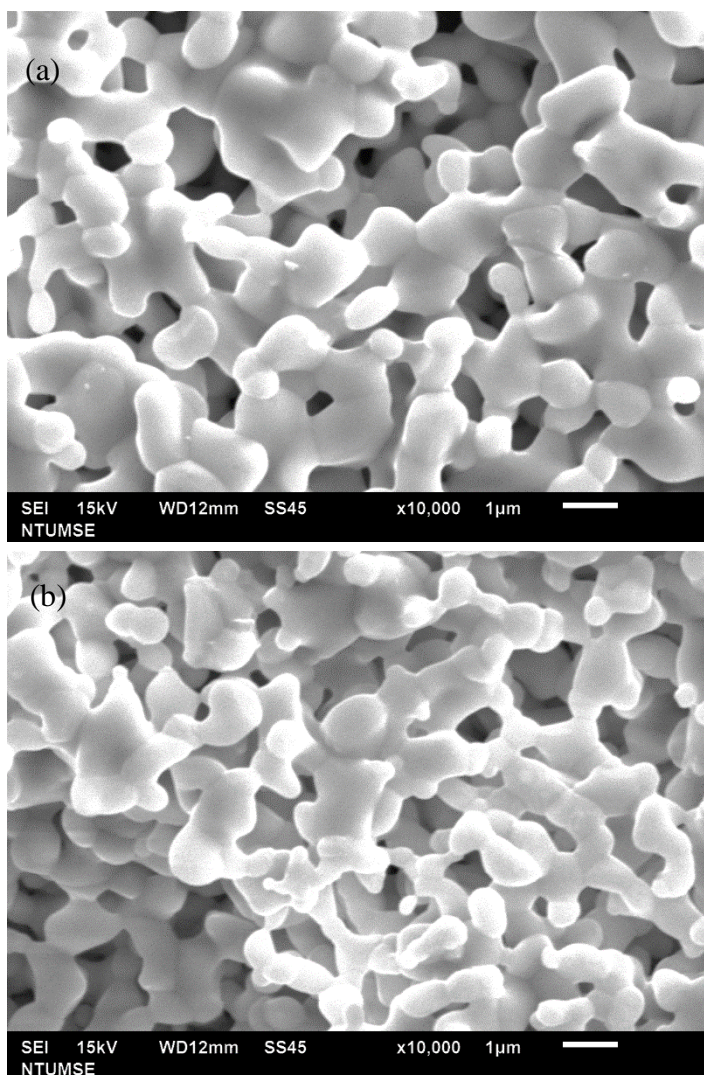


Fig. 4.26 SEM micrographs of top view of N<sub>100</sub>Z anode disks, (a) sintered at 1400 °C, (b) after reduced at 700 °C for 10 h.

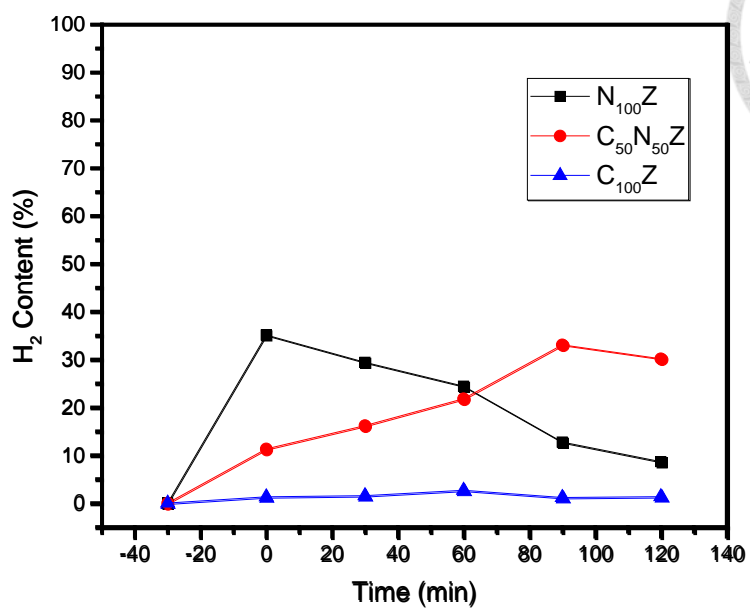


Fig. 4.27 Content of  $H_2$  in reacting gas ( $CH_4$ ) through three anodes  $C_{100}Z$ ,  $C_{50}N_{50}Z$  and  $N_{100}Z$  at  $650^\circ C$  in 2 h.



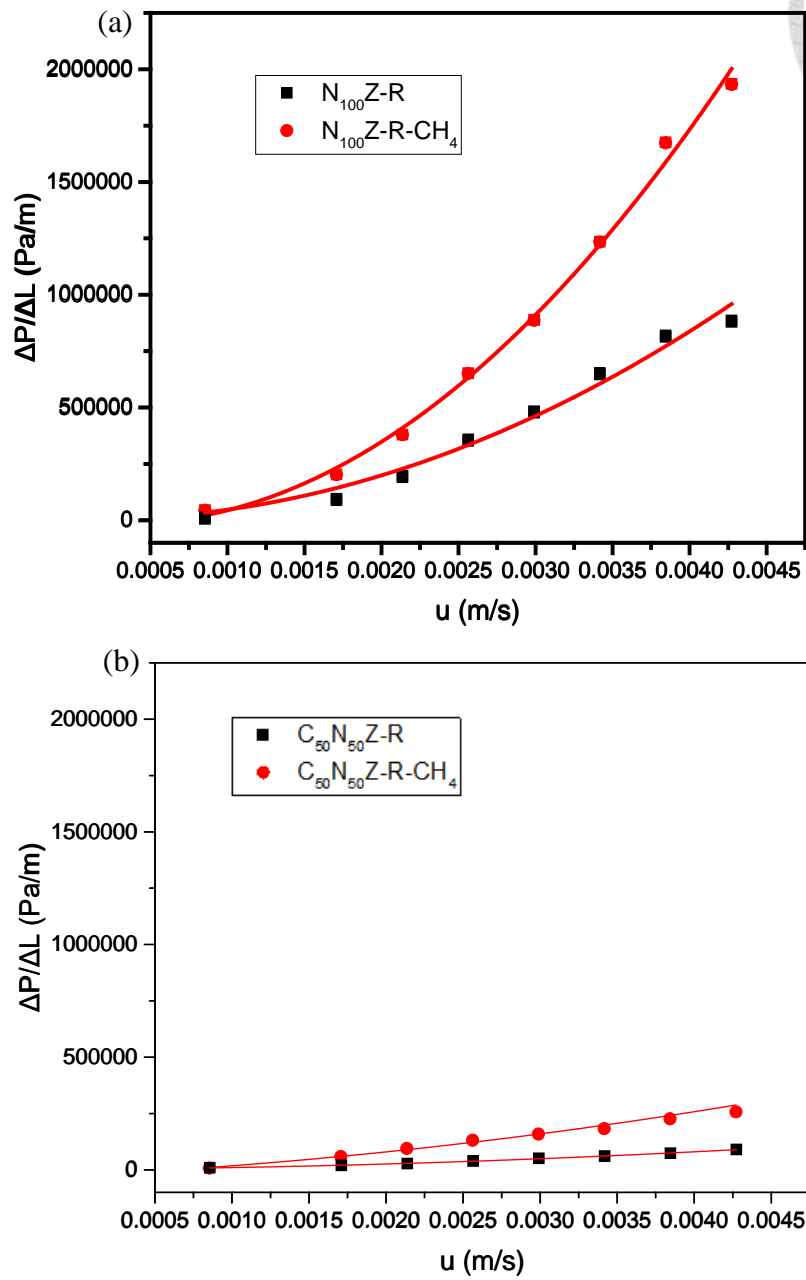


Fig. 4.28 Pressure drop across  $N_{100}Z$  and  $C_{50}N_{50}Z$  sample plot against velocity of  $N_2$  before and after reacting with  $CH_4$  at  $650^\circ C$  in 2 h



Table 4.4 Permeability of two anodes before and after carbon deposition

Sample	$\beta\rho(10^9)$	$\frac{\mu}{k}(10^6)$	$k(10^{-13})$
N <sub>100</sub> Z-R-CH <sub>4</sub>	129.558	84.9489	2.08
N <sub>100</sub> Z-R	55.735	14.7585	12.0
C <sub>50</sub> N <sub>50</sub> Z-R-CH <sub>4</sub>	23.3021	23.9477	7.37
C <sub>50</sub> N <sub>50</sub> Z-R	8.62875	1.13144	156

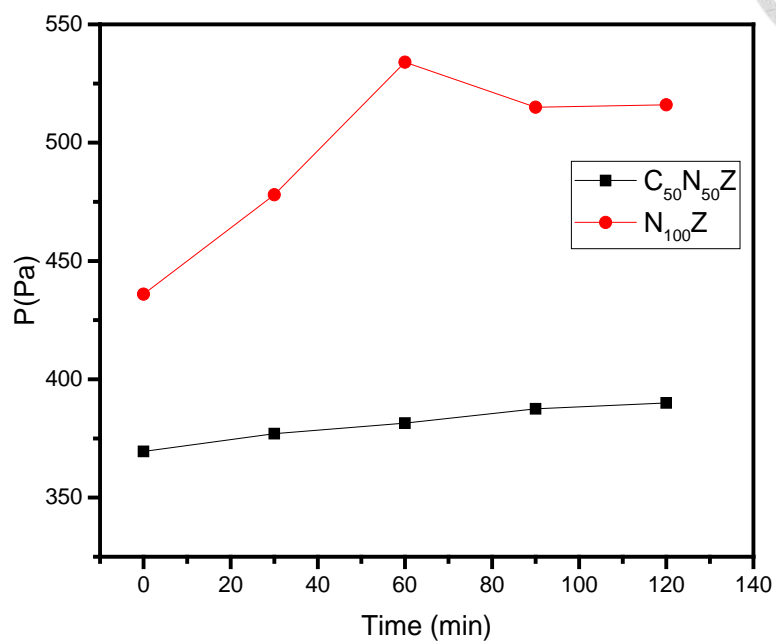


Fig. 4.29 Pressure head of the reactor plotted against deposition time showing the kinetics of coking reaction of  $C_{50}N_{50}Z$  and  $N_{100}Z$  in  $CH_4$  at 650 °C.

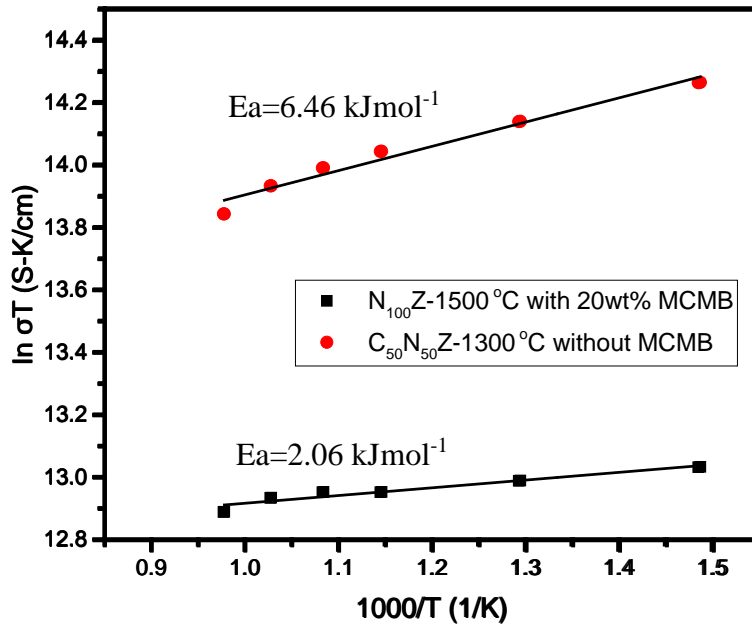


Fig. 4.30 Arrhenius plot of electric conductivity of  $N_{100}Z$  sintered at  $1500^\circ C$  with 20 wt% MCMB and  $C_{50}N_{50}Z$  sintered at  $1300^\circ C$  without MCMB.



## 4.3 Fabrication and Characterization of Half-Cell

### 4.3.1 N<sub>100</sub>Z Anode Supported Cells

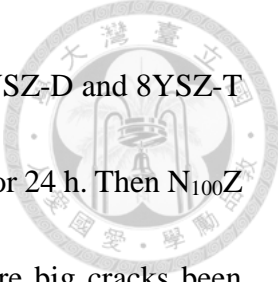
Thin electrolyte layer was made by using spin-coating method in this study. Since a strength > 3MPa of porous anode disks is needed, N<sub>100</sub>Z are pre-sintered at 1000 °C and the porous microstructure is shown in Fig. 4.31. There are varying sizes of pores caused by a burn-out of MCMB. The average size of the pores measured by smile view software is 12.4 μm and the biggest one is 33.6 μm. The diameter of a N<sub>100</sub>Z anode sintered at 1000 °C is 29.2±0.5 mm and the linear shrinkage is 2.60±1.67%.

According to previous results in our lab [44], the addition of 8YSZ-N layer is valid to flatten the surface and decrease the contact and polarization resistances. After pre-sintered at 1000 °C, the anode substrates of N<sub>100</sub>Z was spin-coated with a layer made of 1 wt% nano-sized 8YSZ-N slurry. The medium particle size (D<sub>50</sub>) of 8YSZ-N is about 60 nm, which can fill in the pores on the anode. Fig. 4.32 (a) and (b) show the surface becomes smoother after co-sintered at 1000 °C. However, some cracks and pores appeared on the surface of the disks at 1400 °C, as shown in Fig. 4.32 (c) and (d). Fig. 4.32 (e) also shows the cross-section of the anode with 1 cycle spin-coated 8YSZ-N. The average thickness is 2.0 ± 0.2 μm. As the sintering temperature increases, the cracks and pores grow bigger. To prevent fuel leakage, more than one layer 8YSZ electrolyte are

needed in this study.



To make dense electrolyte, co-sintering process plays an important role. Since thermal stress will be generated by the mismatch of anode and electrolyte in the sintering shrinkage and lead to cracking of the electrolyte layer. The total shrinkage of anode and electrolyte should match each other. For determining the thermal processing steps of co-sintering, and selecting suitable 8YSZ powders, the shrinkage behavior of N<sub>100</sub>Z pre-sintered at 1000 °C, then coating with 8YSZ-D (powder provided by Dai-ichi) and 8YSZ-T (powder provided by Tosho) are shown in Fig. 4.33. The bulk samples were sintered from room temperature to 1500 °C at a heating rate of 5 °Cmin<sup>-1</sup> in air. The total shrinkage of N<sub>100</sub>Z, 8YSZ-D and 8YSZ-T at 1500 °C are 21.45%, 17.76% and 20.18% in Fig. 4.33 (a), respectively. The average particle size of 8YSZ-T powder is smaller than that of 8YSZ-D. Smaller particle size and narrow size distribution of 8YSZ-T help sintering. So, the shrinkage of 8YSZ-T is greater than 8YSZ-D, and closer to N<sub>100</sub>Z. On the other hand, the linear shrinkage rate also takes into consideration in the heating process. Fig. 4.33 (b) shows that N<sub>100</sub>Z and 8YSZ-T starts to shrinkage at 1000 °C. But the linear shrinkage rate of 8YSZ-T is faster than that of N<sub>100</sub>Z below than 1350 °C and slower after reaching 1350 °C. While the shrinkage of 8YSZ-D begins at 1100 °C because of its particle size/distribution, the linear shrinkage rate of 8YSZ-D is similar as N<sub>100</sub>Z when the temperature is higher than 1350 °C.



Because both of 8YSZ-D and 8YSZ-T have pros and cons. 8YSZ-D and 8YSZ-T were separately made into 5wt% slurry with ethanol and ball-milled for 24 h. Then N<sub>100</sub>Z anode substrate was spin-coated 2 cycles with the slurries. There are big cracks been observed on the surface of 8YSZ-D in Fig. 4.34 (a). Meanwhile, the top view of 8YSZ-T shows no big cracks after sintered at 1400 °C in Fig. 4.34 (b). However, there are still small pores when 8YSZ-T sintered at 1400 °C.

Fig. 4.35 (a), (b) and (c) show 8YSZ-T sintered at 1400 °C, 1450 °C and 1500 °C. When the temperature increased, the pores reduced as sintering theory described. The grains grew obviously at 1500 °C. Fig. 4.35 (d) also shows that 8YSZ-T is dense and the average thickness of electrolyte layer is  $6.7 \pm 1.3 \mu\text{m}$ . Thus, 8YSZ-T was chosen to be the electrolyte material compatible with the anode N<sub>100</sub>Z. The diameter of N<sub>100</sub>Z disk co-sintered at 1500 °C was  $22.2 \pm 0.2 \text{ mm}$ . The shrinkage was  $24.20 \pm 0.51\%$ , and slightly higher than the DIL results because it hold for 1 h at the sintering temperature.

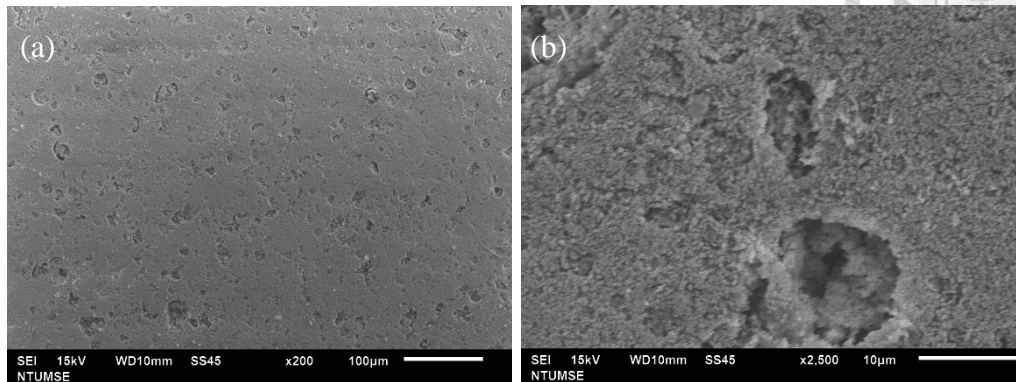


Fig. 4.31 SEM micrographs of surface morphology of N<sub>100</sub>Z anode pre-sintered at 1000

°C (a) 200×, (b) 2500×.



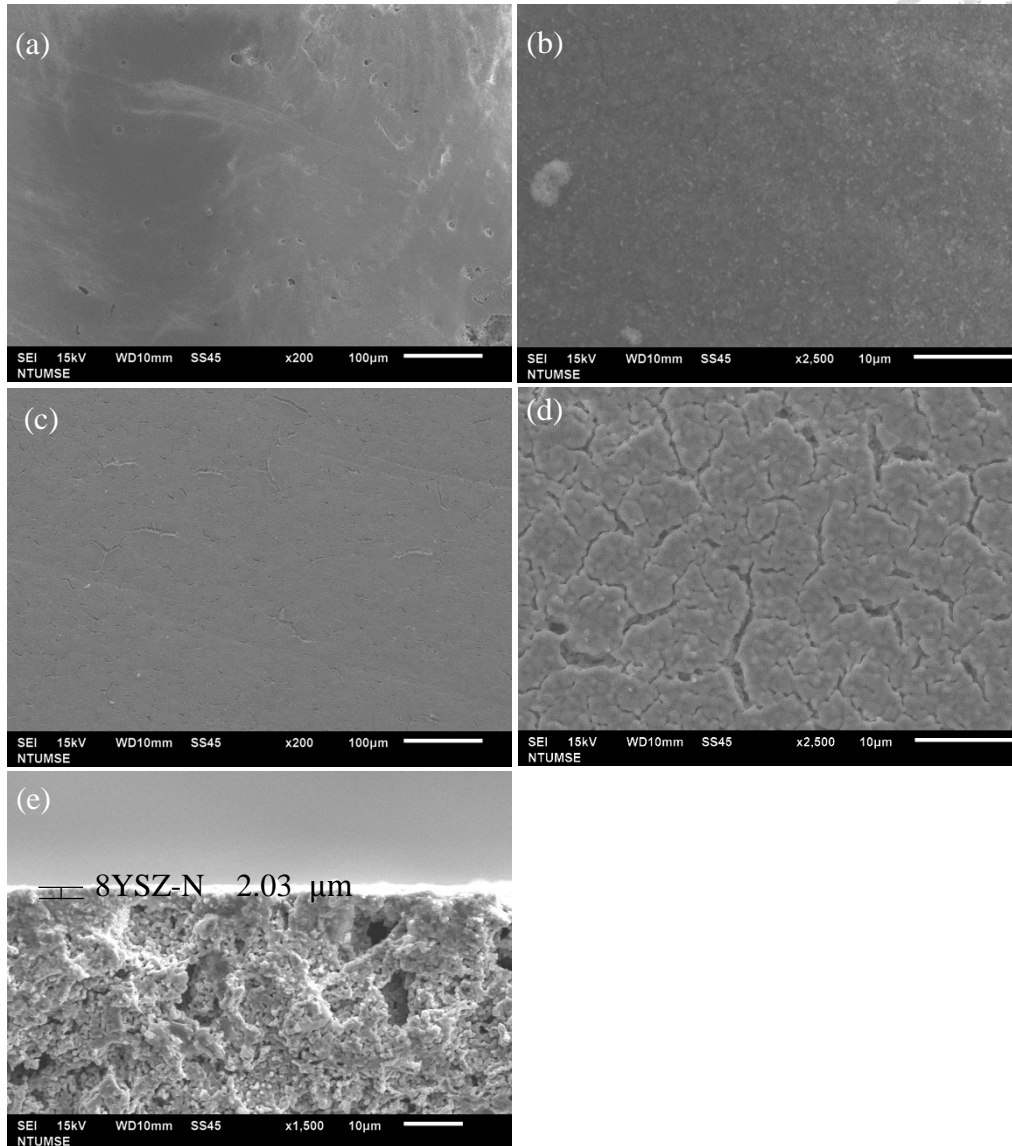


Fig. 4.32 SEM micrographs of the top view of N<sub>100</sub>Z anode with one layer of 8YSZ-N sintered at 1000 °C for 1 h, (a) 200×, (b) 2500×, and sintered at 1400 °C for 1 h (c) 200×, (d) 2500×, and (e) cross-section

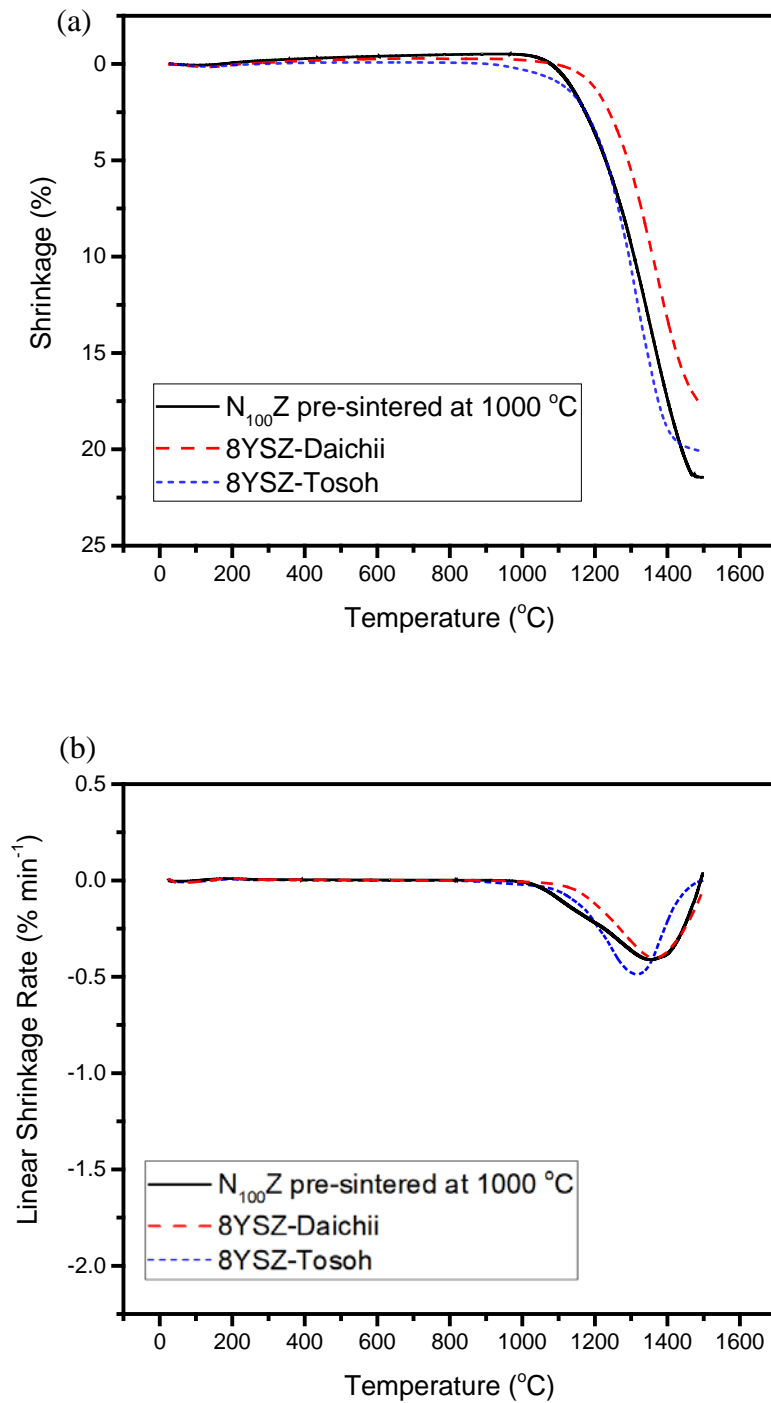


Fig. 4.33 Shrinkage behavior (a) shrinkage and (b) shrinkage rate of 8YSZ-D, 8YSZ-T and  $N_{100}Z$  presintered at 1000 °C with a heating rate of 5 °C min<sup>-1</sup> in air.

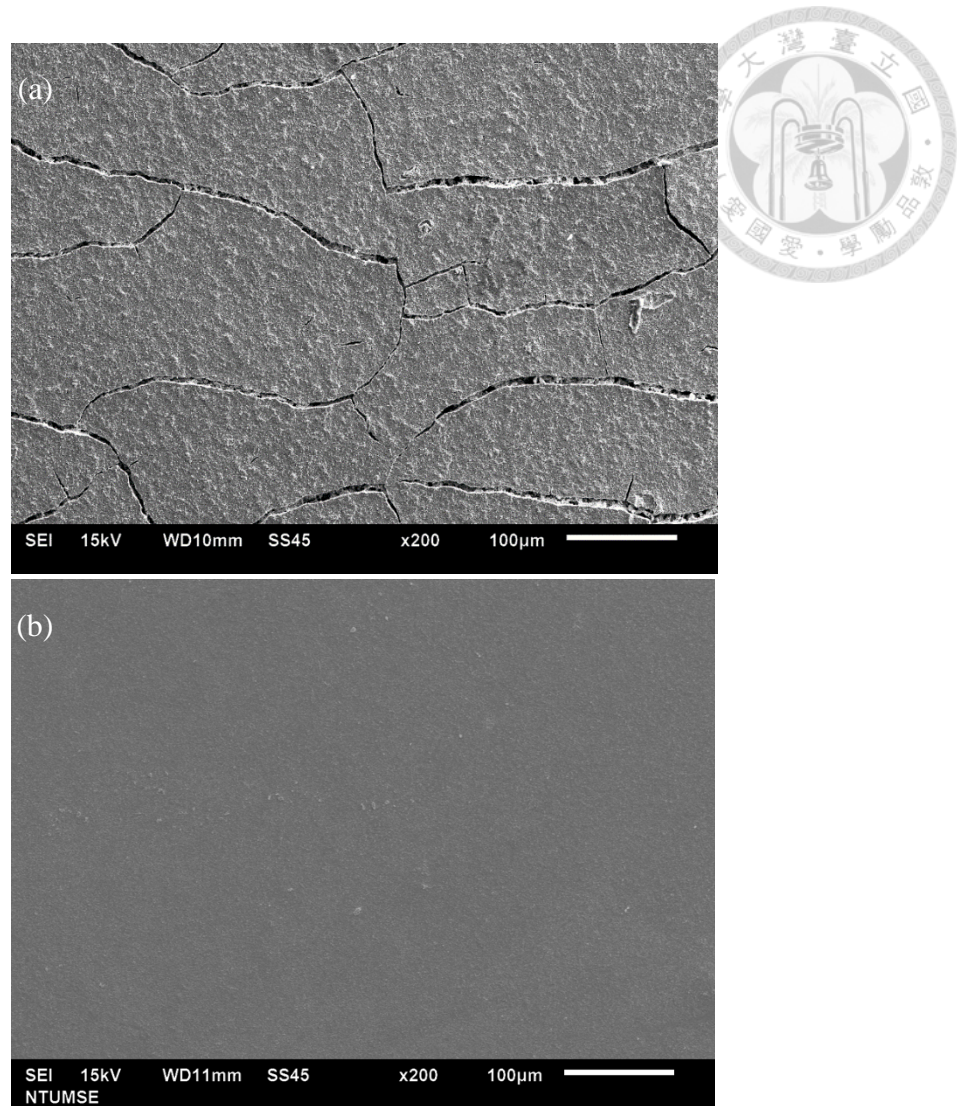


Fig. 4.34 SEM micrographs of top view of  $N_{100}Z$  anode (a) with one layer of 8YSZ-N and two-layer 8YSZ-D sintered at 1400 °C, (b) with one layer of 8YSZ-N and two-layer of 8YSZ-T sintered at 1400 °C.

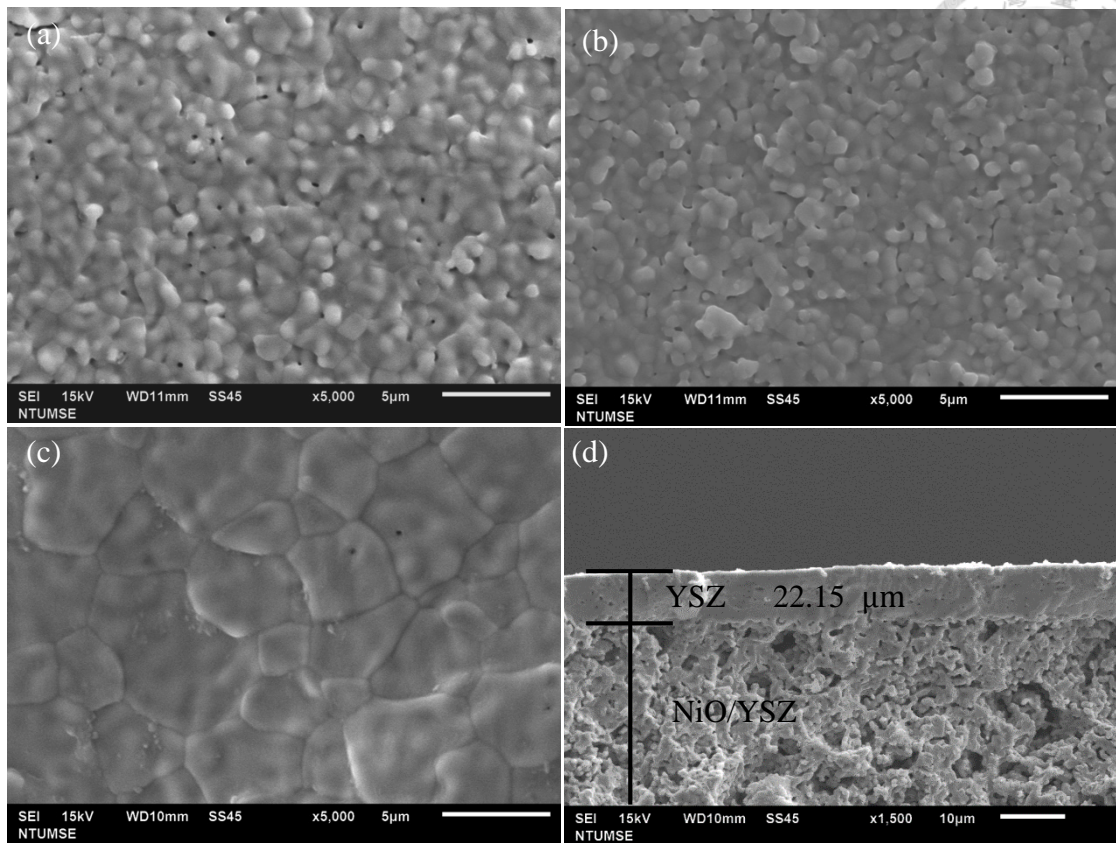


Fig. 4.35 SEM micrograph of top view of  $N_{100}Z$  anode with one layer of 8YSZ-N and two-layer 8YSZ-T sintered at (a) 1400 °C, (b) 1450 °C, (c) 1500 °C for 1 h and (d) cross-section sintered at 1500 °C.




### 4.3.2 C<sub>50</sub>N<sub>50</sub>Z Anode Supported Cell

To prepare C<sub>50</sub>N<sub>50</sub>Z anode support cell, we tried to use same experimental procedure as N<sub>100</sub>Z. During the co-sintering process, CTE mismatch of anode and electrolyte may lead to cell warpage. We put a porous alumina plate on the sample to solve this problem. However, new phases CuAl<sub>2</sub>O<sub>4</sub> and CuAlO<sub>2</sub> begin to show when the temperature is higher than 1050 °C [55]. The C<sub>50</sub>N<sub>50</sub>Z would react with the alumina plate during co sintering process. Instead of that, a porous zirconia plate was used and nearly no sticking and reaction phases.

First, C<sub>50</sub>N<sub>50</sub>Z were pre-sintered at 900 °C, 1000 °C, and 1100 °C, the diameter of each is 29.2±0.05 mm, 27.80±0.20 mm and 25.65±0.10 mm, and the linear shrinkage is 2.67±0.17%, 7.33±0.67% and 14.5±0.35%, respectively. However, the strength of the disk by 900 °C is weak, and not suitable for being used in spin-coating process. For a better understanding of the differences in shrinkage behavior during heating, another two anodes were prepared and compared with 8YSZ-T.

The shrinkage and shrinkage rate are shown on Fig. 4.36. There is two-step shrinkage of C<sub>50</sub>N<sub>50</sub>Z. Before the temperature reaching 1130 °C, the shrinkage of C<sub>50</sub>N<sub>50</sub>Z pre-sintered at 1000 °C and 1100 °C are 8.83% and 2.18%. After that, the sample continued shrinking at a lower rate. However, both of them have less shrinkage than 8YSZ-T. Fig. 4.36 (b) illustrates the shrinkage rate of C<sub>50</sub>N<sub>50</sub>Z pre-sintered at 1000 °C




and 1100 °C. The  $C_{50}N_{50}Z$  exhibits two maximums in shrinkage rate either at 1070 °C or 1125 °C, indicating some reactions during the sintering process. According to Ran's report [56], CuO starts to dissociate to  $Cu_2O$  at 1030 °C. The volume of  $Cu_2O$  is theoretically 12% less than that of CuO. So, we assume the first maximum is caused by the dissociation of CuO. While the melting point of  $Cu_2O$  is around 1125 °C. The liquid phase is resulted in the enhancement of the shrinkage and show the second maximum. After 1200 °C, melted  $Cu_2O$  starts to volatile. But there is only one maximum at 1315 °C in the curve of the densification rate of 8YSZ-T.

The shrinkage of  $C_{50}N_{50}Z$  pre-sintered at 1100 °C is too small to enhance the sintering of coated 8YSZ layer. So, we pre-sintered the anode at 1000 °C in the following test, which is shown in Fig. 4.37 (a). Then  $C_{50}N_{50}Z$  substrate was spin-coated with one layer of 8YSZ-N and two layers of 8YSZ-T, as shown in Fig. 4.37 (b). After sintered at 1000 °C, the pores are fully covered by 8YSZ. In order to make a dense 8YSZ layer, we tried to co-sintered  $C_{50}N_{50}Z$  half-cell at 1300 °C, 1350 °C and 1400 °C, and concerned the melting point 1326 °C of CuO. The results are shown in Fig. 4.38, which show a top view and cross-section of  $C_{50}N_{50}Z$  half-cell sintered at 1300 °C. There are 8YSZ particles on the surface, which may be caused by the porous zirconia plate. Moreover, the pores made by MCMB are too big and hold not enough particles after the heating process.

The thickness of 8YSZ layer on anode sintered at 1300 °C is around  $2.27 \pm 0.91$   $\mu m$ .





As temperature increased to 1350 °C, the remaining 8YSZ grains grew but still some pores remained on the surface in Fig. 4.38 (c). The thickness of 8YSZ sintered at 1350 °C is around  $3.07 \pm 0.80$  μm. In Fig. 4.38 (e), the morphology of 8YSZ sintered at 1400 °C became different and the grains had grown obviously. This might be due to the diffusion and volatile of copper. From the cross-section of view, distortion of the electrolyte layer was observed when the temperature increased.

In order to improve the performance of C<sub>50</sub>N<sub>50</sub>Z anode supported half-cell. Two powders, C<sub>50</sub>N<sub>50</sub>Z without MCMB and C<sub>50</sub>N<sub>50</sub>Z with 5 wt% MCMB, were used as anode materials. Fig. 4.39 (a) shows that the C<sub>50</sub>N<sub>50</sub>Z half-cell without MCMB co-sintered at 1200 °C appears no big pores on the 8YSZ surface. In Fig. 4.39 (c), C<sub>50</sub>N<sub>50</sub>Z half-cell with 5 wt% MCMB co-sintered at 1200 °C has same problems. The big pores made by MCMB still exist. The surface pores cannot be eliminated even if the temperature is increased to 1400 °C, as shown in Fig. 4.39 (e). In the cross-section of these two half-cells, the thickness of C<sub>50</sub>N<sub>50</sub>Z half-cell without MCMB and with 5 wt% MCMB is  $6.40 \pm 1.60$  μm and  $4.8 \pm 0.4$  μm, respectively. The lower the porosity, the thicker the electrolyte. In this test, a full densification of the 8YSZ electrolyte is difficult to achieve while co-sintering with C<sub>50</sub>N<sub>50</sub>Z anode.

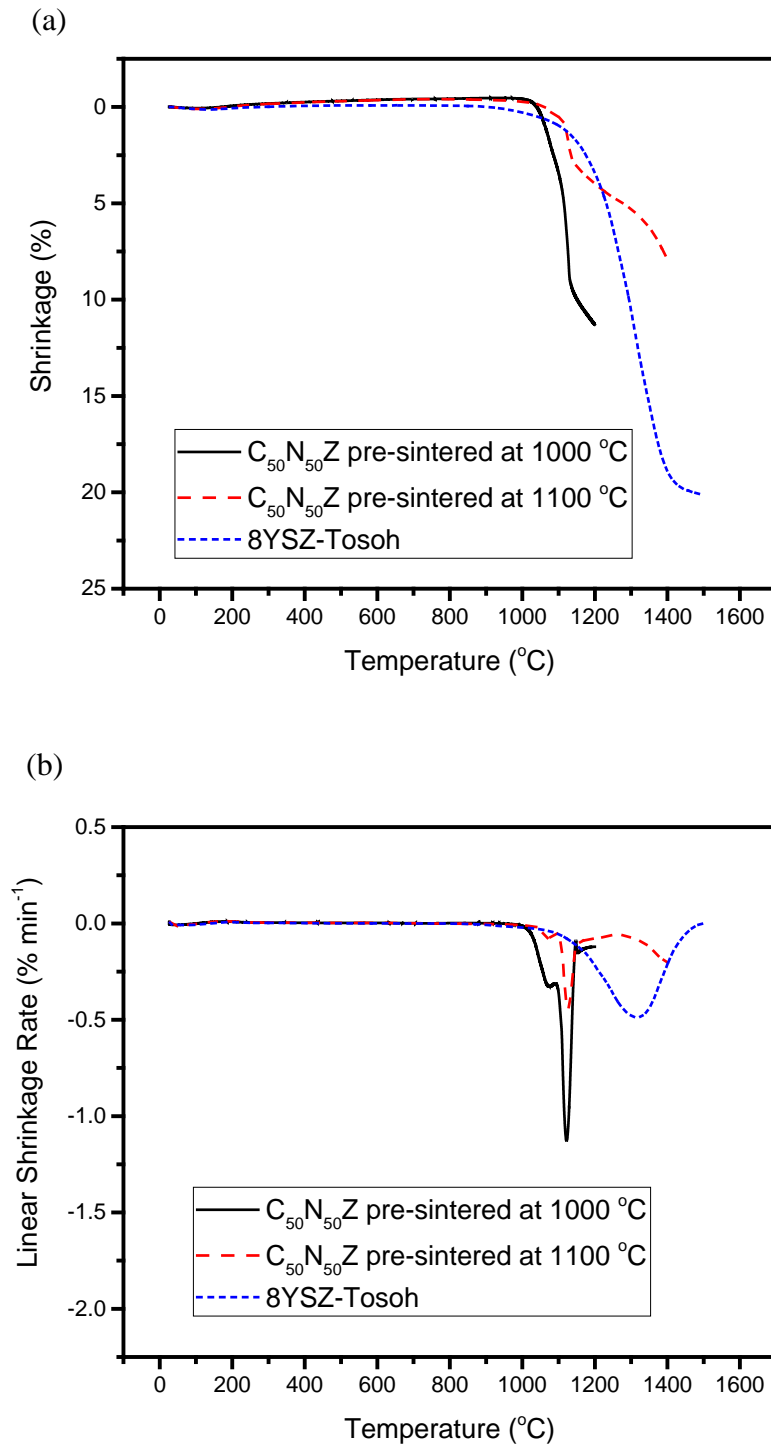


Fig. 4.36 The Shrinkage behavior of 8YSZ-T and  $C_{50}N_{50}Z$  presintered at 1000 °C or at 1100 °C at a heating rate of 5 °Cmin<sup>-1</sup> in air.



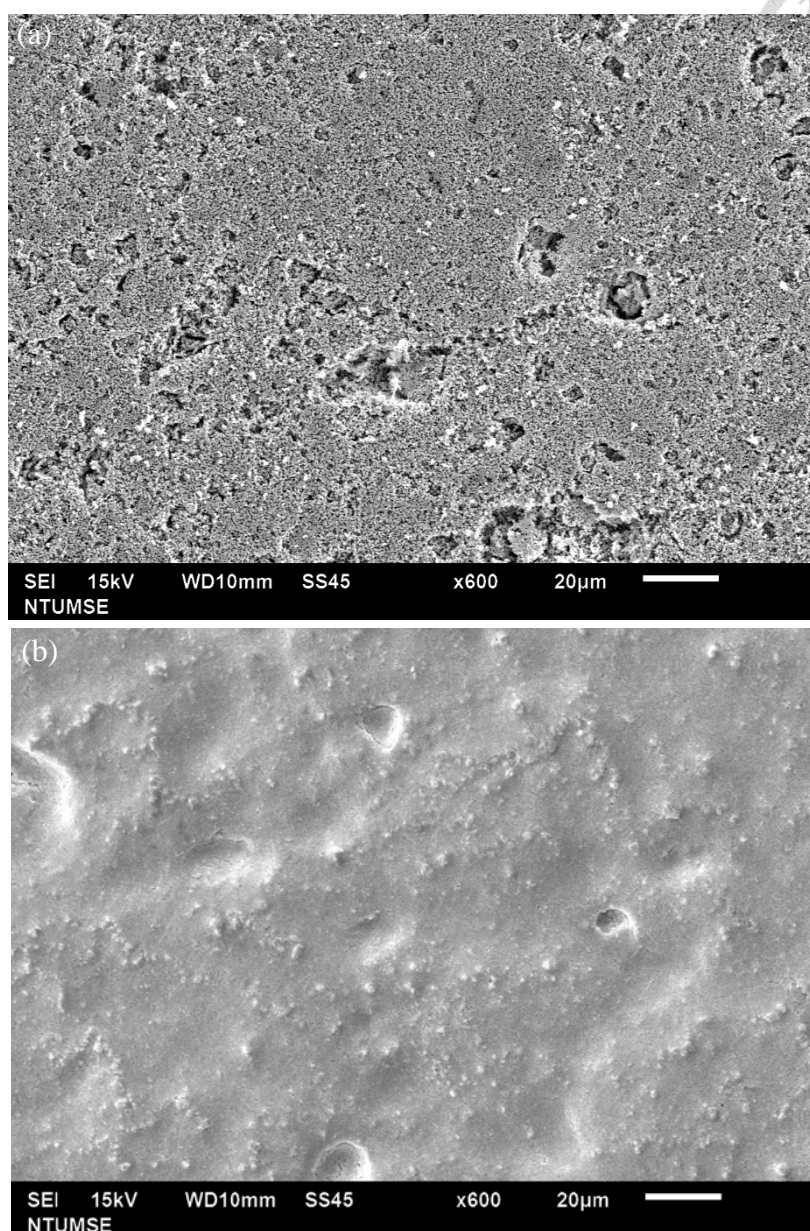


Fig. 4.37 SEM micrograph of top view of  $C_{50}N_{50}Z$  anode (a) pre-sintered at 1000 °C, (b) with one layer of 8YSZ-N and two layers 8YSZ-T sintered at 1000 °C.

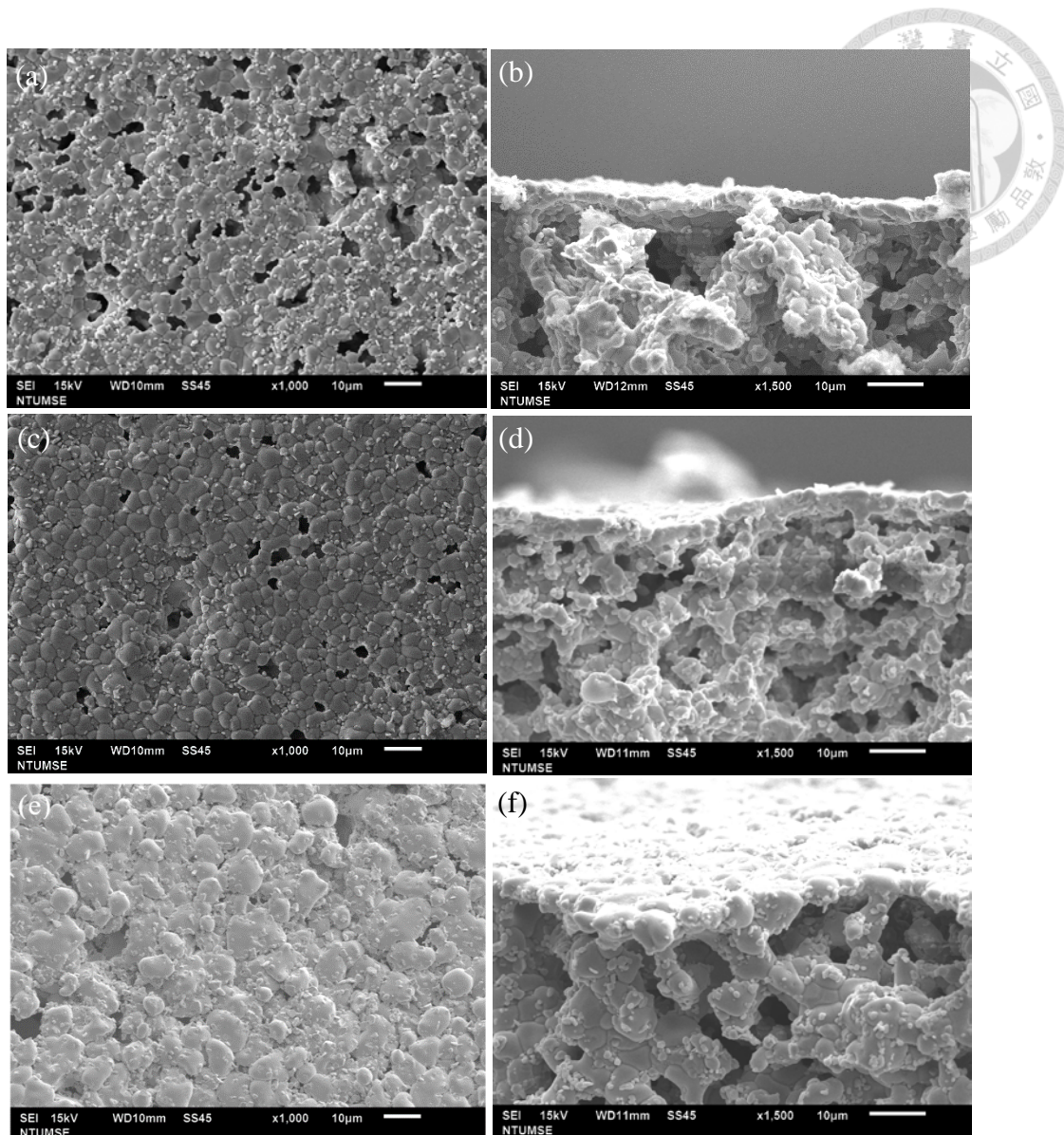


Fig. 4.38 SEM micrographs of top view and cross-section of  $C_{50}N_{50}Z$  anode (with 20 wt% MCMB) spin-coated one layer of 8YSZ-N and two layers 8YSZ-T. (a) and (b) sintered at 1300 °C, (c) and (d) sintered at 1350 °C, (e) and (f) sintered at 1400 °C.



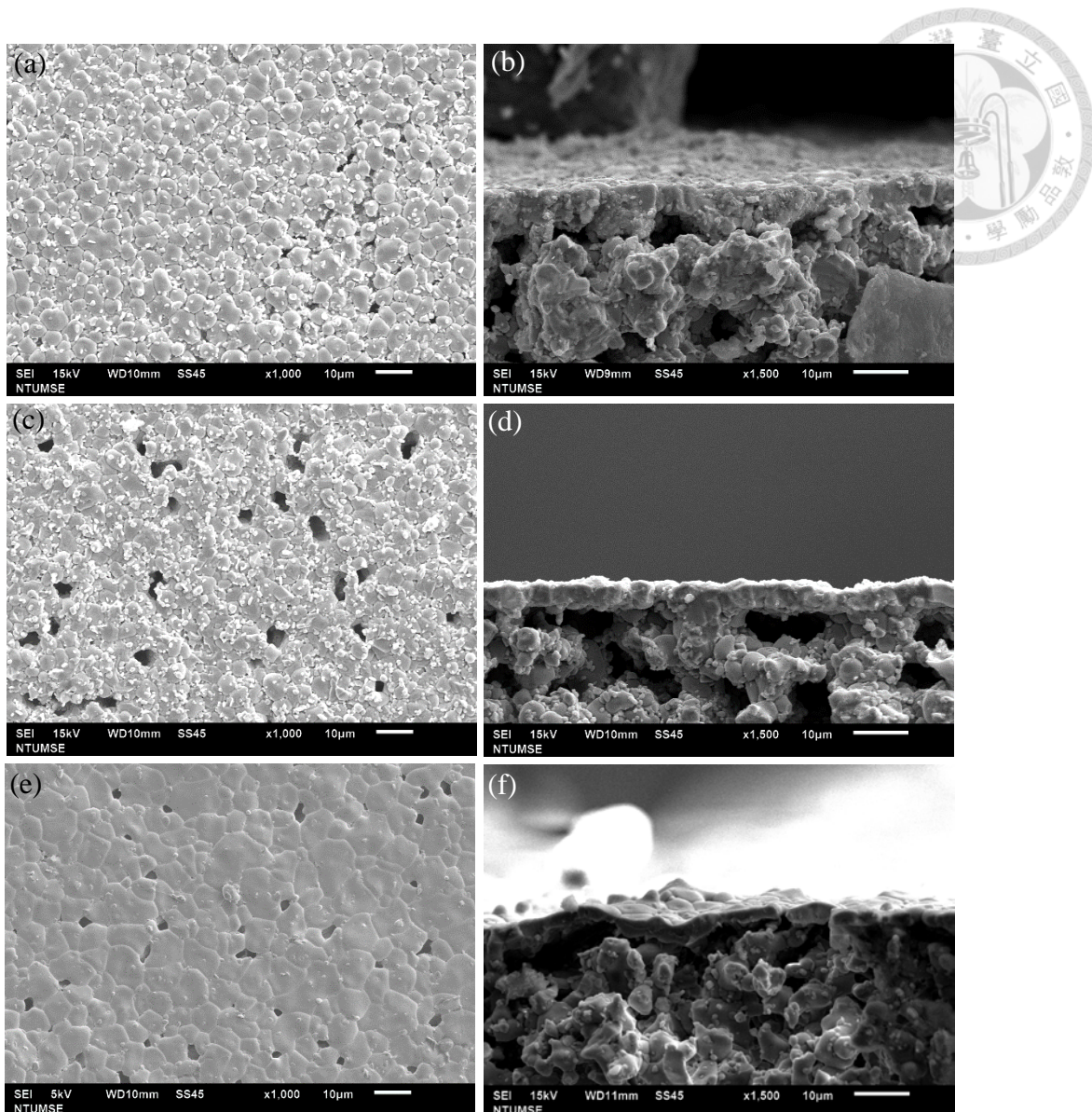


Fig. 4.39 SEM micrographs of the top view and cross-section of  $C_{50}N_{50}Z$  anode spin-coated one layer of 8YSZ-N and two layers of 8YSZ-T. (a) and (b) sintered at 1200 °C (without MCMB), (c) and (d) sintered at 1200 °C (with 5 wt% MCMB), (e) and (f) sintered at 1400 °C (with 5 wt% MCMB).

### 4.3.3 Improvement of C<sub>50</sub>N<sub>50</sub>Z Anode Supported Cell



In previous section, C<sub>50</sub>N<sub>50</sub>Z anode material has several difficulties to co-sinter with 8YSZ electrolyte. First, the wetting properties of copper oxide are better than nickel oxide on 8YSZ. Without adding pore former, C<sub>50</sub>N<sub>50</sub>Z can form connecting pores which are an advantage for porous anode in SOFC. However, it also is a fatal flaw when using spin-coating method to fabricate 8YSZ electrolyte due to the pore size too big for 8YSZ particles bridging on it, so there still some pores remained on the surface of half-cell.

Second, the shrinkage ranges of C<sub>50</sub>N<sub>50</sub>Z and 8YSZ-T is different in temperature. C<sub>50</sub>N<sub>50</sub>Z anode completely shrinkage at 1200 °C and while 8YSZ-T just start to shrinkage. For this reason, C<sub>50</sub>N<sub>50</sub>Z help 8YSZ-T to sintering, but not forming a dense electrolyte layer at 1200 °C. If sintering higher than 1200 °C, there might be large amount of copper diffusion and volatilization. Thus, we tried to use a NiO/8YSZ anode function layer (AFL) to solve these problems.

C<sub>50</sub>N<sub>50</sub>Z anode without MCMB was first pre-sintered at 1200 °C (Fig. 4.40 (a)) and reduced in H<sub>2</sub> at 600 °C for 1 h, as shown in Fig. 4.40 (b). The substrate will not shrink and influence the following process. Then, a slurry of AFL was prepared by ball-milling NiO and 8YSZ-T powders in ethyl cellulose (a binder) and terpineol (a carrier) in a mass ratio of 15:15:2:68 for 24 h. The viscosity of NiO and 8YSZ-T slurry was increased to bridge on the big pores of C<sub>50</sub>N<sub>50</sub>Z anode. The AFL slurry was spin-coated 2 cycles

(5000 rpm, 60s) and sintered at 1000 °C. In Fig.4.41 (a) and (b), AFL has flattened the surface of C<sub>50</sub>N<sub>50</sub>Z anode and had an average thickness of  $5.57 \pm 0.62 \mu\text{m}$ .

After that 8YSZ-T slurry was spin-coated 2 cycles and co-sintered at 1200 °C for 3 h. Finally, we used LSCF powder mixing with PEG and 2 wt% D-134 (a dispersant) as cathode slurry and spin-coated one cycle on the electrolyte layer. Then the single cell was sintered at 1150 °C for 1 h. In Fig.4.41 (c), the thickness of electrolyte and cathode are  $8.02 \pm 1.31 \mu\text{m}$  and  $14.3 \pm 0.91 \mu\text{m}$ , respectively.

Besides the flattened surface on C<sub>50</sub>N<sub>50</sub>Z anode, this anode function layer may have the other three advantages. Because AFL has a higher shrinkage and similar shrinkage temperature range with 8YSZ-T. This can help densification of 8YSZ electrolyte at 1200 °C. Fig.4.41 (d) shows that the 8YSZ particles which contacted with AFL are sintered and formed a dense layer without big pores.

The NiO/YSZ AFL can be a barrier layer for copper diffusion. If copper diffuses apparently into 8YSZ electrolyte layer, it may influence the characteristic of 8YSZ. By the way, some copper diffusing into AFL can reduce carbon deposition when using hydrocarbon fuels. The CTE of Cu, Ni and 8YSZ are  $16.5 \text{ ppmK}^{-1}$ ,  $13.4 \text{ ppmK}^{-1}$  and  $10.5 \text{ ppmK}^{-1}$ , which have shown in Table 2.1. Therefore, the CTE of NiO/YSZ AFL is between C<sub>50</sub>N<sub>50</sub>Z and 8YSZ and can be treated as a buffer layer. The chance of delamination of cell is decreased in the following thermal process and during cell test.

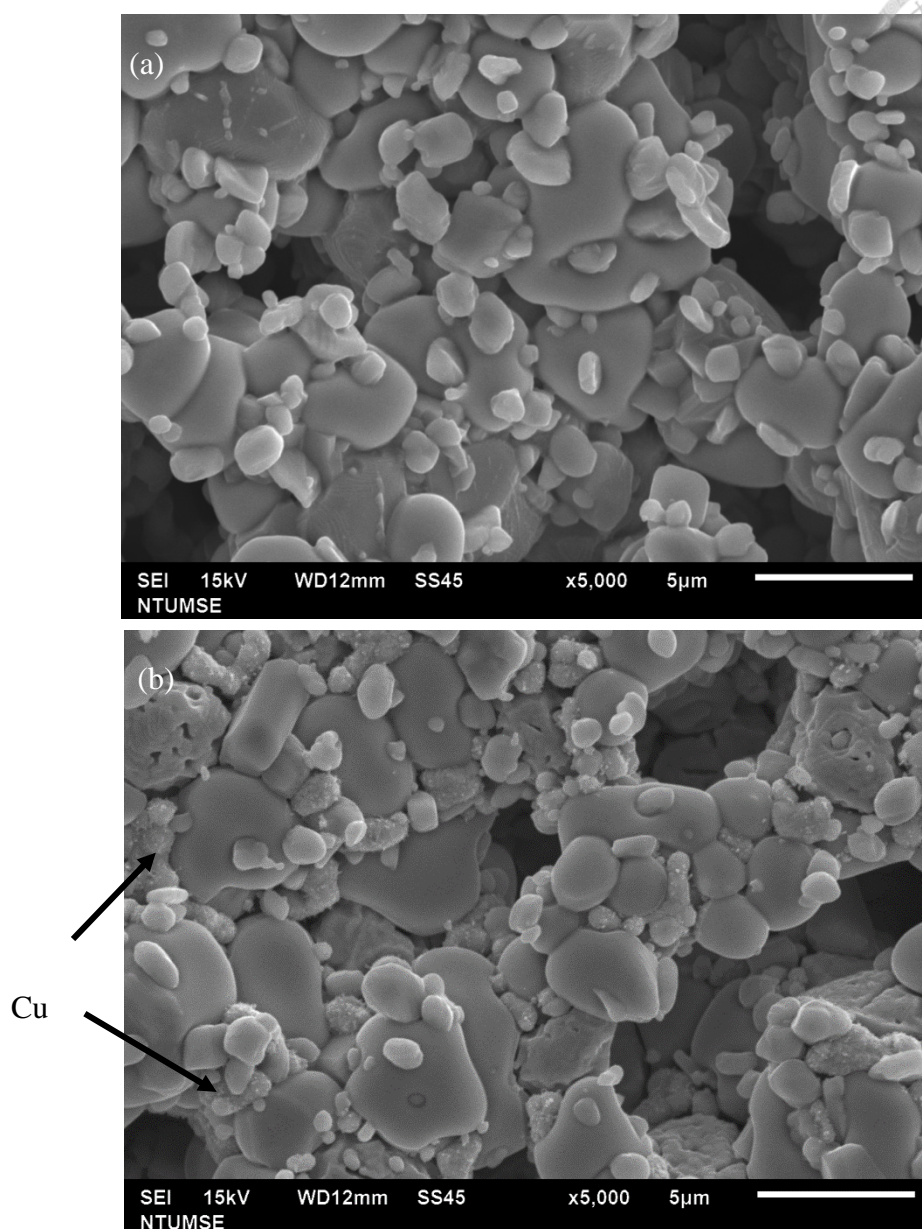
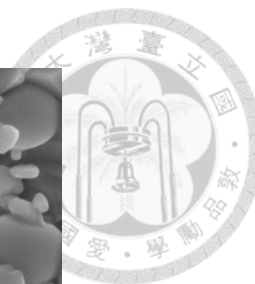


Fig. 4.40 SEM micrographs of  $C_{50}N_{50}Z$  anode without MCMB. The anode (a) sintered at 1200 °C, and then (b) reduced at 600 °C for 1 h by  $H_2$ .



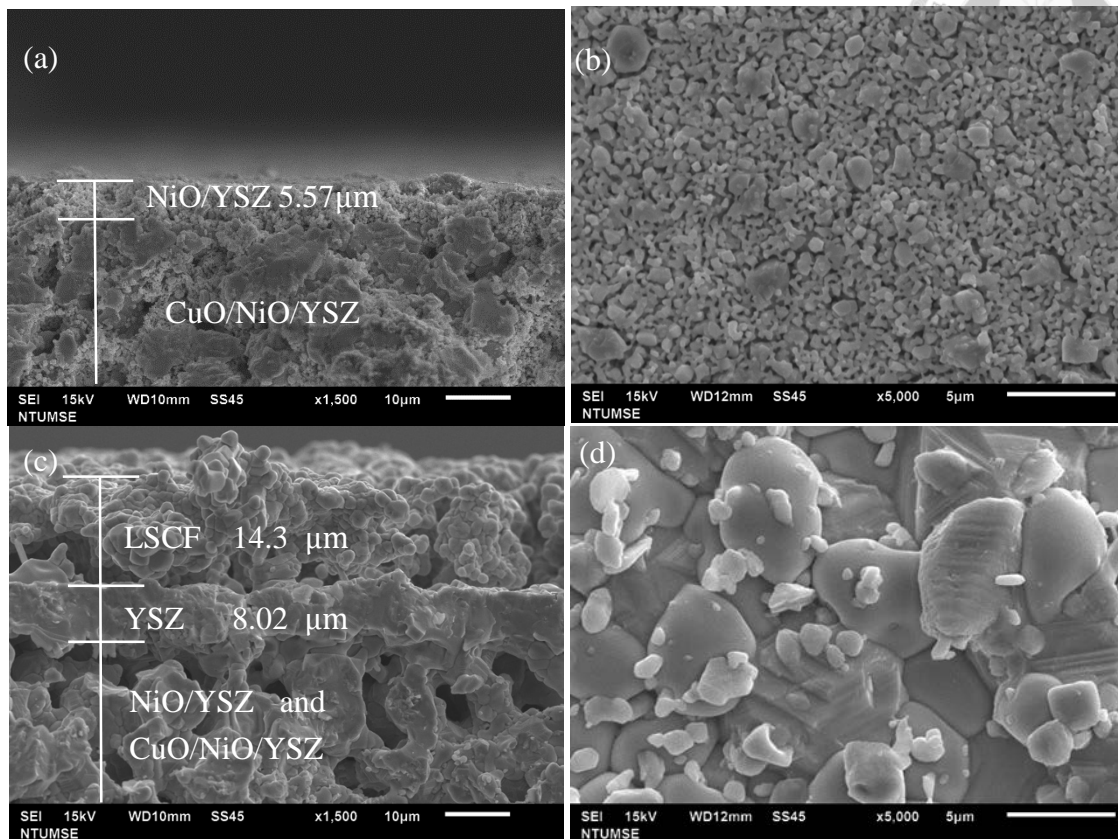


Fig.4.41 SEM micrographs of (a) cross-section and (b) top view of anode and anode function layer (AFL), which was made by using spin-coating, (c) cross-section of single cell showing the thickness of individual layer, (d) top view of spin-coated two-layer of 8YSZ.

## Chapter 5 Conclusions



This study has demonstrated the electrical properties of Cu-based and nickel wires.

The performance of five thermocouples made by above wires were studied in long-term test. This study also investigated the porosity, catalytic properties, electrical conductivity of three different ratios of CuO/NiO anode samples. Besides, Cu-based anode supported cell has been assembled and improved. The results are summarized as below.

1. The conductivity of C, C11N, CZ and N wires are  $59.2 \times 10^6 \text{ S}\cdot\text{m}^{-1}$ ,  $5.36 \times 10^6 \text{ S}\cdot\text{m}^{-1}$ ,  $10.57 \times 10^6 \text{ S}\cdot\text{m}^{-1}$  and  $13.5 \times 10^6 \text{ S}\cdot\text{m}^{-1}$ , respectively at room temperature. When the temperature increases, the conductivity of metal decreases. However, the conductivity of Cu at 650 °C is  $16.9 \times 10^6 \text{ S}\cdot\text{m}^{-1}$  and good enough for using as a current collector in SOFC.
2. The Seebeck coefficient of the thermocouple from high to low is C-C11N, C11N-CZ, C-C9N6S, C-N and C-CZ at 650 °C. Thus, three thermocouples (C-C11N, C-C9N6S and C-N) show good sensitivity, less response time and high stability in long-term test, and suitable for temperature sensing for IT-SOFC.
3. In catalytic analysis of carbon deposition, the content of H<sub>2</sub> through N<sub>100</sub>Z which reacts with CH<sub>4</sub> was up to 35%, gradually decreases in 2 h. This is bad for using in SOFC. In contrast, the catalytic ability of C<sub>50</sub>N<sub>50</sub>Z is lower than N<sub>100</sub>Z. But the H<sub>2</sub> content of C<sub>50</sub>N<sub>50</sub>Z stably increases for the first 1.5 h. The C<sub>100</sub>Z shows rarely H<sub>2</sub> formation as





reforming  $\text{CH}_4$  in this test.

4. In permeability test, both  $\text{N}_{100}\text{Z}$  and  $\text{C}_{50}\text{N}_{50}\text{Z}$  tests with  $\text{CH}_4$  have carbon deposition.

After reforming  $\text{CH}_4$  for 2 h, the permeability of  $\text{N}_{100}\text{Z}$  and  $\text{C}_{50}\text{N}_{50}\text{Z}$  decreased nearly 6 times and 21 times, respectively. However, carbon deposition rate of  $\text{N}_{100}\text{Z}$  is much faster than that of  $\text{C}_{50}\text{N}_{50}\text{Z}$ . Thus, the  $\text{C}_{50}\text{N}_{50}\text{Z}$  is a candidate of anode material to use in hydrocarbon fuels.

5. The electrical conductivity of  $\text{N}_{100}\text{Z}$  anode sintered at  $1500\text{ }^\circ\text{C}$  with 20 wt% MCMB is  $482.75\text{ Scm}^{-1}$  at  $650\text{ }^\circ\text{C}$  and  $363.52\text{ Scm}^{-1}$  at  $800\text{ }^\circ\text{C}$ . While the electrical conductivity of  $\text{C}_{50}\text{N}_{50}\text{Z}$  sintered at  $1300\text{ }^\circ\text{C}$  without MCMB is  $1503.37\text{ Scm}^{-1}$  at  $650\text{ }^\circ\text{C}$  and  $959.60\text{ Scm}^{-1}$  at  $800\text{ }^\circ\text{C}$ .
6.  $\text{C}_{50}\text{N}_{50}\text{Z}$  is difficult to co-sinter with 8YSZ because of high wetting properties and low melting point of  $\text{CuO}$ . A newly designed half-cell with multilayer structure,  $\text{C}_{50}\text{N}_{50}\text{Z}/\text{N}_{100}\text{Z}(\text{AFL})/\text{YSZ}/\text{LSCF}$ , has overcome the situations.

## Appendix 1



Three anode samples using liquefied petroleum gas (LPG) is tested in order to observe possible reforming of LPG gas through the anodes at 650 °C. LPG is flammable mixtures of mainly propane ( $C_3H_8$ ) used as a fuel in heating appliances, cooking equipment, and vehicles. [Fig. A-1](#) shows that LPG reforms at different temperatures. Propane dehydrogenation is the main reaction which starts nearly at 600 °C. In addition, there are five reactions may happen [57]:



The content of  $H_2$  is between 17.2% to 23.1% at 600 °C to 750 °C and obviously increasing to 32.9% at 800 °C. Meanwhile, the content of  $CH_4$  was almost double to the content of  $H_2$ . The reforming rate of LPG increases at higher temperature.

A LPG at a flow rate of  $10 \text{ mlmin}^{-1}$  flows through anode samples was conducted during the heating process from room temperatures to 650 °C and lasted for 2 h. Then reacting gas was collected at 300 °C and 650 °C in every 30 min. [Fig. A-2](#) and [Fig. A-3](#)

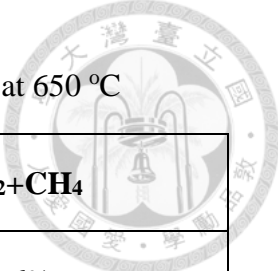
are the contents of  $H_2$  and  $CH_4$  respectively. The reforming rate of  $C_3H_8$  from high to low is  $C_{50}N_{50}Z$ ,  $N_{100}Z$  and  $C_{100}Z$ , as shown in Table A-1.



[Fig. A-2](#) shows the content of hydrogen in reacting gas. The  $H_2$  content of  $C_{100}Z$  is 17.81% when the temperature reaches 650 °C. Then it increases to 37.41% after 30 min and slight decreases as the time increases. The  $H_2$  content of  $C_{50}N_{50}Z$  had maximum range from 41.4% to 50.0%. Whereas the  $H_2$  content of  $N_{100}Z$  shows only 13.31% to 16.89% at 650 °C. It's lower than no catalytic carrier, the reason may be caused by rapid carbon deposition at beginning. [Fig. A-3](#) shows the  $CH_4$  content of three anodes. The  $CH_4$  content of  $C_{100}Z$  tends to in a balance of 44.8%. In contrast, the  $CH_4$  content of  $C_{50}N_{50}Z$  and  $N_{100}Z$  decreases as the time increases.

The reaction of LPG is complicated and difficult to determine which reaction is dominating. After the test, a lot of carbon in the tube and sample was obtained, as shown in [Fig. A-4](#). Therefore, LPG is not suitable for using on SOFC without appropriately reforming.

Table A-2 Content of H<sub>2</sub> and CH<sub>4</sub> in LPG after reacting with sample at 650 °C



Sample	Time (min)	H <sub>2</sub>	CH <sub>4</sub>	H <sub>2</sub> +CH <sub>4</sub>
None	0	23.1%	55.5%	78.6%
<b>C<sub>100</sub>Z</b>	0	17.8%	45.2%	63.0%
	30	37.4%	42.5%	79.9%
	60	37.8%	43.8%	81.6%
	90	35.0%	48.1%	83.1%
	120	36.7%	41.6%	78.3%
<b>C<sub>50</sub>N<sub>50</sub>Z</b>	0	50.0%	39.0%	89.0%
	30	48.5%	26.0%	74.5%
	60	45.5%	26.6%	72.1%
	90	45.0%	19.7%	64.7%
	120	41.4%	25.4%	66.8%
<b>N<sub>100</sub>Z</b>	0	16.9%	55.5%	72.4%
	30	14.9%	59.2%	74.1%
	60	13.3%	57.0%	70.3%
	90	15.8%	39.4%	55.2%
	120	14.8%	36.7%	51.5%

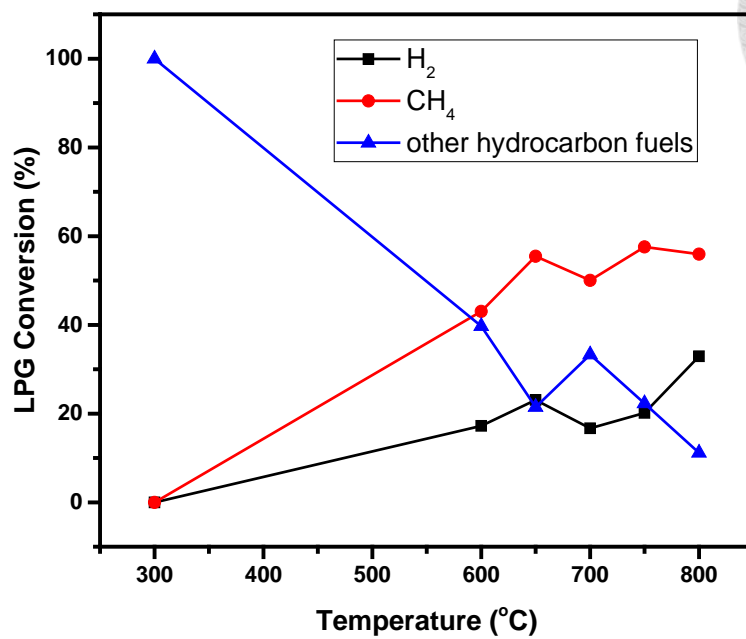


Fig. A-1 GC results of the reforming of LPG gas at a flow rate of 10 mlmin<sup>-1</sup> at different temperatures.

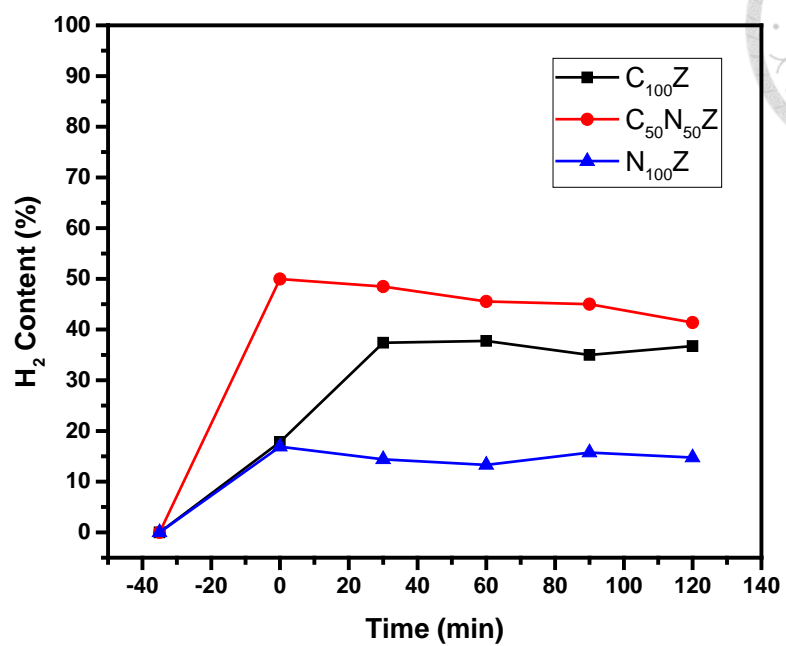


Fig. A-2 Content of H<sub>2</sub> in the reforming gas (LPG) through three anodes C<sub>100</sub>Z, C<sub>50</sub>N<sub>50</sub>Z and N<sub>100</sub>Z at 650 °C in 2 h.

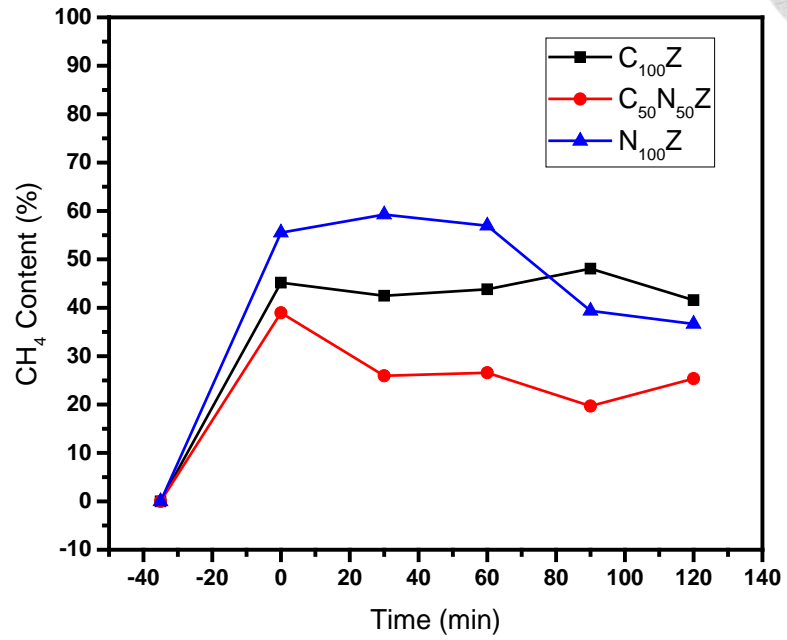


Fig. A-3 Content of  $CH_4$  in reforming gas (LPG) through three anodes  $C_{100}Z$ ,  $C_{50}N_{50}Z$  and  $N_{100}Z$  at  $650\text{ }^{\circ}C$  in 2 h.

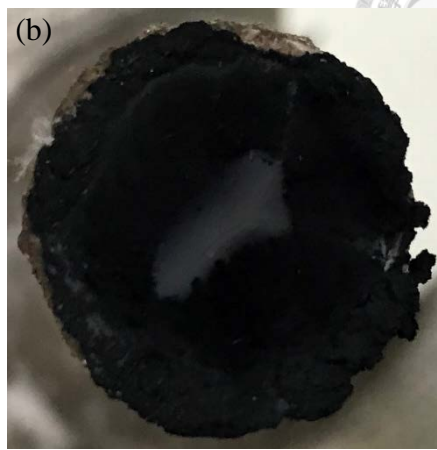
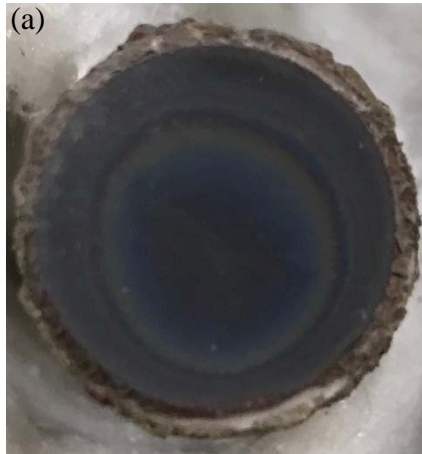


Fig. A- 4 (a) N<sub>100</sub>Z anode sintered at 1400 °C before tested with LPG, (b) carbon deposition on the N<sub>100</sub>Z anode after reacting with LPG for 2 h at 650 °C.



## Appendix 2



Two different structure single cells were sealed by ceramic paste and tested from 600 °C to 800 °C for IV curve. First cell (cell 1) is an 8YSZ electrolyte support cell, the thickness of electrolyte is 100  $\mu\text{m}$ . Each surface of electrolyte was printed by CuO/NiO/YSZ anode and LSCF/GDC cathode, respectively. The electrodes were co-sintered at 1000 °C for both anode and cathode. The cross-section of the full cell is shown in Fig. A-5(a).

The power density of the cell 1 was tested in 50 ml min<sup>-1</sup> H<sub>2</sub> flowing at the anode side and 250 ml min<sup>-1</sup> air flowing at the cathode side. The OCV value of the cell at 800 °C is 1.06 V, but the maximum output is 0.90 mW cm<sup>-2</sup>, which is shown in Fig. A-5(b). These may be caused by high interface resistance.

Cell 2 was used N<sub>100</sub>Z half cell (Fig. 4.35) with LSCF/GDC cathode, and also printed a CuO/NiO/YSZ anode layer. A four-layer structure was shown in Fig. A-6 (a) and (b). The OCV value of the cell was between 0.55 V to 1.03 V at 600 °C. The power density was very small and failed to operate at 650 °C. Leakage problem in electrolyte might result in this unstable OCV value and low power output.

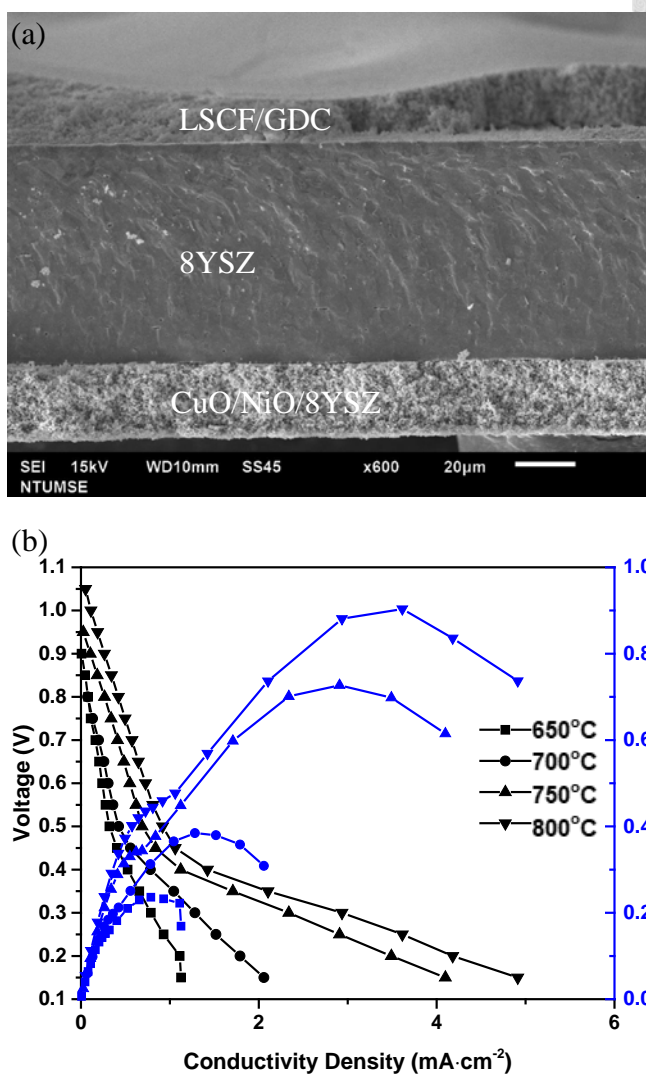


Fig. A-5 (a) Cross- section of cell 1, (b) I-V curve and power density of cell 1 using H<sub>2</sub> as a fuel

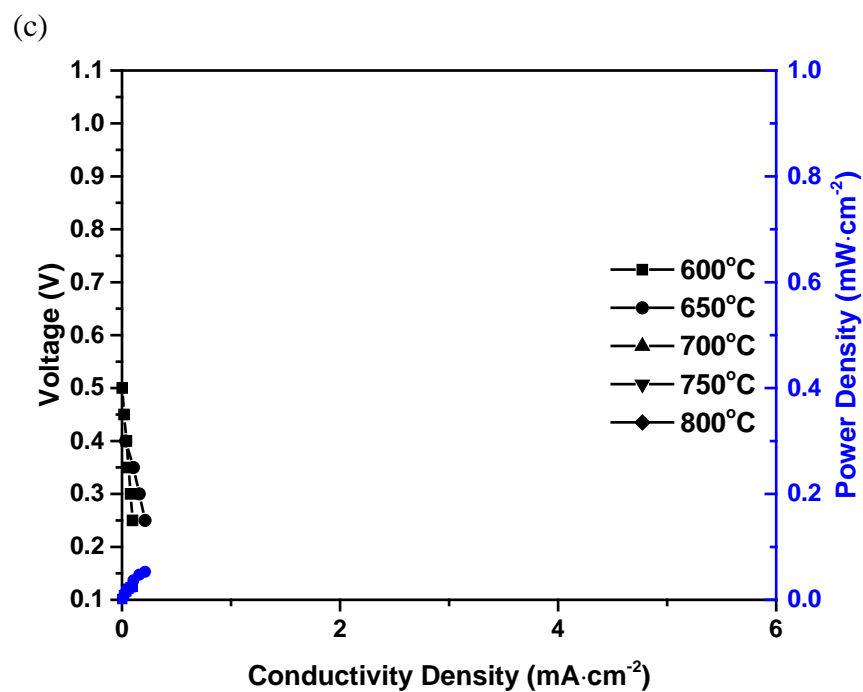
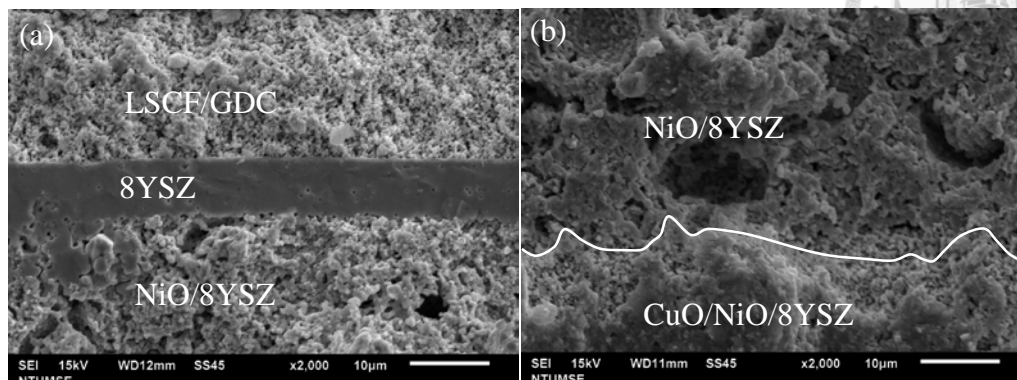


Fig. A-6 (a), (b) Cross- section of cell 2, (c) I-V curve and power density of cell 2 using H<sub>2</sub> as a fuel


## REFERENCE



- [1] 韋文誠，“固態燃料電池技術”，高立圖書，(2013)
- [2] Z. Lu, L. Pei, T. M. He, X. Q. Huang, Z. G. Liu, Y. Ji, X. H. Zhao, and W. H. Su,  
“ Study on new copper-containing SOFC anode materials”, Journal of Alloys and  
Compounds, 334 (2002) 299–303.
- [3] S. McIntosh and R. J. Gorte, “Direct Hydrocarbon Solid Oxide Fuel Cells”,  
Chemical Reviews, 104[10] (2004) 4845-4865.
- [4] G.O. Brown, “Henry Darcy and the making of a law”, Water Resources Research,  
38[7] (2002) 11-1-11-12.
- [5] Z. Zeng, and R. Grigg, “A Criterion for Non-Darcy Flow in Porous Media”,  
Transport in Porous Media, 63[1] (2006) 57-69.
- [6] X.-M. Ge, S.-H. Chan, Q.-L. Liu, and Q. Sun, “Solid Oxide Fuel Cell Anode  
Materials for Direct Hydrocarbon Utilization”, Advanced Energy Materials, 2[10]  
(2012) 1156-1181.
- [7] O. Costa-Nunes, R. J. Gorte, and J.M. Vohs, “Comparison of the performance of Cu–  
CeO<sub>2</sub>–YSZ and Ni–YSZ composite SOFC anodes with H<sub>2</sub>, CO, and syngas”, Journal  
of Power Sources, 141[2] (2005) 241-249.
- [8] Y. Matsuzaki, and I. Yasuda, “The poisoning effect of sulfur-containing impurity gas  
on a SOFC anode: Part I. Dependence on temperature, time, and impurity

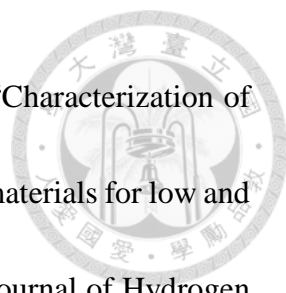


- concentration”, *Solid State Ionics*, 132 (2000) 261–269.
- [9] H.P. He, A. Wood, D. Steedman, and M. Tilleman, “Sulphur tolerant shift reaction catalysts for nickel-based SOFC anode”, *Solid State Ionics*, 179[27-32] (2008) 1478-1482.
- [10] H. He, R. J. Gorte, and J.M. Vohs, “Highly Sulfur Tolerant Cu-Ceria Anodes for SOFCs”, *Electrochemical and Solid-State Letters*, 8[6] (2005) A279.
- [11] V. De Marco, A. Iannaci, S. Rashid, and V. M. Sglavo, “Effect of anode thickness and Cu content on consolidation and performance of planar copper-based anode-supported SOFC”, *International Journal of Hydrogen Energy*, 42[17] (2017) 12543-12550.
- [12] R. Raza, X. Wang, Y. Ma, X. R. Liu, and B. Zhu, “Improved ceria–carbonate composite electrolytes”, *International Journal of Hydrogen Energy*, 35[7] (2010) 2684-2688.
- [13] X.-F. Ye, B. Huang, S. R. Wang, L. Xiong, and T. L. Wen, “Preparation and performance of a Cu–CeO<sub>2</sub>–ScSZ composite anode for SOFCs running on ethanol fuel”, *Journal of Power Sources*, 164[1] (2007) 203-209.
- [14] M.C. Tucker, G. Y. Lau, C. P. Jacobson, S. J. Visco, and L. C. De Jonghe, “Cu–YSZ cermet solid oxide fuel cell anode prepared by high-temperature sintering”, *Journal of Power Sources*, 195[10] (2010) 3119-3123.

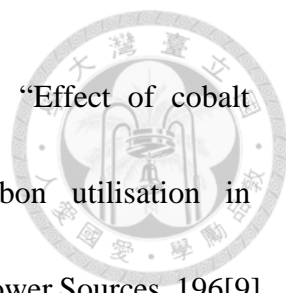
- 
- [15] V. De Maeco, A. Iannaci, S. Rashid, and V. M. Sglavo, “Performance and evolution of planar copper-based anode-supported solid oxide fuel cell”, *Journal of the Ceramic Society of Japan*, 125[4] (2017) P4-1-P4-4.
- [16] S. Basu, G. Kaur, “Physical characterization and electrochemical performance of copper–iron–ceria–YSZ anode-based SOFCs in H<sub>2</sub> and methane fuels”, *International journal of energy research*, 39 (2015) 1345–1354.
- [17] A. Rismanchian, J. Mirzababaei, and S.S.C. Chuang, “Electro-less plated Cu–Ni anode catalyst for natural gas solid oxide fuel cells”, *Catalysis Today*, 245 (2015) 79-85.
- [18] M.A. Bucchieri, and J.M. Hill, “Evaluation of a Cu/YSZ and Ni/YSZ Bilayer Anode for the Direct Utilization of Methane in a Solid-Oxide Fuel Cell. *Fuel Cells*”, 14[2] (2014) 162-170.
- [19] M. Miyake, S. Matsumoto, M. Iwami, S. Nishimoto, and Y. Kameshima, “Electrochemical performances of Ni<sub>1-x</sub>Cu<sub>x</sub>/SDC cermet anodes for intermediate-temperature SOFCs using syngas fuel” *International Journal of Hydrogen Energy*, 41[31] (2016) 13625-13631.
- [20] M. Cuglietta, J. Kuhn, and O. Kesler, “A Novel Hybrid Axial-Radial Atmospheric Plasma Spraying Technique for the Fabrication of Solid Oxide Fuel Cell Anodes Containing Cu, Co, Ni, and Samaria-Doped Ceria”, *Journal of Thermal Spray*



- Technology, 22[5] (2013) 609-621.
- [21] W. Wang, H. Zhu, G. Yang, H. J. Park, D. W. Jung, C. Kawk, and Z. Shao, “A NiFeCu alloy anode catalyst for direct-methane solid oxide fuel cells”, *Journal of Power Sources*, 258 (2014) 134-141.
- [22] G. Kaur, and S. Basu, “Study of Carbon Deposition Behavior on Cu-Co/CeO<sub>2</sub>-YSZ Anodes for Direct Butane Solid Oxide Fuel Cells. Fuel Cells”, 14[6] (2014) 1006-1013.
- [23] Z. Wang, W. Weng, K. Cheng, P. Du, G. Shen, and G. Han, “Catalytic modification of Ni-Sm-doped ceria anodes with copper for direct utilization of dry methane in low-temperature solid oxide fuel cells”, *Journal of Power Sources*, 179[2] (2008) 541-546.
- [24] X. Lu, and J. Zhu, “Cu(Pd)-impregnated La<sub>0.75</sub>Sr<sub>0.25</sub>Cr<sub>0.5</sub>Mn<sub>0.5</sub>O<sub>3-δ</sub> anodes for direct utilization of methane in SOFC”, *Solid State Ionics*, 178[25-26] (2007) 1467-1475.
- [25] N. Droushiotis, F. Dal Grande, M. H. Dzafan Othman, K. Kanawka, U. Doraswami, I. S. Metcalfe, K. Li, and G. Kelsall, “Comparison Between Anode-Supported and Electrolyte-Supported Ni-CGO-LSCF Micro-tubular Solid Oxide Fuel Cells” *Fuel Cells*, 14[2] (2014) 200-211.
- [26] 周志勳，銅基材料於固態燃料電池之應用與熱熔組件開發，國立台灣大學碩士論文，(2015)

- 
- [27] Ö. Yıldız, A. M. Soydan, M. Akei, E. F. Ipcizade, and A. Ata, “Characterization of  $\text{MO}_y\text{--M}_x\text{Ce}_{1-x}\text{O}_{2-\delta}$  (M: Co, Ni & Cu) nano powders and anode materials for low and intermediate temperature solid oxide fuel cells”, *International Journal of Hydrogen Energy*, 40[40] (2015) 14085-14094.
- [28] S. Sameshima, M. Kawaminami, and Y. Hirata, “Thermal Expansion of Rare-Earth-Doped Ceria Ceramics”, *Journal of the Ceramic Society of Japan*, 110[7] (2002). 597-600.
- [29] G. Kaur, and S. Basu, “Performance studies of copper–iron/ceria–yttria stabilized zirconia anode for electro-oxidation of butane in solid oxide fuel cells” , *Journal of Power Sources*, 241(2013) 783-790.
- [30] M. Cimenti, and J.M. Hill, “Direct utilization of methanol and ethanol in solid oxide fuel cells using  $\text{Cu--Co(Ru)/Zr}_{0.35}\text{Ce}_{0.65}\text{O}_{2-\delta}$  anodes”, *Journal of Power Sources*, 195[13] (2010) 3996-4001.
- [31] S.-I. Lee, K. Ahn, J. M. Vohs, and R. J. Gorte, “Cu-Co Bimetallic Anodes for Direct Utilization of Methane in SOFCs”, *Electrochemical and Solid-State Letters*, 8[1] (2005) A48.
- [32] X.-F. Ye, S. R. Wang, Q. Hu, J. Y. Chen, T. L. Wen, and Z. Y. Wen, “Improvement of  $\text{Cu--CeO}_2$  anodes for SOFCs running on ethanol fuels”, *Solid State Ionics*, 180[2-3] (2009) 276-281.



- 
- [33] A. Fuerte, R. X. Valenzuela, M. J. Escudero and L. Daza, “Effect of cobalt incorporation in copper-ceria based anodes for hydrocarbon utilisation in Intermediate Temperature Solid Oxide Fuel Cells”, *Journal of Power Sources*, 196[9] (2011) 4324-4331.
- [34] B.R. Munson, “Fundamental of fluid mechanics”, Wiley, New York (1990).
- [35] P. Forchheimer, “Wasserbewegung durch boden”, *Zeit. Ver. Deutsch. Ing.*, 45 (1901) 1781-1788.
- [36] G.H. Fancher, and J.A. Lewis, “Flow of simple fluids through porous materials”, *Ind. Engng. Chem.*, 25[10] (1933) 1139-1147.
- [37] S.M. Hassanizadeh, and W.G. Gray, “High velocity flow in porous media”, *Transport in Porous Media*, 2 (1987) 521-531.
- [38] T.H. Chilton, and A.P. Colburn, “Pressure drop in packed tubes”, *Ind Engng. Chem.*, 23[8] (1931) 913-919.
- [39] S. Ergun, “Fluid flow through packed columns” *Chem. Engng. Prog.*, 48[2] (1952) 89-94.
- [40] F. Hartmeister, “Analysis of nonlinear Darcy-Forchheimer flows in porous”, Texas Tech University, (2009).
- [41] A.S.T.M., “Manual on the use of thermocouples in temperature measurement Fourth Edition”, (1993).



[42] 王柏崴，高熱膨脹氧化物玻璃用於熱熔擠出及電絕緣特性之應用研究，國立台灣大學碩士論文，(2016)

[43] 陳牧民，使用生質燃料的固態燃料電池組之開發及測試，國立台灣大學碩士論文，(2014)

[44] 王丹，摻雜型鈹鐵基鈣鈦礦材料用於中溫固態燃料電池陰極之研究，國立台灣大學碩士論文，(2016)

[45] C.R. Bingham, Honeywell Inc., “Thermocouple comprising intimately twisted wires”, U.S. Pat. 3317353A, Dec. 6, 1962.

[46] F.A. Wolff, and J.H. Dellinger, “The electrical conductivity of commercial copper” (1910) 1981-2008.


[47] W.D. Callister Jr, and D.G. Rethwisch, “Materials Science and Engineering 8th Edition SI Version”, (2010).

[48] 黃怡婷，3D 列印銅基模具之材料性質分析與擠出模擬，國立台灣大學碩士論文，(2018)

[49] S.C. Singhal, “Advances in solid oxide fuel cell technology”, Solid State Ionics, 135(2000) 305-313.

[50] W.Z. Zhu, and S.C. Deevi, “A review on the status of anode materials for solid oxide fuel cells”, Materials Science and Engineering, A362 (2003) 228-239.

[51] A.A.Bokov, and A.V. Nikonov, “Formation mechanism of monoclinic ZrO<sub>2</sub> at the

- 
- Contact of YSZ with CuO”, *Inorganic Materials*, 51[6] (2015) 553-558.
- [52] M. Steinberg, “Fossil fuel de-carbonization technology for mitigating global warming”, *International journal of Hydrogen Energy*, 24[8] (1999) 771-777.
- [53] J.H. Lee, H. Moon, H. W. Lee, J. Kim, J. D. Kim, and K. H. Yoon, “Quantitative analysis of microstructure and its related electrical property of SOFC anode, Ni-YSZ cermet”, *Solid State Ionics*, 148 (2002) 15-26.
- [54] R. Konar, J. Mukhopadhyay, A. D. Sharma, and R. N. Basu, “Synthesis of Cu-YSZ and Ni-Cu-YSZ cermets by a novel electro-less technique for use as solid oxide fuel cell anode: Application potentiality towards fuel flexibility in biogas atmosphere”, *International journal of hydrogen energy*, 41(2016) 1151-1160.
- [55] K.T. Jacob, and C.B. Alcock, “Thermodynamics of  $\text{CuAlO}_2$  and  $\text{CuAl}_2\text{O}_4$  and phase equilibria in the system  $\text{Cu}_2\text{O-CuO-Al}_2\text{O}_3$ ”, *Journal of the American Ceramic Society*. 58[5-6] (1975) 192-195.
- [56] S. Ran, L. Winnubst, W. Wiratha, and D. H. A. Blank, “Sintering behavior of 0.8 mol%-CuO-doped 3Y-TZP ceramics”, *The American Ceramic Society*, 89[1] (2006) 151-155.
- [57] 吳貞儀，直接丙烷固態氧化物燃料電池之燃料重組研究，國立清華大學碩士論文，(2010).